

THREE-DIMENSIONAL, UNSTRUCTURED-GRID NUMERICAL  
SIMULATIONS OF HYDRODYNAMICS AND SCALAR  
TRANSPORT IN SAN FRANCISCO BAY

A DISSERTATION  
SUBMITTED TO THE DEPARTMENT OF CIVIL AND  
ENVIRONMENTAL ENGINEERING  
AND THE COMMITTEE ON GRADUATE STUDIES  
OF STANFORD UNIVERSITY  
IN PARTIAL FULFILLMENT OF THE REQUIREMENTS  
FOR THE DEGREE OF  
DOCTOR OF PHILOSOPHY

Vivien P. Chua  
September, 2011

UMI Number: 3497149

All rights reserved

INFORMATION TO ALL USERS

The quality of this reproduction is dependent upon the quality of the copy submitted.

In the unlikely event that the author did not send a complete manuscript and there are missing pages, these will be noted. Also, if material had to be removed, a note will indicate the deletion.



UMI 3497149

Copyright 2012 by ProQuest LLC.


All rights reserved. This edition of the work is protected against unauthorized copying under Title 17, United States Code.



ProQuest LLC  
789 East Eisenhower Parkway  
P.O. Box 1346  
Ann Arbor, MI 48106-1346

© Copyright by Vivien P. Chua 2011  
All Rights Reserved

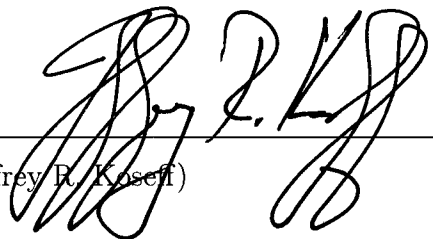
I certify that I have read this dissertation and that, in my opinion, it is fully adequate in scope and quality as a dissertation for the degree of Doctor of Philosophy.

  
\_\_\_\_\_  
(Oliver B. Fringer) Principal Adviser

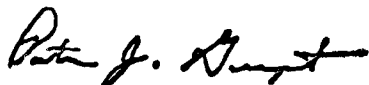
I certify that I have read this dissertation and that, in my opinion, it is fully adequate in scope and quality as a dissertation for the degree of Doctor of Philosophy.

  
\_\_\_\_\_  
(Stephen G. Monismith)

I certify that I have read this dissertation and that, in my opinion, it is fully adequate in scope and quality as a dissertation for the degree of Doctor of Philosophy.

  
\_\_\_\_\_  
(Jeffrey R. Koseff)

Approved for the University Committee on Graduate Studies

  
\_\_\_\_\_

# Abstract

The unstructured-grid SUNTANS model is applied to San Francisco Bay and employed to perform three-dimensional simulations of flow in order to assess the performance of high- and low- order scalar transport schemes. The potential impacts of climate change are also studied. Using a grid with an average resolution of 50 m, the model accurately resolves tidal hydrodynamics in a domain that extends from the Pacific Ocean to the western portion of the Delta region, the flow through which is approximated with two rectangular boxes as a “false delta”. A detailed calibration is performed, and we show that the model accurately predicts tidal heights, currents, and salinity at several locations throughout the Bay.

A sensitivity study is presented to understand the effects of grid resolution, the turbulence model, and the scalar transport scheme. Three levels of grid refinement are performed, and the results of a second-order accurate, TVD scalar transport scheme are compared to those with first-order upwinding. Our results show that the best convergence rate with respect to grid refinement occurs when the TVD scheme is employed. This accuracy degrades when the turbulence model is not employed due to a lack of feedback between vertical turbulent mixing and stratification. Significant horizontal diffusion associated with first-order upwinding eliminates the necessary horizontal salinity gradients required to induce baroclinic circulation and renders the results less sensitive to the turbulence model or grid refinement.

The quantification of numerical diffusion on unstructured grids when employing the finite-volume method is accomplished with a novel approach to analytically derive diffusion coefficients by extending the Hirt analysis on Cartesian grids to unstructured

grids. Two forms of computing the modified equation termed the independent analysis and the combined analysis are employed. Numerical diffusion coefficients are overpredicted with the independent analysis which separately derives the modified equation for the two types of cells, while the combined analysis which employs a recurrence relation for one equation obtains the correct diffusion coefficients. The numerical diffusion coefficients are analytically derived for first-order upwinding and the second-order scheme which stabilizes central differencing but introduces dispersion. First-order upwinding is stable with the most restrictive Courant number constraint  $0 \leq C_0 \leq \sqrt{3}/2 \approx 0.87$  when  $\theta = \pi/6$ , while the second-order scheme is stable with  $0 \leq C_0 \leq 2/\sqrt{6} \approx 0.82$  for all  $\theta$ . An accuracy analysis shows that first-order upwinding is first-order accurate in time and space and the second-order scheme is second-order accurate in time and space.

An alternative domain-averaged formulation provides an estimate for numerical diffusion without the need for analytical methods. This formulation is particularly suited to compare the performance of high- and low- order scalar advection schemes for applications in complex geometries, and is applied to San Francisco Bay to assess the impact of tidal straining and time scales on numerical diffusion. Over long time-scales, the TVD scheme is less effective in regions of high tidal dispersion, since grid-scale variability resulting from strong straining of the tracer field causes strong numerical diffusion regardless of the method employed. For short time scales, the net diffusion coefficient is consistently smaller for the TVD scheme compared to first-order upwinding.

The unstructured-grid SUNTANS model is subsequently employed to investigate the implications of sea-level rise on salinity intrusion and estuarine circulation under different hydrologic scenarios in North San Francisco Bay. Rising sea levels reduce the impact of bottom-generated turbulence causing less vertical mixing. This leads to stronger gravitational circulation and higher vertical stratification, resulting in enhanced salinity intrusion. Under low-flow conditions, salinity intrusion is the largest because sea-level rise has a greater impact due to weaker vertical stratification. Strong flows increase the strength of the gravitational circulation, resulting in higher vertical stratification, which leads to the nonlinear feedback between vertical mixing and

stratification. The effect of sea-level rise on vertical stratification and consequently salinity intrusion is reduced owing to the suppression of mixing by stratification.

# Acknowledgements

First and foremost, I would like to express my sincere gratitude to my advisor Professor Oliver Fringer, for his guidance, patience and encouragement. His consuming enthusiasm and passion for research is infectious, and has since deeply influenced my chosen career field as well as approach to scientific research. I will always be indebted to him for this opportunity to pursue my Ph.D, and for his invaluable support during this incredible journey.

I am grateful to my committee members, Professor Stephen Monismith and Professor Jeff Koseff for their advice and encouragement. I would also like to thank Dr Derek Fong for taking on the task of examining my defense, and Professor Leif Thomas for chairing the committee. I am deeply indebted to Dr Rocky Geyer of Woods Hole Oceanographic Institute for imparting his vast knowledge and experience, and for being a huge source of inspiration for the budding scientist in me. I would like to thank Dr Edward Gross of Bay Modeling Consultancy for the many valuable discussions on numerical methods and estuarine circulation.

I have been very fortunate to meet many mentors who are extremely supportive of my academic pursuits. I would particularly like to thank Professor Margot Gerritsen for her support and guidance during my time at the Institute of Computational and Mathematical Engineering (ICME). Through her encouragement, I gained a newfound confidence and drive to pursue my Ph.D. I am grateful to Professor Walter Murray for the Stanford experience, which has forever changed the path of my life. I would like to thank my undergraduate advisor Professor Mason Porter (currently at Oxford University) for showing me the ropes to scientific research. His mentorship and guidance has opened up exciting new opportunities for me, and provided me with



the courage and desire to pursue a Ph.D. I am also grateful to Professor Lee Chin Hui at Georgia Institute of Technology for the opportunity to broaden my research horizons.

Members of the SUNTANS group have contributed immensely to my professional development and are frequently my first resource for research-related questions. I am especially grateful to past and present group members, Bing Wang, Zhonghua Zhang, Yi-Ju Chou, Dajuan Kang, Subbayya Sankaranarayanan, Goncalo Gil, Sergey Kooltakov, Sean Vitousek and Phillip Wolfram. I would like to thank my officemates, May Chui, Maha Alnajjar, Cameron McDonald and Lianna Sameul, whose presence make this a place I look forward to coming everyday. I have appreciated the camaraderie of students in EFML, Rica Enrique, Jamie Fleischfresser, Sarah Giddings, Erin Hult, Sueann Lee, Xiaoyi Liu, Ryan Moniz, Mike Squibb, Vamsi Sridharan, Liv Walter, Ryan Walter and Joel Weitman. I would also like to acknowledge the wonderful work of the EFML administrators, Jill Nomura and Yusong Rogers, for overseeing the smooth running of our lab.

I gratefully acknowledge the funding sources that allowed me the freedom to pursue my Ph.D pursuits. My time at Stanford was supported by the Singapore National Research Foundation (Environment and Water Technologies) Ph.D Scholarship (Overseas) and the Stanford School of Engineering Graduate Fellowship. I would also like to acknowledge the support of the California State Coastal Conservancy (Agreement Number 07-137; Program managers Abe Doherty, Doug George, and Matt Gerhart). My dissertation work was conducted on the Peter A. McCuen Environmental Computing Center at Stanford University.

My Stanford days were a wonderful memory to reflect upon because of the many heartwarming friendships. I would like to thank Sanghui Ahn, Boram Lee, and Jennifer Shen for their support and friendship. I will forever cherish the memories of travels and parties, all of which has made my otherwise dull and boring Ph.D life, so much more colorful. I also have my friends at ICME, Thomas Callaghan, Johnny Carlsson, Henry Kim, Sarah Macumber, and Tanvi Vyas to thank for the easy transition in my first year at Stanford.

I am grateful to my friends in Singapore, Yanshan Chen and Kaijing Lim; my

Bay Area friends, Alvin Barlian, Bert Chi, Victoria Gong, Bryan Hong, Denise Lee, Miranda Lee, Andreas Sundquist, Ariel Tang, Jonathan Teo, Michael Tung, and Christina Yin for their friendship. My life at Stanford was also enriched by the Great Exchange Covenant Church (GRX), Bridgeway Church of Silicon Valley, and the Singapore Student Association.

This dissertation has been possible only with the love and unconditional support of my family. My parents whom this dissertation is dedicated to, have been a constant source of love, support and inspiration for me. I would like to express my deepest appreciation to Dad and Mom, who have always encouraged me to pursue my dreams, and regardless of all will be my number one cheerleader in life. My younger brother Edwin for his companionship growing up, and who can be counted on to provide humor and support at all times. I could not have asked for a better family.

Above all, I thank God for the wisdom, strength, endurance and patience to complete this dissertation.

Dedicated to  
Mom and Dad

# Nomenclature

## Roman Symbols

- $(s_f)_\alpha$  Scalar concentration on face  $\alpha$
- $(s_f)_\beta$  Scalar concentration on face  $\beta$
- $(s_f)_\gamma$  Scalar concentration on face  $\gamma$
- $(s_f)_j$  Scalar concentration on face  $j$
- $\bar{X}$  Quantity time-averaged over the calibration period
- $\text{cov}_{xy}$  Covariance in x and y directions
- $h_{\text{buffer}}$  Buffering layer thickness
- $h_{\text{dry}}$  Minimum depth for dry cell
- $\mathbf{u}_0$  Velocity vector
- $\mathbf{u}_1$  Velocity vector in first grid cell above bed
- $a$  Area of triangle grid cell
- $A_0$  Tidally-averaged cross-sectional area
- $A_b$  Cross-sectional area of boundary
- $A_i$  Scalar concentration for type A cell

|            |   |
|------------|---|
| $B_i$      | Scalar concentration for type B cell                    |
| $C_0$      | Courant number on Cartesian grids                       |
| $C_\alpha$ | Courant number on face $\alpha$                         |
| $C_\beta$  | Courant number on face $\beta$                          |
| $C_\gamma$ | Courant number on face $\gamma$                         |
| $C_d$      | Drag coefficient  |
| $C_e$      | Courant number on east face                             |
| $C_f$      | Courant number on face                                  |
| $C_l$      | Courant number on unstructured grids                    |
| $C_x$      | Courant number on face x                                |
| $C_y$      | Courant number on face y                                |
| $D$        | Diagonal matrix composed of eigenvalues of $K_D$        |
| $d$        | Water depth measured from the undisturbed water surface |
| $d_1, d_2$ | Principal diagonal components of $D$                    |
| $E$        | Error norm  |
| $F$        | Subtidal salt flux                                      |
| $f$        | Coriolis parameter                                      |
| $F_E$      | Steady exchange flux                                    |
| $F_R$      | River flux  |
| $F_T$      | Tidal flux  |
| $g$        | Acceleration due to gravity                             |

|                              |  |
|------------------------------|--|
| $H$                          | Depth  |
| $h$                          | Free-surface height  |
| $I$                          | Non-dimensional constant   |
| $K$                          | Longitudinal dispersion coefficient  |
| $K'$                         | Longitudinal dispersion coefficient in the main channel                            |
| $k - \epsilon$               | k-epsilon two-equation turbulence closure model                                    |
| $k - \omega$                 | k-omega two-equation turbulence closure model                                      |
| $k - kl$                     | k-kl two-equation turbulence closure model (MY25)                                  |
| $k^{-1}$                     | Characteristic residence time  |
| $k_{xxx}$                    | Numerical dispersion coefficient in streamwise direction                           |
| $k_{xxx}^A$                  | Numerical dispersion coefficient in streamwise direction for type A cell           |
| $k_{xxx}^B$                  | Numerical dispersion coefficient in streamwise direction for type B cell           |
| $k_{xxx}^{1d}$               | Numerical dispersion coefficient on one-dimensional Cartesian grids                |
| $k_{xxx}^{2d}$               | Numerical dispersion coefficient in x direction on two-dimensional Cartesian grids |
| $k_{xxy}, k_{xyy}$           | Numerical dispersion coefficient in cross-directions                               |
| $k_{xxy}^A, k_{xyy}^A$       | Numerical dispersion coefficient in cross-directions for type A cell               |
| $k_{xxy}^B, k_{xyy}^B$       | Numerical dispersion coefficient in cross-directions for type B cell               |
| $k_{xxy}^{2d}, k_{xyy}^{2d}$ | Numerical dispersion coefficient on two-dimensional Cartesian grids                |
| $k_{xx}$                     | Numerical diffusion coefficient in streamwise direction                            |
| $k_{xx}^A$                   | Numerical diffusion coefficient in streamwise direction for type A cell            |

|                   |  |
|-------------------|--|
| $k_{xx}^B$        | Numerical diffusion coefficient in streamwise direction for type B cell            |
| $k_{xx}^{1d}$     | Numerical diffusion coefficient on one-dimensional Cartesian grids                 |
| $k_{xx}^{2d}$     | Numerical diffusion coefficient in x direction on two-dimensional Cartesian grids  |
| $k_{xy}$          | Numerical diffusion coefficient in cross-direction                                 |
| $k_{xy}^A$        | Numerical diffusion coefficient of cross-direction for type A cell                 |
| $k_{xy}^B$        | Numerical diffusion coefficient in cross-direction for type B cell                 |
| $k_{xy}^{2d}$     | Numerical diffusion coefficient in xy direction on two-dimensional Cartesian grids |
| $k_{yyy}$         | Numerical dispersion coefficient in lateral direction                              |
| $k_{yyy}^A$       | Numerical dispersion coefficient in lateral direction for type A cell              |
| $k_{yyy}^B$       | Numerical dispersion coefficient in lateral direction for type B cell              |
| $k_{yyy}^{2d}$    | Numerical dispersion coefficient in y direction on two-dimensional Cartesian grids |
| $k_{yy}$          | Numerical diffusion coefficient in lateral direction                               |
| $k_{yy}^A$        | Numerical diffusion coefficient in lateral direction for type A cell               |
| $k_{yy}^B$        | Numerical diffusion coefficient in lateral direction for type B cell               |
| $k_{yy}^{2d}$     | Numerical diffusion coefficient in y direction on two-dimensional Cartesian grids  |
| $K_D$             | Diffusion tensor   |
| $L$               | Length   |
| $L_{\text{tide}}$ | Tidal excursion length   |

|             |  |
|-------------|--|
| $M$         | Matrix composed of eigenvectors of $K_D$       |
| $m_0$       | Zeroth moment                                  |
| $m_{1x}$    | First moment in x direction                    |
| $m_{1y}$    | First moment in y direction                    |
| $m_{2x}$    | Second moment in x direction                   |
| $m_{2y}$    | Second moment in y direction                   |
| $m_{xy}$    | x-y correlation                                |
| $N$         | Number of elements                             |
| $P$         | Pressure                                       |
| $Q$         | Freshwater flow rate                           |
| $R$         | Radius of Gaussian tracer field                |
| $r$         | Baroclinic head                                |
| $R_\theta$  | Rotation matrix                                |
| $r_v$       | Trap to channel volume ratio                   |
| $r_{i+1/2}$ | Ratio of the upwind to the local gradient      |
| $Ri_x$      | Horizontal Richardson number                   |
| $S$         | Time- and depth-averaged salinity              |
| $s$         | Salinity                                       |
| $s'$        | Cross-sectionally and tidally varying salinity |
| $s^{n+1}$   | Scalar concentration at time step $n + 1$      |
| $s^n$       | Scalar concentration at time step $n$          |



|           |   |
|-----------|---|
| $s_0^R$   | Reference salinity                                      |
| $s_a$     | Cross-sectionally and tidally averaged salinity         |
| $s_c$     | Cross-sectionally averaged and tidally varying salinity |
| $s_e$     | Scalar concentration on east face                       |
| $s_f$     | Face-averaged scalar concentration                      |
| $s_i$     | Cell-centered scalar concentration                      |
| $s_j$     | Scalar concentration adjacent to face $j$               |
| $s_o$     | Observed salinity                                       |
| $s_p$     | Predicted salinity                                      |
| $s_s$     | Tidally-averaged and cross-sectionally varying salinity |
| $s'_V$    | Vertically varying salinity perturbation                |
| $s_w$     | Scalar concentration on west face                       |
| $s_{i+1}$ | Upwind cell scalar concentration                        |
| $s_{i-1}$ | Downwind cell scalar concentration                      |
| $T$       | Tidal period  |
| $t$       | Time  |
| $T'$      | Time scale for cross-sectional mixing                   |
| $T_c$     | Time scale for transverse mixing                        |
| $U, V$    | Depth-averaged Cartesian horizontal velocity components |
| $u, v$    | Cartesian horizontal velocity components                |
| $u'$      | Cross-sectionally and tidally varying velocity          |

|                   |   |
|-------------------|---|
| $u^A$             | Advective velocity in streamwise direction for type A cell  |
| $u^B$             | Advective velocity in streamwise direction for type B cell  |
| $u_0$             | Constant velocity   |
| $U_1$             | Magnitude of $\mathbf{u}_1$   |
| $U_\alpha$        | Velocity normal to face $\alpha$  |
| $u_*$             | Friction velocity   |
| $U_\beta$         | Velocity normal to face $\beta$   |
| $U_\gamma$        | Velocity normal to face $\gamma$  |
| $u_{\text{dev}}$  | Deviation of mean flow velocity from the cross-sectional variation of the depth-averaged velocity |
| $U_{\text{GC}}$   | Velocity scale for exchange flow  |
| $U_{\text{tide}}$ | Maximum velocity of tidal flow  |
| $u_a$             | Cross-sectionally and tidally averaged velocity   |
| $u_b$             | Cross-sectionally averaged velocity at boundary   |
| $u_c$             | Cross-sectionally averaged and tidally varying velocity   |
| $u_i$             | Velocity of grid cell edge $i$  |
| $u_s$             | Tidally-averaged and cross-sectionally varying velocity   |
| $v^A$             | Advective velocity in lateral direction for type A cell   |
| $v^B$             | Advective velocity in lateral direction for type B cell   |
| $W$               | Width   |
| $w$               | Vertical velocity   |

|                    |  |
|--------------------|--|
| $x, y$             | Cartesian horizontal coordinates   |
| $x_0, y_0$         | Coordinates of center of Gaussian tracer field   |
| $X_2$              | Distance (in km) from the Golden Gate Bridge measured along the longitudinal axis to the location where the bottom salinity is 2 psu |
| $X_{\text{model}}$ | Model-predicted quantity   |
| $X_{\text{obs}}$   | Observed quantity  |
| $X_s$              | Salinity intrusion length scale  |
| $z$                | Vertical coordinate  |
| $z_0$              | Roughness coefficient  |
| $z_1$              | Location of $U_1$ at a distance of one-half bottom-most vertical grid spacing above bed  |

### Greek Symbols

|                    |  |
|--------------------|--|
| $\beta$            | Coefficient of salt expansivity  |
| $\Delta l$         | Side length of triangle grid cell  |
| $\Delta r$         | Voronoi distance between grid cells                                      |
| $\Delta t$         | Time step  |
| $\Delta x$         | Space discretization   |
| $\delta_{xi}^{AA}$ | x-component of vector pointing from centroid of cell $A_i$ to cell $A_3$ |
| $\delta_{xi}^{AB}$ | x-component of vector pointing from centroid of cell $A_i$ to cell $B_1$ |
| $\delta_{xi}^{BA}$ | x-component of vector pointing from centroid of cell $B_i$ to cell $A_3$ |
| $\delta_{yi}^{AA}$ | y-component of vector pointing from centroid of cell $A_i$ to cell $A_3$ |

|                    |  |
|--------------------|--|
| $\delta_{yi}^{AB}$ | y-component of vector pointing from centroid of cell $A_i$ to cell $B_1$ |
| $\delta_{yi}^{BA}$ | y-component of vector pointing from centroid of cell $B_i$ to cell $A_3$ |
| $\epsilon$         | Eddy diffusivity   |
| $\epsilon_H$       | Horizontal eddy diffusivity  |
| $\epsilon_V$       | Vertical eddy diffusivity  |
| $\Gamma$           | Horizontal salinity gradient   |
| $\kappa$           | Von Karman's constant  |
| $\lambda_L$        | Ratio of the tidal excursion length to the eddy size                     |
| $\nu$              | ratio of tidal to total dispersive flux                                  |
| $\nu_E$            | Ratio of energy of the eddies to the tidal flow                          |
| $\nu_H$            | Horizontal eddy viscosity  |
| $\nu_V$            | Vertical eddy viscosity  |
| $\Omega$           | Angular velocity of the Earth  |
| $\omega$           | Frequency  |
| $\phi$             | Latitude   |
| $\rho$             | Density  |
| $\rho_0$           | Reference density  |
| $\sigma_x$         | Variance in x direction  |
| $\sigma_y$         | Variance in y direction  |
| $\tau_b$           | Bottom stress  |

$\theta$  Angle between edge  $\alpha$  and the flow direction

### Other Symbols

$\langle \cdot \rangle$  Tidally averaged

$\nabla$  Laplacian

$\nabla_H$  Horizontal Laplacian

$\bar{\cdot}$  Cross-sectionally averaged

$\sum$  Summation

### Abbreviations

CFL Courant-Friedrichs-Lewy

ELM Eulerian-Lagrangian Method

LLW Lower-low water

MLLW Mean lower-low water

MSL Mean sea level

MY25 Mellor-Yamada level 2.5 scheme

RMS Root-mean-square

SIPS Strain-induced periodic stratification

TV Total variation

TVD Total-variation diminishing

USGS United States Geological Survey

$\theta_\alpha$  Angle from the horizontal at which the principal axis is aligned

# Contents

|   |            |
|---|------------|
| <b>Abstract</b>   | <b>iv</b>  |
| <b>Acknowledgements</b>                                     | <b>vii</b> |
| <b>Nomenclature</b>   | <b>xi</b>  |
| <b>Table of Contents</b>                                    | <b>xx</b>  |
| <b>List of Tables</b>                                       | <b>xx</b>  |
| <b>List of Figures</b>                                      | <b>xx</b>  |
| <b>1 Introduction</b>                                       | <b>1</b>   |
| 1.1 Motivation . . . . .                                    | 1          |
| 1.2 San Francisco Bay . . . . .                             | 2          |
| 1.3 Potential climate change impacts . . . . .              | 6          |
| 1.3.1 Potential land loss and coastal flood risk . . . . .  | 6          |
| 1.3.2 Impact on freshwater resources and habitats . . . . . | 7          |
| 1.4 Hydrodynamic modeling . . . . .                         | 8          |
| 1.4.1 Depth-averaged models . . . . .                       | 9          |
| 1.4.2 Three-dimensional models . . . . .                    | 9          |
| 1.4.3 San Francisco Bay . . . . .                           | 11         |
| 1.5 Mixing mechanisms in estuaries . . . . .                | 12         |
| 1.5.1 Salt flux decomposition . . . . .                     | 13         |
| 1.5.2 Shear flow dispersion . . . . .                       | 14         |

|          |  |           |
|----------|--|-----------|
| 1.5.3    | Tidal pumping/trapping . . . . .                     | 14        |
| 1.5.4    | Gravitational circulation . . . . .                  | 15        |
| 1.5.5    | Tidal random walk . . . . .                          | 17        |
| 1.5.6    | Horizontal turbulent mixing . . . . .                | 18        |
| 1.6      | Modeling scalar transport . . . . .                  | 18        |
| 1.6.1    | Scalar advection schemes . . . . .                   | 20        |
| 1.7      | Dissertation roadmap . . . . .                       | 24        |
| <b>2</b> | <b>San Francisco Bay numerical model</b>             | <b>26</b> |
| 2.1      | Introduction . . . . .                               | 26        |
| 2.2      | Governing equations and numerical method . . . . .   | 26        |
| 2.2.1    | Bottom shear stress and turbulence closure . . . . . | 28        |
| 2.2.2    | Wet-dry treatment . . . . .                          | 29        |
| 2.2.3    | Numerical method for scalar transport . . . . .      | 29        |
| 2.3      | Setup of San Francisco Bay simulation . . . . .      | 31        |
| 2.3.1    | Computational domain . . . . .                       | 31        |
| 2.3.2    | Bathymetry . . . . .                                 | 31        |
| 2.3.3    | Unstructured grid . . . . .                          | 33        |
| 2.3.4    | Initial and boundary conditions . . . . .            | 33        |
| 2.4      | Model calibration and validation . . . . .           | 37        |
| 2.4.1    | Surface elevations . . . . .                         | 37        |
| 2.4.2    | Currents . . . . .                                   | 45        |
| 2.4.3    | Salinity . . . . .                                   | 49        |
| 2.5      | Summary . . . . .                                    | 53        |
| <b>3</b> | <b>Sensitivity analysis of salinity simulations</b>  | <b>55</b> |
| 3.1      | Introduction . . . . .                               | 55        |
| 3.2      | Sensitivity to grid resolution . . . . .             | 55        |
| 3.3      | Salt flux analysis . . . . .                         | 64        |
| 3.4      | Summary . . . . .                                    | 66        |

|          |   |            |
|----------|---|------------|
| <b>4</b> | <b>Numerical scalar diffusion on unstructured grids</b>                                 | <b>68</b>  |
| 4.1      | Introduction . . . . .  | 68         |
| 4.2      | Quantification of numerical diffusion . . . . .   | 68         |
| 4.2.1    | Numerical diffusion on Cartesian grids . . . . .  | 68         |
| 4.2.2    | Numerical diffusion on unstructured grids . . . . .                                     | 74         |
| 4.3      | Numerical simulations . . . . .   | 96         |
| 4.3.1    | Accuracy analysis . . . . .   | 101        |
| 4.4      | Summary and discussion . . . . .  | 102        |
| <b>5</b> | <b>Numerical diffusion in San Francisco Bay</b>   | <b>107</b> |
| 5.1      | Introduction . . . . .  | 107        |
| 5.1.1    | Inferring the diffusion coefficient for general discretizations . . . . .               | 107        |
| 5.2      | Numerical simulations . . . . .   | 110        |
| 5.2.1    | Idealized simulations . . . . .   | 110        |
| 5.2.2    | Numerical diffusion in San Francisco Bay . . . . .                                      | 115        |
| 5.3      | Tidal dispersion . . . . .  | 116        |
| 5.4      | Diffusion coefficients evaluated over different time scales . . . . .                   | 117        |
| 5.5      | Summary . . . . .   | 125        |
| <b>6</b> | <b>Potential climate change impacts on estuarine circulation and salinity intrusion</b> | <b>128</b> |
| 6.1      | Introduction . . . . .  | 128        |
| 6.2      | Numerical Model . . . . .   | 128        |
| 6.3      | Climate Change Scenarios . . . . .  | 129        |
| 6.4      | Salinity intrusion and estuarine circulation . . . . .                                  | 131        |
| 6.5      | Quantifying salinity intrusion due to sea-level rise . . . . .                          | 134        |
| 6.6      | Estimating the effect of sea-level rise on $X_2$ . . . . .                              | 138        |
| 6.7      | Summary . . . . .   | 139        |
| <b>7</b> | <b>Conclusion</b>   | <b>141</b> |
| 7.1      | San Francisco Bay numerical model . . . . .   | 141        |
| 7.2      | Sensitivity analysis of salinity simulations . . . . .                                  | 142        |



|                     |   |            |
|---------------------|---|------------|
| 7.3                 | Numerical scalar diffusion on unstructured grids . . . . .                                    | 143        |
| 7.4                 | Numerical diffusion in San Francisco Bay . . . . .  | 145        |
| 7.5                 | Potential climate change impacts on estuarine circulation and salinity<br>intrusion . . . . . | 145        |
| 7.6                 | Recommendations . . . . .   | 146        |
| <b>Appendix A</b>   |   | <b>150</b> |
| <b>Bibliography</b> |   | <b>150</b> |

# List of Tables

|     |  |     |
|-----|--|-----|
| 2.1 | Statistical evaluation of surface elevations . . . . .   | 39  |
| 2.2 | M2 surface elevation constituents . . . . .  | 41  |
| 2.3 | K1 surface elevation constituents . . . . .  | 43  |
| 2.4 | S1 surface elevation constituents . . . . .  | 43  |
| 2.5 | O1 surface elevation constituents . . . . .  | 44  |
| 2.6 | N2 surface elevation constituents . . . . .  | 44  |
| 2.7 | Statistical evaluation of depth-averaged velocities . . . . .  | 49  |
| 2.8 | Statistical evaluation of salinity. . . . .  | 53  |
| 3.1 | Least squares fitted convergence rates for runs A – D . . . . .  | 58  |
| 5.1 | Channel flow numerical simulations with the addition of physical diffusion. $k_{xx}$ derived in Chapter 4 for the case that $\theta = 0$ is shown for comparison. $k_{yy} = k_{xy} = 0$ when $\theta = 0$ . Diffusion coefficients are in $\text{m}^2 \text{s}^{-1}$ . $k_{\text{num}} = k_{\text{net}} - k_{\text{phys}}$ . . . . . | 114 |
| 5.2 | Comparisons of $k_{\text{net}}$ and $k_{\text{num,local}}$ from channel flow numerical simulations. Diffusion coefficients are in $\text{m}^2 \text{s}^{-1}$ . . . . .   | 115 |
| 5.3 | Mean $k_{\text{net}}$ (in $\text{m}^2 \text{s}^{-1}$ ) in San Francisco Bay for the re-initialized simulations and those run over a three-day period. . . . .  | 127 |
| 6.1 | Least-squares fit of the form $X_2 = bQ^n$ for sea-level rise scenarios in Fig. 6.3. . . . .   | 137 |
| 6.2 | Least-squares fit of the form $X_2 = c(H_0 + \Delta H)^m$ for the inflow scenarios in Fig. 6.4. . . . .  | 138 |

# List of Figures

|     |   |    |
|-----|---|----|
| 1.1 | The San Francisco Bay model domain and bathymetry (in m below MSL). . . . .   | 3  |
| 1.2 | Cell $i$ with east and west faces indicated by $e$ and $w$ , respectively. . .  | 20 |
| 2.1 | The San Francisco Bay model domain . . . . .  | 32 |
| 2.2 | The unstructured grid of San Francisco Bay. Entire domain (a), refinement at Golden Gate (b), and rectangular “false deltas” (c). . . .   | 34 |
| 2.3 | Metric of orthogonality for San Francisco Bay. Greyscale depicts the distribution of angle skewness, in degrees. . . . .  | 35 |
| 2.4 | Intertidal mudflats in North San Francisco Bay are exposed during LLW (shown in black). Surface elevations (in m) on the wet areas are plotted for day 30.9. . . . .  | 38 |
| 2.5 | Comparison of predicted and observed surface elevations (in m) at (a) Fort Point (b) Richmond (c) Alameda and (d) San Mateo Bridge. Legend: predictions ( $\cdots$ ), observations ( $—$ ) . . . . .  | 40 |
| 2.6 | Distribution of amplitudes (in m) and phases (in degrees) for M2 and K1 harmonics plotted against distance from Golden Gate. Points in South Bay are negative and those in North Bay are positive. Legend: predictions ( $-o-$ ), observations ( $-x-$ ). . . . . | 42 |
| 2.7 | Comparison of predicted and observed depth-averaged velocities ( $m s^{-1}$ ) at Richmond. Legend: predictions ( $\cdots$ ), observations ( $—$ ). . . . .  | 45 |
| 2.8 | Comparison of predicted and observed U and V velocity profiles (in $m s^{-1}$ ) at Richmond. . . . .  | 46 |

|      |   |    |
|------|---|----|
| 2.9  | Comparison of predicted and observed depth-averaged velocities ( $\text{m s}^{-1}$ ) at Oakland. Legend: predictions ( $\cdots$ ), observations ( $\text{---}$ ). . . . .   | 47 |
| 2.10 | Comparison of predicted and observed U and V velocity profiles (in $\text{m s}^{-1}$ ) at Oakland. . . . .  | 48 |
| 2.11 | Comparison of predicted and observed salinities (in psu) at Point San Pablo (a) surface elevations (b) surface salinity (c) bottom salinity (d) stratification. Surface and bottom salinities are 7.9 m and 0.9 m from the bottom, respectively. Legend: predictions ( $\cdots$ ), observations ( $\text{---}$ ). . . . .   | 51 |
| 2.12 | Comparison of predicted and observed salinities (in psu) at Benicia (a) surface elevations (b) surface salinity (c) bottom salinity (d) stratification. Surface and bottom salinities are 22.5 m and 7.6 m from the bottom, respectively. Legend: predictions ( $\cdots$ ), observations ( $\text{---}$ ). . . . .  | 52 |
| 3.1  | Convergence of the mean (a) and RMS (b) bottom salinity errors (in psu) as a function of grid refinement $\Delta x$ (km) at Benicia and Point San Pablo. Legend: Run A ( $\circ$ ), Run B ( $\triangle$ ), Run C ( $\square$ ), Run D ( $\diamond$ ), result of Gross et al. (2009) ( $*$ ), result of MacWilliams et al. (2007) ( $+$ ). . . . .   | 60 |
| 3.2  | Vertical profiles of salinity (in psu) along the transect depicted in Fig. 2.1 in Carquinez Strait tidally-averaged on year day 44 on the finest mesh. Runs: (A) TVD with turbulence model (B) TVD without turbulence model (C) First-order upwind with turbulence model (D) First-order upwind without turbulence model. . . . .   | 61 |
| 3.3  | Depth-averaged salinities (in psu) from the Golden Gate along the longitudinal axis in North San Francisco Bay. Legend: (A) TVD with turbulence model ( $\text{---}$ ), (B) TVD without turbulence model ( $\text{--.}$ ), (C) First-order upwind with turbulence model ( $\text{---}$ ), (D) First-order upwind without turbulence model ( $\cdots$ ). Results are computed for the finest mesh. . . . . | 62 |
| 3.4  | Time series of vertical profiles of the vertical eddy-diffusivity (in $\log(\text{m}^2\text{s}^{-1})$ ) at Benicia on the finest mesh. . . . .  | 63 |

|     |   |    |
|-----|---|----|
| 3.5 | Influence of the scalar advection scheme and turbulence model on tidally-averaged salt fluxes (in $\text{psu m}^3/\text{s}$ ) on fine (a) and coarse (b) meshes. Runs: (A) TVD with turbulence model, (B) TVD without turbulence model, (C) First-order upwind with turbulence model, (D) First-order upwind without turbulence model. Legend: Black: $F_R$ , Gray: $F_E$ , White: $F_T$ . Diffusive fraction $\nu = F_T/(F_T + F_E)$ and $1 - \nu = F_E/(F_T + F_E)$ . . . . . | 67 |
| 4.1 | Stability region for first-order upwinding based on the sign of the principle components of the diffusion tensor $d_1^{2d}$ and $d_2^{2d}$ . When $d_1^{2d} \geq 0$ and $d_2^{2d} \geq 0$ the scheme is stable. The black line shows the contour of $d_2^{2d} = 0$ while $d_1^{2d} \geq 0$ for $0 \leq C_0 \leq 1$ and $0 \leq \theta \leq \pi/2$ . . . . .   | 71 |
| 4.2 | Depiction of two-dimensional equilateral triangles. $(s_f)_j$ is the scalar concentration on face $j$ , $\Delta l_j$ is the length of face $j$ , $s_i$ is the scalar concentration of cell $i$ . Three types of edges are denoted by $\alpha$ , $\beta$ and $\gamma$ . The velocity field is aligned with the x-axis and we assume $\theta$ is defined as the angle that edge $\alpha$ makes with the flow direction. . . . .   | 76 |
| 4.3 | Two types of cells on unstructured grids. For type A cells, the velocity components are given by $U_\alpha =  U_\alpha $ , $U_\beta = - U_\beta $ and $U_\gamma =  U_\gamma $ . For type B cells, the velocity components are given by $U_\alpha = - U_\alpha $ , $U_\beta =  U_\beta $ and $U_\gamma = - U_\gamma $ . . . . .  | 77 |
| 4.4 | Unstructured grid composed of equilateral triangles, showing how type A cells are surrounded by type B cells and vice-versa. . . . .  | 77 |
| 4.5 | Stability region for first-order upwinding based on the sign of the principle components of the diffusion tensor $d_1$ and $d_2$ obtained from the combined analysis. When $d_1 \geq 0$ and $d_2 \geq 0$ the scheme is stable. The black line shows the contour of $d_2 = 0$ while $d_1 \geq 0$ for $0 \leq C_l \leq 1$ and $0 \leq \theta \leq \pi/3$ . . . . .  | 85 |

|      |   |     |
|------|---|-----|
| 4.6  | Result of advecting a Gaussian passive tracer field using first-order upwind (top row) and the second-order scheme (bottom row) on the grid with $\Delta x = 2000$ m. The results are shown after 50,000 s for $\theta = 0$ and $\theta = \pi/6$ . The grid cell size is represented by a small triangle on the top left hand corner of the plots. Legend: Numerical solution (black), Exact solution (red). . . . .  | 99  |
| 4.7  | Comparison of theoretical diffusion coefficients to those computed using first-order upwind and the second-order scheme on the grid with $\Delta l = 500$ m. Legend: Analytical $k_{xx}$ (—), $k_{yy}$ (---), $k_{xy}$ (⋯), Idealized simulations using spatial moments analysis (*), Independent analysis (red), and Combined analysis (black). . . . .  | 100 |
| 4.8  | Comparison of diffusion and dispersion coefficients from numerical simulations and the spectral method for $\theta = 0$ and $\pi/6$ . The results are shown after 50,000 s. The triangle in the upper left-hand corner of the plots indicates the triangle size used in the calculations. Legend: Numerical simulations (black), Spectral method (red). . . . .   | 101 |
| 4.9  | Accuracy in space and time for $\theta = 0$ and $\theta = \pi/6$ . Legend: $\theta = 0$ (red), $\theta = \pi/6$ (black), first-order upwind (—,○), second-order scheme (—,*) . . . . .  | 103 |
| 4.10 | Nondimensional $d_1$ and $d_2$ from the diffusion tensor as a function of $\theta$ with $C_0 = 0.1$ for first-order upwind and the second-order scheme from the combined analysis. First-order upwind is nondimensionalized with $(u_0\Delta l)$ and the second-order scheme is nondimensionalized with $(u_0^2\Delta t)$ . First row is first-order upwind and second row is the second-order scheme, with $\psi = 1, 1.5$ and $2$ . Legend: $d_1$ (—) and $d_2$ (---), black (unstructured grids), red (two-dimensional Cartesian grids). . . | 104 |
| 4.11 | Nondimensional dispersion coefficients as a function of $\theta$ with $C_0 = 0.1$ for the second-order scheme from the combined analysis. Legend: $k_{xxx}/(u_0\Delta l^2)$ (—), $k_{yyy}/(u_0\Delta l^2)$ (---), $k_{xxy}/(u_0\Delta l^2)$ (---), $k_{xyy}/(u_0\Delta l^2)$ (⋯), black (unstructured grids), red (two-dimensional Cartesian grids). . .  | 105 |

|     |  |     |
|-----|--|-----|
| 5.1 | Result of advecting a Gaussian passive tracer after 50,000 s with the TVD scheme (left column) and first-order upwind (right column). The three rows represent results with $k_{\text{phys}} = 0 \text{ m}^2 \text{ s}^{-1}$ (run C), $k_{\text{phys}} = 50 \text{ m}^2 \text{ s}^{-1}$ (run D) and $k_{\text{phys}} = 200 \text{ m}^2 \text{ s}^{-1}$ (run E). The grid cell size is represented by a small triangle on the top left hand corner of the plot. Legend: Numerical solution (black), Exact solution (red). . . . . | 112 |
| 5.2 | Comparison of $k_{\text{net}}$ with different amounts of physical diffusion. Legend: first-order upwind ( $--$ ), TVD ( $---$ ), $k_{\text{phys}} = 0 \text{ m}^2 \text{ s}^{-1}$ (black), $k_{\text{phys}} = 50 \text{ m}^2 \text{ s}^{-1}$ (red), $k_{\text{phys}} = 200 \text{ m}^2 \text{ s}^{-1}$ (blue). . . . .   | 113 |
| 5.3 | Sensitivity of $k_{\text{net}}$ to grid resolution. Legend: $k_{\text{net}}$ (black), $k_{\text{xx}}$ (red), First-order upwind ( $x, --$ ), Second-order ( $o, ---$ ). . . . .  | 114 |
| 5.4 | Evolution of passive tracer field at Golden Gate from 0 to 12 hour in 3 hour intervals. Left column is the TVD scheme and right column is first-order upwind. Note that the color axes change with time. . . . .   | 118 |
| 5.5 | Evolution of passive tracer field at Golden Gate from 15 to 21 hour in 3 hour intervals. Left column is the TVD scheme and right column is first-order upwind. Note that the color axes change with time. . . . .  | 119 |
| 5.6 | Evolution of passive tracer field at Carquinez Strait from 0 to 12 hour in 3 hour intervals. Left column is the TVD scheme, and right column is first-order upwind. Note that the color axes change with time. . . . .   | 120 |
| 5.7 | Evolution of passive tracer field at Carquinez Strait from 15 to 21 hour in 3 hour intervals. Left column is the TVD scheme, and right column is first-order upwind. Note that the color axes change with time. . . . .  | 121 |
| 5.8 | Evolution of passive tracer field in South Bay from 0 to 12 hour in 3 hour intervals. Left column is the TVD scheme, and right column is first-order upwind. Note that the color axes change with time. . . . .  | 122 |
| 5.9 | Evolution of passive tracer field in South Bay from 15 to 21 hour in 3 hour intervals. Left column is the TVD scheme, and right column is first-order upwind. Note that the color axes change with time. . . . .   | 123 |

|      |   |     |
|------|---|-----|
| 5.10 | Comparison of $k_{\text{net}}$ for the period of simulation at (a) Golden Gate (b) Carquinez Straits (c) South Bay Shoals. Legend: first-order upwind (---), TVD (—). . . . .   | 124 |
| 5.11 | Comparison of $k_{\text{net}}$ with reinitialization at (a) Golden Gate (b) Carquinez Straits (c) South Bay Shoals. Legend: first-order upwind (---), TVD (—). . . . .  | 126 |
| 6.1  | Tidal and depth-averaged salinities from the Golden Gate along the longitudinal axis in North San Francisco Bay. Distances into the Bay are positive and those towards the ocean are negative. Legend: Freshwater inflows $2000 \text{ m}^3\text{s}^{-1}$ (black), $800 \text{ m}^3\text{s}^{-1}$ (red), $300 \text{ m}^3\text{s}^{-1}$ (blue), and sea-level rise 0 m (—) 0.46 m (---), 1.00 m (·-·) and 1.39 m (···). . . . . | 131 |
| 6.2  | Vertical profiles of tidally-averaged salinity along a transect in Carquinez Strait (black line in Fig. 2.1) for $2000 \text{ m}^3\text{s}^{-1}$ , $800 \text{ m}^3\text{s}^{-1}$ and $300 \text{ m}^3\text{s}^{-1}$ freshwater inflows, and (a) 0 m (b) 0.46 m (c) 1.00 m (d) 1.39 m sea-level rise. . . . .   | 133 |
| 6.3  | Dependence of salinity intrusion length scale $X_2$ on inflows. Legend: Sea-level rise scenarios 0.00 m (—, ×), 0.46 m (---, ○), 1.00 m (···, *), 1.39 m (·-·, ◇). . . . .  | 136 |
| 6.4  | Dependence of salinity intrusion length scale $X_2$ on sea-level rise. Legend: Freshwater inflows $2000 \text{ m}^3\text{s}^{-1}$ (—, ×), $800 \text{ m}^3\text{s}^{-1}$ (---, ○), and $300 \text{ m}^3\text{s}^{-1}$ (···, *). . . . .   | 137 |
| 6.5  | Inflows required to maintain $X_2$ standards for the sea-level rise scenarios. Legend: Port Chicago $X_2 = 64 \text{ km}$ (—, ○), Chipps Island $X_2 = 74 \text{ km}$ (---, ◇), and Collinsville $X_2 = 81 \text{ km}$ (···, *). . . . .  | 138 |



# Chapter 1

## Introduction

### 1.1 Motivation

Estuaries such as San Francisco Bay are transitional regions that lie between salty ocean water at the mouth and freshwater upstream. The estuarine circulation is complex with interactions of strong tidal currents, bathymetric variability and density driven exchange born of the competition between ocean and fresh waters. The complexity and enormous variability in the forcing makes it difficult to study the transport of substances in estuaries, which is crucial given the variety of ecosystems in these large water bodies that traverse heavily populated areas. Estuaries are also extremely fragile environments that are highly susceptible to human activities. Understanding the dynamics of estuarine flow is therefore vital to maintain healthy estuaries throughout the world.

Numerical models are important tools in the study of circulation and transport in estuaries and coastal oceans. Two- and three-dimensional models have been applied to San Francisco Bay and extensively calibrated to yield results that match field data reasonably well (Cheng et al. 1993; Cheng and Smith 1998; Gross et al. 1999b; Gross et al. 1999a; Gross et al. 2005; Gross et al. 2009; MacWilliams and Cheng 2006; MacWilliams et al. 2007). These models are used to obtain a detailed understanding of hydrodynamics and transport in the Bay and the influence of mixing and forcing mechanisms on the circulation.

The transport and mixing of salt, pollutants, sediments and nutrients play a fundamental role in sustainable estuary management. Our ability to predict transport and mixing is limited by the accuracy of scalar advection schemes in numerical models, and the adequacy of such models to resolve physical processes. The physics that must be resolved include large scale mixing mechanisms dictated by grid resolution and small scale turbulent mixing mechanisms determined by turbulence parameterizations. Employing numerical models to isolate the effects of grid resolution, the turbulence model and the scalar advection scheme, our objective is to assess the effects of these mechanisms to enable highly accurate estuarine simulations.

This dissertation employs the coastal ocean simulator SUNTANS (Stanford Unstructured Nonhydrostatic Terrain-following Adaptive Navier-Stokes Simulator) (Fringer et al. 2006) to perform three-dimensional hydrodynamic simulations of San Francisco Bay. SUNTANS is well-suited to simulate the flow in San Francisco Bay because it employs an unstructured grid, hence enabling flow features to be resolved where there is bathymetric variability. Successful application of numerical models to San Francisco Bay depends heavily on accurate implementation of the advection scheme. An investigation into methods to quantify numerical diffusion is valuable for the development of accurate numerical modeling tools to simulate estuarine flows and predict climate change impacts.

## 1.2 San Francisco Bay

San Francisco Bay consists of two distinct subestuaries: the northern reach lies between the Golden Gate and the confluence of the Sacramento-San Joaquin Delta, and comprises San Pablo Bay, Suisun Bay and Central Bay, and South Bay extends southward from the Golden Gate to San Jose (Fig. 1.1). The only outlet to the Pacific Ocean is through the Golden Gate channel, a 1.5 km wide channel with a maximum depth of 110 m that connects the Central Bay to the Gulf of Farallones in the coastal Pacific Ocean. Carquinez Strait connects Suisun Bay to San Pablo Bay, where the deepest part of the channel is over 30 m deep. San Francisco Bay is a shallow estuary with an average depth of 2 m, consisting of large areas of intertidal mudflats in the

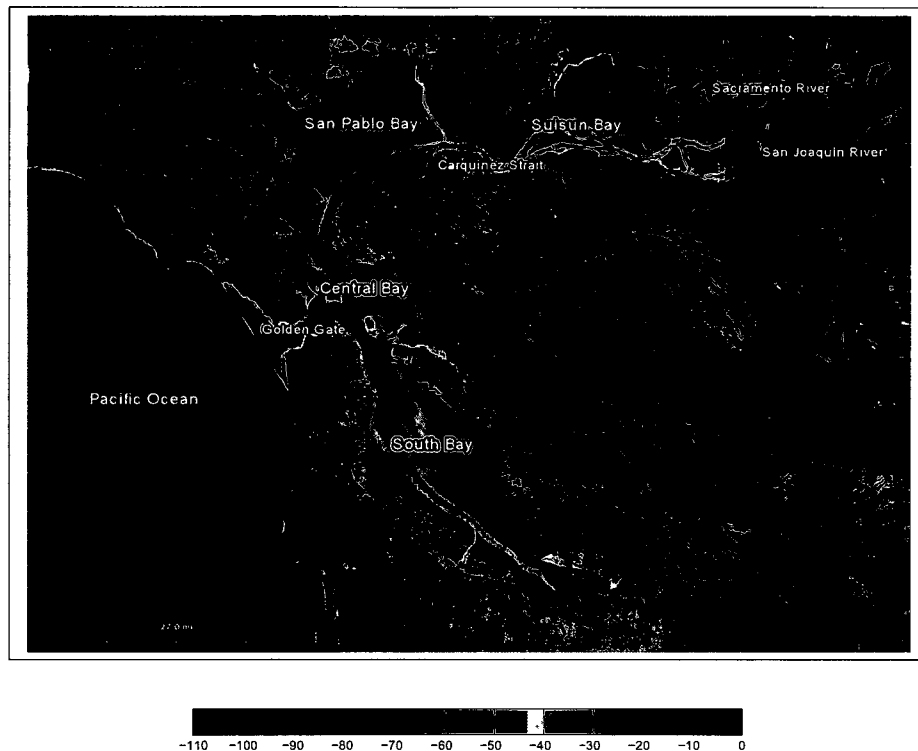


Figure 1.1: The San Francisco Bay model domain and bathymetry (in m below MSL).

eastern and southern parts of the South Bay, and the northern parts of San Pablo Bay and Suisun Bay. Along the longitudinal axis of the Bay is a narrow main channel between 10 to 18 m deep.

Spatial and temporal variability in San Francisco Bay are characterized by tides, freshwater inflows, and exchange with coastal waters (Walters et al. 1985; Conomos et al. 1985; Conomos 1979a). Tides in San Francisco Bay are mixed semi-diurnal and diurnal with pronounced spring-neap variability. The tidal prism is approximately  $1.6 \text{ km}^3$  or nearly a quarter of the total volume of the Bay. Ocean tides propagate through the narrow opening at Golden Gate, and the nature of the waves is changed by the influence of bathymetry in Central Bay as they propagate to the northern and southern reaches. Tides in the northern reach are progressive waves which are altered at the constrictions and gradually become a mixture of progressive and standing

waves. In the southern reach, tides become a standing wave when incoming tides from Central Bay are superimposed upon reflections from the south end of the Bay.

San Francisco Bay receives most of its freshwater inflows from the Sacramento-San Joaquin Delta. The Delta receives runoff from about 40 percent of the land area of California and about 50 percent of California's total streamflow. The Mediterranean climate controls seasonal patterns of freshwater inflows such that inflows are high in winter (rainfall runoff) and spring (snowmelt runoff) and low in summer. About 25 percent of the inflows are pumped into California's water system and diverted to Southern California and the Central Valley, and 10 percent of the inflows provide freshwater supplies for local domestic, industrial and agricultural use.

The northern reach of San Francisco Bay is a partially-mixed estuary dominated by seasonally varying freshwater inflows. Inflows create horizontal salinity gradients, with freshwater entering through the Delta having salinities of less than 1 psu, and salinities increasing downstream to approach 30 psu near the mouth of the estuary. The horizontal salinity gradient drives gravitational circulation as freshwater flows seaward on the surface and salty water flows landward at depth. Superimposed on this is the influence of tidal stirring and mixing, leading to tidal asymmetry that will modify the gravitational circulation in a phenomenon known as strain-induced periodic stratification (SIPS) (Simpson et al. 1990). The net effect of these processes is to adjust the longitudinal salinity gradient throughout North San Francisco Bay.

Inflows into South Bay are less than one tenth of freshwater inflows into the northern reach and are too weak to stratify the water column and create estuarine circulation. Salinities are higher and more uniform compared to the northern reach, and evaporation makes the South Bay saltier in the summer than the coastal ocean, resulting in the formation of an inverse estuary (Pritchard 1994; Nunes et al. 1990). In the winter, high inflows entering the Bay through the Delta pass through Central Bay to reach South Bay. Gravitational circulation results as fresh water on the surface flows southward over salty ocean water on the bottom.

Seasonal variability in nearshore oceanic circulation in the Pacific results in seasonal variability in the composition of the coastal waters that enter San Francisco Bay (Largier 1996), and this has important implications for seasonal phytoplankton

dynamics (Cloern and Nichols 1985). Upwelling and downwelling influence the temperature and salinity of nearshore coastal waters in San Francisco Bay. Along the California coast, coastal upwelling occurs in the summer as northerly winds cause Ekman transport (Sverdrup et al. 1942) of surface water away from the coast, and surface waters are replaced by deeper, colder and saltier ocean water (Bakun 1973; Scwing et al. 1996). Deep waters are rich in nutrients which enhance phytoplankton productivity. Downwelling reduces biological productivity and transports surface waters rich in dissolved oxygen deeper into the ocean. In the winter, southerly winds cause Ekman transport which moves surface waters towards the coast, resulting in the piling up and sinking of water known as coastal downwelling.

Ocean salinities varying by only 3 psu between summer and winter months (Conomos et al. 1979) have a smaller influence on seasonal variability in the Bay compared to inflows varying widely from 300 m<sup>3</sup>/s in the summer to 2000 m<sup>3</sup>/s in the winter. Stratification is strongest in the winter in North Bay when river inflows are highest. Salinity in the northern reaches and Central Bay is strongly influenced by Delta inflows. During periods of low inflows, sea water penetrates upstream to the confluence of the Sacramento and San-Joaquin rivers, and high inflows result in enhanced salinity stratification and gravitational circulation with a salt wedge developing around Carquinez Strait (Conomos 1979a; Kimmerer 2002).

San Francisco Bay is one of the most productive ecosystems in the world (Kimmerer 2004; Nichols et al. 1986; Conomos 1979b; Hollibaugh 1996), with large areas of salt marshes and intertidal flats that perform critical biological and environmental functions, and hence serve as an important habitat for birds, fish and wildlife. Human interference through activities such as diking of marshes, hydraulic mining and damming of rivers in the watershed have drastically reduced the area and size of the Bay, and altered the types and numbers of organisms living in the estuary. As a consequence of the loss of wetlands and changes in land use, the surface area of the Bay has decreased from 2000 to 1290 km<sup>2</sup> and the Delta from 2000 to  $9 \times 10^{-5}$  km<sup>2</sup> (Cohen 2000). Pollution is increasingly becoming a problem in the estuary as pollutant discharge from stormwater runoff, wastewater outfalls and oil spills enter the Bay. These problems are likely to be intensified with population growth and

global climate change.

## 1.3 Potential climate change impacts

We will use the numerical model of San Francisco Bay to assess the potential impacts of climate change in an estuarine environment. Trends towards urbanization have led to increasingly populated low-lying coastal areas where a large portion of economic activity is concentrated. Coastal zones are also characterized by a rich diversity of ecosystems and habitats. Sea-level rise has profound implications for coastal populations, as coastal zones are at risk of inundation and increased vulnerability to coastal flooding due to storm surges. In addition, sea-level rise has substantial impacts on freshwater resources and habitats, prompting research into possible implications for ecosystems that lie at the interface between land and ocean.

Global sea level has been increasing at an unprecedented rate over the past 100 years (Church and White 2006). Tide gauge data estimates sea-level rise to be in the range of 0.1 m to 0.2 m over the last century. In recent years, the rate of sea-level rise has increased significantly over that of previous decades (Church and White 2006). Semi-empirical models by Rahmstorf (2007) predict sea-level rise by 2100 to be on the order of 1 m exceeding estimates provided by the Intergovernmental Panel on Climate Change (IPCC 2001; IPCC 2007) of between 0.18 m to 0.59 m. The range in sea-level rise predictions in the next century is accounted for by uncertainties in global temperature projection and the rate of melting of ice sheets. Climate models and satellite data indicate that sea-level rise is not expected to be uniform around the world because of geomorphological variability.

### 1.3.1 Potential land loss and coastal flood risk

Potential land loss due to sea-level rise occurs as a result of inundation and erosion of coastal areas. Inundation maps have been employed to determine the intertidal areas that are at threat under different sea-level rise scenarios (Li et al. 2009; Cooper et al. 2008; Titus and Richman 2001; Hennecke 2004; Gornitz et al. 2001; Knowles

2010). The inundation maps are subsequently used to identify coastal populations and critical infrastructure most at risk, from which adaptation strategies can be evaluated, tested and implemented. Densely populated coastal cities indicate huge economic impacts of sea-level rise, including costs of relocation, coastal protection and reconstruction. A study of potential inundation in San Francisco Bay by Knowles (2010) shows wetlands in North Bay and developed areas in Central and South Bays, including San Francisco and Oakland International Airports are most vulnerable to inundation. A 1.0 m sea-level rise would threaten existing commercial, residential and industrial property in the Bay valued at 48 billion (in year 1990 dollars) (Heberger et al. 2009).

Sea-level rise increases the vulnerability of coastal areas to flooding due to storms surges. The effect of storm surges are superimposed over a higher mean sea level resulting in greater destructive ability of such events. Shoreline erosion directly impacts coastal communities, as beaches and dunes which serve as flood buffers are removed.

### **1.3.2 Impact on freshwater resources and habitats**

Sea-level rise leads to an increase in the salinity of surface water and ground water through salt water intrusion. Rising sea levels result in a landward shift of the estuarine salinity field, threatening freshwater supplies upstream (Williams 1987; Hull and Titus 1986). In the San Francisco Bay-Delta system which provides freshwater supplies to Southern California and the Central Valley, and for local domestic, industrial and agricultural use, salt water intrusion upstream will result in water intakes that might draw on salty water during dry periods. Coastal aquifers recharged by freshwater upstream are also likely to become saline as salt water is pushed upstream (Werner and Simmons 2009; Oude Essink 1999; Bobba 2002; Sherif and Singh 1999; Meisler et al. 1984). The availability of freshwater in coastal areas interacts with other factors, including changes to the local hydrology due to climate change (Miller et al. 2003; Dettinger et al. 2004; Knowles and Cayan 2002; Knowles and Cayan 2004), and changes in demand due to population growth and urbanization. The combination of these factors is likely to compound water stress in coastal areas.

Wetlands such as salt marshes and mangroves are located close to sea level and are particularly susceptible to sea-level rise. Wetlands perform critical biological and environmental functions, such as preserving shorelines, providing recreation and economic benefits, creating protection from storms, and serving as an important habitat for birds, fish and wildlife. Rising sea levels accelerate erosion and new wetlands are formed inland as previously dry areas are flooded (Titus 1988). The wetlands disappear if the sea level rises faster than wetlands are being formed inland (Reed 1990; Reed 1995). In developed areas, impediments to landward migration may also exist in the form of dikes, roads and buildings. Intrusion of salt water increases the salinity of habitats upstream and may have significant impacts on marine ecosystems that are unable to tolerate high salinity (Schallenberg et al. 2003; Short and Neckles 1999).

## 1.4 Hydrodynamic modeling

Hydrodynamic modeling capabilities have improved significantly in the last decade as a result of advances in computing power. In order to obtain highly accurate models, the ability to resolve physical processes is crucial. Grid resolution dictates which processes are resolved and turbulence closure models determine the parameterization of unresolved small scale turbulent mixing mechanisms. A highly efficient model compromises resolution by using a coarser grid and turbulence closure models to parameterize mixing, such as Reynolds-averaged (RANS) simulations to obtain solutions in a shorter time frame. On the other hand, direct numerical simulations (DNS) permit the full range of spatial and temporal scales of turbulence to be resolved, which makes them prohibitively expensive to implement for large-scale environmental flows. For the same grid resolution, the accuracy of different hydrodynamic models varies and is dependent on the numerical methods used to solve the governing equations. In the following sections, we review two- and three-dimensional models applied in estuaries and coastal oceans, and describe hydrodynamic modeling efforts in San Francisco Bay.



### 1.4.1 Depth-averaged models

Two-dimensional hydrodynamic models solve the depth-averaged Navier-Stokes and continuity equations using finite difference, finite volume or finite-element schemes. Such models simulate barotropic flows while ignoring baroclinic effects. The development of depth-averaged hydrodynamic models in estuaries began with explicit numerical methods (Leendertse 1967). Such schemes have a time step limitation based on the CFL condition associated with the speed of propagation of fast free-surface gravity waves, resulting in a computationally inefficient approach. More recently, Casulli (1990) solved the two-dimensional shallow water equations numerically with a semi-implicit scheme, which has the advantage of being more robust and computationally efficient.

Two-dimensional simulations are sufficient to understand the tidal pumping mechanism, which results mostly from tidal asymmetry of the currents. Signell and Butman (1992) employed the two-dimensional TRIM model (Casulli 1990) to simulate horizontal exchange of water between Boston Harbor and the coastal ocean. By tracking Lagrangian particles, they showed that dispersive characteristics are extremely sensitive to the location and timing of the release of particles. Their simulations matched well with residual current data near the inlet of the Harbor, yet deviated from data on the shelf outside the Harbor, indicating the importance of density-driven currents.

### 1.4.2 Three-dimensional models

Baroclinic effects are included in three-dimensional models. Such models resolve vertical variations in velocity and scalar concentrations, allowing processes such as vertical shear flow dispersion, vertical steady exchange and stratification to be included. The major differences among three-dimensional models are in the choices of the turbulence closure schemes, vertical coordinate systems and numerical methods for time-advancement.

The use of turbulence closure schemes in three-dimensional models enables the

parameterization of turbulence with an eddy-viscosity and eddy-diffusivity. Two-equation turbulence models such as the  $k - \epsilon$  model,  $k - \omega$  model and  $k - kl$  model are widely used. The most popular model is the Mellor-Yamada level 2.5 turbulence closure model (Mellor and Yamada 1982), which has been successfully implemented in the POM coastal ocean model by Blumberg and Mellor (1987). Two-equation models solve two partial differential equations to compute the turbulent velocity scale and length scale. The performance of turbulence closure models implemented using a generic length scale method ( $k - kl$ ,  $k - \epsilon$ ,  $k - \omega$ ) was compared in an application to the Hudson river estuary (Warner et al. 2005). The authors showed that numerical simulations of estuarine stratification are relatively insensitive to the choice of the turbulence closure schemes, although the stability functions that determine the influence of stratification can be important.

A range of vertical coordinate systems have been implemented in ocean models, including the  $z$ -coordinate in SUNTANS (Fringer et al. 2006), the sigma-coordinate in POM (Mellor 1996) and the  $s$ -coordinate in ROMS (Shchepetkin and McWilliams 2005). Terrain-following coordinates have the advantage of providing smooth representation of bottom topography. The sigma coordinate is equidistant in the vertical, while the  $s$ -coordinate is stretched vertically to provide higher resolution near the surface, and consequently a better representation of the mixed layer. The terrain-following coordinates, however, lend themselves to a pressure gradient error giving rise to unrealistic flows, which does not arise with the  $z$ -coordinate (Haney 1991). Methods to reduce the pressure gradient error in terrain-following coordinates are described in Shchepetkin and McWilliams (2005).

A popular choice for three-dimensional models is to use a mode-splitting algorithm for time-advancement (Blumberg and Mellor 1987). Using this approach, a splitting algorithm is employed for the external or barotropic and internal or baroclinic modes to reduce computational effort. The external mode (two-dimensional vertically integrated equations) is solved independently from the internal mode (full three-dimensional equations). The stability requirement for the external mode is related to the free surface gravity wave propagation and is governed by the CFL (Courant-Friedrichs-Levy) condition, hence requiring the use of a small time step. The internal

mode is related to the internal wave propagation, and stability is achieved by using a larger time step. Mode-splitting can result in inconsistencies between the internal and external modes (Higdon and Bennett 1996; Hallberg 1997). Casulli and Cheng (1992) introduced a semi-implicit formulation to directly solve the three-dimensional governing equations without requiring any form of splitting. Employing the Eulerian-Lagrangian discretization for advection of momentum, the algorithm is very stable and permits the use of large time steps to improve computational efficiency.

### 1.4.3 San Francisco Bay

A range of numerical models have been applied to simulate circulation in San Francisco Bay. These include cross-sectionally-averaged one-dimensional models, depth-averaged two-dimensional models and three-dimensional models capable of simulating the full flow field. Earlier models of San Francisco Bay are one-dimensional, such as the Delta Simulation Model (DSM2) and the link-node model. DSM2 is a one-dimensional, water quality and particle-tracking model developed by the California Department of Water Resources (Anderson and Mierzwa 2002), which has been primarily applied in the Sacramento-San Joaquin Delta for particle tracking purposes (Kimmerer and Nobriga 2008; Sommer et al. 1993). Link-node models discretize the flow domain into channel links connected by nodes. Nelson and Lerseth (1972) applied a linked-node model to South San Francisco Bay.

Finite-volume and finite-element methods are employed in two- and three-dimensional models. The RMA (Resource Modelling Associates)-based models, such as RMA-2V and RMA-10 employ finite-element methods for estuarine hydrodynamics and salt transport (King and Norton 1978; King 1993). King and Rachiele (1990) performed a modeling study of the San Francisco Bay-Delta system using RMA-10 to evaluate the impacts of channel geometry on salinity intrusion and currents. Finite-volume methods were introduced in San Francisco Bay with the Semi-Implicit-3D Model (SI-3D) and the TRIM family of models. Smith (2006) developed SI-3D to simulate density-driven gravitational circulation and applied the model to perform three-dimensional particle tracking in the San Francisco estuary (Smith et al. 2005).

The TRIM family of models have been extensively applied to San Francisco Bay. Cheng et al. (1993) developed a two-dimensional depth-averaged model of San Francisco Bay with TRIM2D (Casulli 1990), which is calibrated and validated with a large set of surface elevation and current data. The two-dimensional TRIM model has been implemented in the San Francisco Bay Marine Nowcast System (Cheng and Smith 1998), and realtime Nowcast model results are available for download. The TRIM3D model (Casulli and Cattani 1994) (three-dimensional version of TRIM2D) has been applied to San Francisco Bay to study hydrodynamics resulting from salinity-induced baroclinic circulation. A conservative transport method and a two-equation turbulence closure model were added to TRIM3D by Gross et al. (1999b), and the resulting model was used to investigate the effects of stratification in South Bay. Gross et al. (2009) presented the results of TRIM3D as applied to the entire San Francisco Bay, and details of the calibration are presented along with an assessment of model performance which performs extremely well throughout the Bay. The UnTRIM model (Casulli and Walters 2000), which is the unstructured version of TRIM3D and is the methodology (i.e., numerical method, unstructured grids) upon which the SUNTANS model (Fringer et al. 2006) is based, has also been applied to San Francisco Bay by MacWilliams and Cheng (2006).

## 1.5 Mixing mechanisms in estuaries

In this section, we review mixing processes in estuaries which range from turbulent mixing at small scales to dispersive mechanisms associated with tides, winds and density-driven flows at large scales. To compare the relative importance of various dispersion mechanisms, we investigate the salt balance from the cross-sectionally and tidally-averaged advection-diffusion equation.

Cross-sectionally and tidally-averaged salt transport can be described quantitatively using the advection-diffusion equation, with rivers advecting salt seaward and dispersive processes carrying salt into the Bay. The net exchange is given by

$$\frac{\partial \langle \bar{s} \rangle}{\partial t} = - \langle \bar{u} \rangle \frac{\partial \langle \bar{s} \rangle}{\partial x} + \frac{\partial}{\partial x} \left( K \frac{\partial \langle \bar{s} \rangle}{\partial x} \right), \quad (1.1)$$

where  $\langle \cdot \rangle$  indicates tidal averaging,  $\bar{\cdot}$  indicates cross-sectional averaging,  $u$  is the along-channel velocity,  $s$  is salinity,  $x$  is the coordinate along the main channel and  $K$  is the longitudinal dispersion coefficient. The first term on the right-hand side describes advective flux, and the second term describes dispersive flux. The dispersive flux mechanisms include shearflow dispersion, steady exchange and tidal pumping/tidal trapping. The steady exchange resulting from vertical structure is attributed to gravitational circulation created by longitudinal salinity gradients.

### 1.5.1 Salt flux decomposition

The classical approach to decomposing estuarine salt fluxes follows the method in Fischer et al. (1979). The decomposition of the velocity and salinity profiles is given by

$$u(x, y, z, t) = u_a + u_c(x, t) + u_s(x, y, z) + u'(x, y, z, t), \quad (1.2)$$

$$s(x, y, z, t) = s_a + s_c(z, t) + s_s(x, y, z) + s'(x, y, z, t), \quad (1.3)$$

where  $u_a = \langle \bar{u} \rangle$  and  $s_a = \langle \bar{s} \rangle$  are cross-sectionally and tidally-averaged terms,  $u_c = \bar{u} - u_a$  and  $s_c = \bar{s} - s_a$  are cross-sectionally averaged and tidally varying terms,  $u_s = \langle u \rangle - u_a$  and  $s_s = \langle s \rangle - s_a$  are tidally-averaged and cross-sectionally varying terms, and  $u'$  and  $s'$  are cross-sectionally and tidally varying terms. The subtidal salt flux is then given by

$$F = \langle \bar{u}\bar{s} \rangle = u_a s_a + \langle u_c s_c \rangle + \overline{u_s s_s} + \langle u' s' \rangle. \quad (1.4)$$

The first term on the right-side is identified as the advection term, which removes salt from the estuary, and the remaining three are dispersive terms, which add salt to the estuary.  $\langle u_c s_c \rangle$  is the tidal flux,  $\overline{u_s s_s}$  is the exchange flux and  $u' s'$  is the oscillatory shear flow.

### 1.5.2 Shear flow dispersion

Shear flow dispersion in estuaries is determined from shear flow dispersion in rivers with the addition of an oscillatory component (Fischer et al. 1979). The longitudinal dispersion coefficient due to shear flow in rivers is given by

$$K = I u_{dev}^2 T_c, \quad (1.5)$$

where  $T_c = W^2/\epsilon_H$  is the time scale for transverse mixing,  $W$  is the width of the channel,  $\epsilon_H$  is the horizontal eddy diffusivity,  $u_{dev}$  is the deviation of mean flow velocity from the cross-sectional variation of the depth-averaged velocity, and  $I \approx 0.1$ . This is applicable only if the oscillating period is longer than  $T_c$ , ie.  $T \gg T_c$ , the cross-section is wide and shallow, and density effects are absent. For the case that the period is shorter than  $T_c$ , ie.  $T \ll T_c$ , there is no shear flow dispersion, since transverse variations produced by the shear are eliminated when the flow reverses.

The longitudinal dispersion coefficient in an estuary due to shear flow (Fischer et al. 1979) is given by

$$K = 0.1 \bar{u}^2 T [(1/T') f(T')], \quad (1.6)$$

where  $T' = T/T_c$  is the dimensionless time scale for cross-sectional mixing, and the function  $f(T')$  has a maximum of approximately 0.8 when  $T' \approx 1$ , and has the limits  $f(T') \rightarrow (1/T')$  for  $T' \gg 1$  and  $f(T') \rightarrow 2.6T'$  for  $T' \ll 1$ .

### 1.5.3 Tidal pumping/trapping

Geometrical variations result in tidal pumping and tidal trapping mechanisms for horizontal mixing in estuaries. In large estuaries, tidal pumping can result as a consequence of Earth's rotation, as currents are deflected to the right in the Northern hemisphere and to the left in the Southern hemisphere. A net counter-clockwise circulation results in the Northern hemisphere as flood and ebb currents are deflected toward the right and left banks, respectively, as viewed by the flood currents.

Tidal pumping is also caused by the interaction of tidal flow with irregular bathymetry at a constriction (Stommel and Farmer 1952). Ebb currents flow into the ocean as a

confined jet, while the flood currents draw flow radially from all around the mouth as a potential sink. The jet-sink structure creates lateral salinity gradients, which results in a net exchange of scalars. In San Francisco Bay, the jet-sink structure is observed in the area between Golden Gate and the offshore sand bar (Largier 1996). The tidal outflow jet is scaled by the width of the channel at the westernmost end of the mouth and will extend about 15 km offshore.

The effects of side embayments and small branching channels on dispersion is termed tidal trapping. The trapping mechanism occurs as the phases of currents in the side channels are different from the main channel producing a net horizontal dispersion (Schijf and Schonfeld 1953). Okubo (1973) suggested a model for the trapping mechanism. Parameterizing for a tidal flow with velocity  $u = u_0 \cos(\omega t)$ , a trap to channel volume ratio of  $r_v$  and a characteristic residence time in the trap of  $k^{-1}$ , the effective longitudinal dispersion coefficient is given by

$$K = \frac{K'}{1 + r_v} + \frac{r_v u_0^2}{2k(1 + r_v)^2(1 + r_v + \sigma/k)}, \quad (1.7)$$

where  $K'$  is the longitudinal dispersion coefficient in the main channel.

#### 1.5.4 Gravitational circulation

The steady exchange resulting from salt water flowing landward along the bottom and fresh water flowing seaward at the surface is referred to as gravitational circulation (Hansen and Rattray 1965). This baroclinic flow is driven by a longitudinal density gradient in estuaries. The strength of gravitational circulation can be estimated by assuming a balance between friction and the baroclinic pressure gradient caused by the longitudinal salinity gradient (Hansen and Rattray 1965),

$$\frac{1}{\rho} \frac{\partial P}{\partial x} \sim \epsilon \frac{\partial^2 u}{\partial z^2}, \quad (1.8)$$

where  $P = \rho(1 + \beta s)gH$  is the pressure,  $\rho$  is the density,  $s$  is salinity,  $g$  is the acceleration due to gravity,  $\beta$  is the coefficient of salt expansivity,  $H$  is the water depth,  $\epsilon$  is the eddy diffusivity,  $x$  is measured upstream from the mouth of the estuary

and  $z$  is measured upward from the water surface. Eq. (1.8) can be used to derive a velocity scale for the exchange flow (Monismith et al. 2002)

$$U_{\text{GC}} \sim \frac{\beta g \frac{\partial s}{\partial x} H^3}{\epsilon}, \quad (1.9)$$

where  $\frac{\partial s}{\partial x}$  is the longitudinal salinity gradient. The balance between horizontal advection of the salinity gradient and vertical diffusion of the vertically varying salinity perturbation,  $s'_V$ , defined as  $s_V = \overline{s_V} + s'_V(z)$  is

$$U_{\text{GC}} \frac{\partial s}{\partial x} \sim \epsilon \frac{\partial^2 s'_V}{\partial z^2}, \quad (1.10)$$

so that

$$s'_V \sim \frac{\beta g \left(\frac{\partial s}{\partial x}\right)^2 H^5}{\epsilon^2}. \quad (1.11)$$

The along-channel salt flux due to the gravitational circulation is then approximated with

$$F = U_{\text{GC}} s'_V \sim \frac{(\beta g)^2 \left(\frac{\partial s}{\partial x}\right)^3 H^8}{\epsilon^3}. \quad (1.12)$$

The strength of the exchange flow varies over the tidal time scale and with neap-spring variability. During neap tides, vertical mixing is weak leading to higher vertical stratification, which further decreases vertical mixing and causes stronger gravitational circulation. On the tidal time scale, gravitational circulation is reinforced through tidal shear. Simpson et al. (1990) introduced the term tidal straining to describe the situation in which the oscillatory vertical shear of a tidal boundary layer flow acts on the horizontal salinity gradient to produce tidal variations in stratification. During ebb tides the stabilizing buoyancy flux decreases mixing, leading to a nonlinear feedback mechanism between stratification and vertical mixing. During flood tides the destabilizing buoyancy flux increases vertical mixing to destratify the water column. The phenomenon is known as strain-induced periodic stratification (SIPS). Observations by Stacey et al. (2008) and Geyer et al. (2000) confirmed the presence of tidal variations in mixing intensity due to straining in real estuaries, while



Burchard and Rennau (2007) employed a two-dimensional model to demonstrate the phenomenon.

The balance between turbulent mixing and stratification determines the conditions in which SIPS occurs, and Monismith et al. (1996) defined the horizontal Richardson number  $Ri_x$  to parameterize the onset of stratification

$$Ri_x = \frac{\beta g \frac{\partial s}{\partial x} H^2}{u_*^2}, \quad (1.13)$$

where  $u_*$  is the friction velocity. When  $Ri_x$  is greater than the critical value which is approximately 0.25 in San Francisco Bay, runaway stratification occurs. Runaway stratification refers to a numerical artifact in which stratification grows indefinitely.

### 1.5.5 Tidal random walk

A conceptual model proposed by Zimmerman (1986) describes the interaction of the tidal flow with a deterministic system of residual eddies generated by variations in topography. Lagrangian trajectories associated with such a flow are extremely complex, with particles exhibiting a “tidal random walk”. An effective dispersion coefficient for the “tidal random walk” has the form

$$K = B(\nu_E, \lambda_L) U_{\text{tide}} L_{\text{tide}}, \quad (1.14)$$

where  $U_{\text{tide}}$  is the velocity of the tidal flow,  $L_{\text{tide}}$  is the tidal excursion length,  $\nu_E$  is the ratio of the energy of the eddies to the tidal flow, and  $\lambda_L$  is the ratio of the tidal excursion length to the eddy size. The function  $B(\nu_E, \lambda_L) \rightarrow 1$  as  $\nu_E \rightarrow 1$  and  $\lambda_L \rightarrow 1$ . Based on this theory, Zimmerman (1976) demonstrated the presence of chaotic stirring in the Dutch Wadden Sea, and computed dispersion coefficients that match observations.

### 1.5.6 Horizontal turbulent mixing

Three-dimensional turbulent motions provide a mechanism for horizontal dispersion in estuaries. The horizontal turbulent diffusivity has the form

$$K = C_1 u_* H, \quad (1.15)$$

where  $C_1$  is a constant between 0.4 and 0.6 (Fischer et al. 1979),  $u_*$  is the friction velocity and  $H$  is the water depth. The horizontal turbulent diffusivity is  $0.002 - 0.06 \text{ m}^2/\text{s}$ , and several orders of magnitude smaller than typical values of horizontal mixing coefficients for estuaries, which are in the range  $50 - 200 \text{ m}^2/\text{s}$  (Signell and Geyer 2007).

## 1.6 Modeling scalar transport

Transport of salt, heat, nutrients, pollutants and organisms in surface waters play a fundamental role in maintaining healthy coastal and ocean environments. Our ability to predict transport in surface water flows is limited by available computing resources to accurately simulate fluid dynamical processes using numerical models. Quantification of numerical diffusion is crucial to assess the performance of low-and-high order advection schemes in order to select a scalar advection scheme with desirable properties. The development and implementation of numerical modeling tools to accurately simulate surface water flows and predict environmental impacts is dependent on the choice of an effective scalar advection scheme.

A review of advection schemes in ocean general circulation models is provided in Gerdes et al. (1991). They found that the main properties relevant for climate simulations depend not only on the formulation of the mixing parameterization, but also on the the choice of the advection scheme. Gross et al. (1999a) evaluated advection schemes for simple test cases and estuarine salinity simulations in South San Francisco Bay. Comparisons of the advection schemes showed that results for simple test cases differ from those of the estuarine simulations, where the most important properties for accurate salinity predictions in dispersive regions are stability and mass

conservation. The performance of advection schemes in estuarine simulations varies with location, and large numerical errors are expected with first-order upwinding in less dispersive regions, even though the performance of first-order upwinding is comparable to higher-order schemes in dispersive regions. Smaoui and Radi (2002) employed a three-dimensional ocean model to simulate the dynamics of the English Channel. A comparison of advection schemes shows the flux-limiting schemes are effective in reducing numerical diffusion present in first-order upwinding, and also in eliminating oscillations caused by non-limiting higher-order schemes.

An analytical derivation of numerical diffusion on Cartesian grids was proposed by Hirt (1968) using heuristic stability theory. The author investigated the computational stability of finite difference equations by determining the modified partial differential equation for a simple linear equation and a set of coupled nonlinear equations. Expanding each of the terms in a Taylor series, the finite-difference equation is reduced to a differential equation. The lowest-order terms in the expansion represent the modified partial differential equation, and the higher-order terms refer to truncation errors which are used to determine the order of accuracy and consistency. Using the modified equation, Warming and Hyett (1974) characterized the dissipative and dispersive properties of a scheme, and established connections between the modified equation and the von Neumann method. Difficulties in employing Hirt analysis (Hirt 1968) on unstructured grids exist due to asymmetries between two types of cells. As a consequence, neighbouring cells may not be characterized by the same modified equation which leads to inconsistency (Bouche and Ghidaglia 2005). On nonuniform Cartesian grids and Curvilinear grids, inconsistent discretizations also arise if the grid spacing is not quasi-uniform and the dependent variables are defined at the center of the cells (Turkel 1986).

In numerical models of ocean circulation, the time evolving, spatially varying flow makes it close to impossible to analytically derive numerical diffusion coefficients associated with the transport of scalars. This has led to the introduction of a variety of methods aimed at assessing numerical diffusion properties in ocean models. Burchard and Rennau (2007) implemented a method to calculate physical and numerical mixing of tracers in ocean models. They defined physical mixing as the turbulent mean scalar

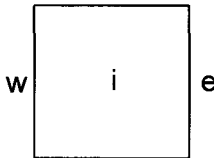


Figure 1.2: Cell  $i$  with east and west faces indicated by  $e$  and  $w$ , respectively.

variance decay rate and numerical mixing due to discretization errors of the transport scheme as the difference in decay rate between the advected square of the tracer variance and the square of the advected scalar. The diagnostic method was applied to the Western Baltic Sea, where numerical mixing was shown to have a magnitude comparable to physical mixing (Rennau and Burchard 2009).

### 1.6.1 Scalar advection schemes

In this section we describe advection schemes by considering the one-dimensional discretization of the scalar advection equation with constant velocity  $u_0$ . Using an explicit time discretization on a Cartesian grids yields

$$\frac{s_i^{n+1} - s_i^n}{\Delta t} + u_0 \frac{s_e^n - s_w^n}{\Delta x} = 0 \quad (1.16)$$

where  $s_i$  are cell-centered quantities,  $s_e$  and  $s_w$  are respectively quantities on the east and west cell faces (Fig. 1.2),  $\Delta t$  is the time step and  $\Delta x$  is the width of cell  $i$ .

#### First-order upwind

For first-order upwinding, the quantity  $s_e$  is set equal to the cell centered value  $s_i$  in the upwind cell given by

$$s_e = \begin{cases} s_i & u_0 > 0, \\ s_{i+1} & \text{otherwise,} \end{cases} \quad (1.17)$$

and it is assumed that  $s_e(i-1) = s_w(i)$ . First-order upwinding is stable if the CFL condition is satisfied, i.e.,

$$0 \leq C_0 \leq 1, \quad (1.18)$$

where  $C_0 = u_0 \Delta t / \Delta x$  is the Courant number. A first-order forward in time and first-order backward in space (FTBS) discretization of Eq. (1.16) on a uniform Cartesian grid gives

$$s_i^{n+1} = (1 - C_0)s_i^n + C_0 s_{i-1}^n. \quad (1.19)$$

By performing a Hirt analysis (Hirt 1968) and substituting the Taylor-series expansions to obtain  $s_i^{n+1}$  and  $s_{i-1}^n$  in terms of time and space derivatives at  $i$  and  $n$ , the modified partial differential equation of the discretization (1.19) is given by, to  $O(\Delta x^2, \Delta t^2)$ ,

$$\frac{\partial s}{\partial t} + u_0 \frac{\partial s}{\partial x} = k_{xx} \frac{\partial^2 s}{\partial x^2}, \quad (1.20)$$

where the numerical diffusion coefficient is given by

$$k_{xx} = \frac{1}{2} u_0 \Delta x (1 - C_0) = \frac{1}{2} \frac{\Delta x^2}{\Delta t} C_0 (1 - C_0). \quad (1.21)$$

The truncation errors show that first-order upwinding is first-order accurate in space and time. First-order upwinding is highly diffusive with the presence of a diffusion term in the truncation errors, which acts to smooth gradients in the flow. The numerical diffusion coefficient gives positive diffusion under the same criteria as the stability constraint.

### Second-order schemes

A second-order scheme based on that of Lax and Wendroff (1960) can be derived with the quantity  $s_e$  given by

$$s_e = \frac{1}{2}(s_i + s_{i+1}) + \frac{1}{2}\psi(1 - C_0)(s_{i+1} - s_i), \quad (1.22)$$

where  $\psi$  is a limiter function satisfying  $0 \leq \psi \leq 2$ . The discretization of Eq. (1.16) on a Cartesian grid gives

$$s_i^{n+1} = s_i^n - \frac{1}{2}C_0 (s_{i+1}^n - s_{i-1}^n) + \frac{1}{2}\psi C_0^2 (s_{i+1}^n - 2s_i^n + s_{i-1}^n). \quad (1.23)$$

By performing a Hirt analysis (Hirt 1968), the modified partial differential equation of the discretization is given by,  $O(\Delta x^3, \Delta t^3)$ ,

$$\frac{\partial s}{\partial t} + u_0 \frac{\partial s}{\partial x} = k_{\text{xx}} \frac{\partial^2 s}{\partial x^2} + k_{\text{xxx}} \frac{\partial^3 s}{\partial x^3}, \quad (1.24)$$

where the numerical diffusion coefficient is given by

$$k_{\text{xx}} = \frac{1}{2} u_0 \Delta x C_0 (\psi - 1) = \frac{1}{2} \frac{\Delta x^2}{\Delta t} C_0^2 (\psi - 1), \quad (1.25)$$

and the numerical dispersion coefficient is given by

$$k_{\text{xxx}} = -\frac{1}{6} u_0 \Delta x^2 (1 - C_0^2) = -\frac{1}{6} \frac{\Delta x^3}{\Delta t} C_0 (1 - C_0^2). \quad (1.26)$$

When  $\psi = 0$ , Eq. (1.23) reduces to the central-differencing scheme, which introduces negative diffusion and is unstable. By setting  $\psi = 1$ , Eq. (1.23) reduces to the Lax-Wendroff scheme (Lax and Wendroff 1960). This introduces antidiffusion that exactly cancels the first-order diffusion and produces a second-order dispersion. For stability, the Courant number must satisfy  $0 \leq C_0 \leq 1$ , which ensures negative dispersion. While more accurate, the Lax-Wendroff scheme produces oscillations due to the numerical dispersion. These oscillations can be eliminated by adjusting the amount of antidiffusion in a way that satisfies the Total Variation Diminishing (TVD) constraint (Harten 1983). In five-point one-dimensional TVD schemes, the leading error is diffusive but the coefficient is second-order in  $\Delta x$ .

### **Total-variation diminishing**

The interpolated face value using the TVD scheme is written as the sum of a lower-order first-order upwind term and a higher-order anti-diffusive term. Application of a limiter function to the anti-diffusion term removes excessive diffusion and prevents the generation of oscillations. The quantity at  $s_e$  is given by, assuming  $u_0 > 0$ ,

$$s_f = s_i + \frac{1}{2} \phi (1 - C_f) (s_{i+1} - s_i), \quad (1.27)$$

where  $\phi$  is the limiter function, and  $C_f$  is the Courant number at a cell face. The TVD scheme limits the magnitude of  $\phi$  such that the total variation does not increase in time (Roe 1984; Sweby 1984),

$$\text{TV}(s^{n+1}) \leq \text{TV}(s^n), \quad (1.28)$$

where

$$\text{TV}(s_i^n) = \sum_{i=1}^N |s_i - s_{i-1}|. \quad (1.29)$$

The TVD scheme ensures that the method is monotonicity preserving, which implies that no new extrema can be created within the domain. The maximum value of the advected quantity is non-increasing, and the minimum value is non-decreasing. The limiter function  $\phi(r)$  (Sweby 1984) is defined by

$$\phi(r) = \begin{cases} 0 & \text{First-order upwind,} \\ 1 & \text{Lax-Wendroff,} \\ \max(0, \min(2r, 1), \min(r, 2)) & \text{Superbee,} \\ \frac{r+|r|}{1+r} & \text{Van Leer,} \\ \min(r, 1) & \text{Minmod.} \end{cases} \quad (1.30)$$

The ratio of the upwind to the local gradient  $r_{i+1/2}$  is given by

$$r_{i+1/2}^+ = \frac{s_i - s_{i-1}}{s_{i+1} - s_i} \quad u > 0, \quad (1.31)$$

$$r_{i+1/2}^- = \frac{s_{i+2} - s_{i+1}}{s_{i+1} - s_i} \quad \text{otherwise.} \quad (1.32)$$

The specification of a limiter function  $\phi$  determines how diffusive or compressive a scheme is. The larger the value of  $\phi$  within the TVD region, the more compressive the scheme. Among the TVD schemes, the Superbee scheme is the most compressive, while Minmod is the most diffusive.

## Unstructured grids

The first-order upwind scheme is simple and monotonic, which makes it easy to implement on unstructured grids. Fringer et al. (2006) used first-order upwinding for scalar transport in SUNTANS, where cell-centered quantities of the upwind cell are interpolated onto cell faces. First-order upwinding introduces excessive diffusion resulting in the smearing of gradients in the flow. This led to the development of TVD schemes which are capable of maintaining sharp fronts on unstructured grids.

The implementation of TVD schemes on unstructured grids is complicated by the difficulty in implementing and enforcing a monotonicity criteria that relies on directional next-neighbor information. This information is readily available for Cartesian grids, but missing on unstructured grids. A number of approaches have been introduced to circumvent this difficulty, including schemes developed by Barth (1993) with varying degrees of success. More recently, Casulli and Zanolli (2005) proposed a TVD scheme for scalar transport in free-surface flows, which is mass conservative and satisfies the max-min property.

## 1.7 Dissertation roadmap

This work employs the SUNTANS model (Fringer et al. 2006) to perform three-dimensional hydrodynamic simulations of San Francisco Bay to improve our understanding of transport and circulation in estuaries. In Chapter 2, the setup and implementation of the SUNTANS model as applied to San Francisco Bay is described. Details of the calibration are presented, and model performance is assessed via validation against observations of sea-surface heights, currents and salinity at several locations throughout the Bay. A TVD scalar transport scheme is implemented and the results are compared to those using first-order upwinding. In Chapter 3, a sensitivity study is performed to determine the effects of grid resolution, the turbulence model, and the scalar transport scheme on salinity simulations in North San Francisco Bay. In Chapter 4, an analytical method is presented to derive numerical diffusion



coefficients on unstructured grids. Difficulties in analytically deriving diffusion coefficients for more general flow and triangulation conditions led to the development of a domain-averaged formulation to compute numerical diffusion coefficients. In Chapter 5, the domain-averaged formulation is employed to assess the performance of the high- and low- order schemes in San Francisco Bay in order to investigate the effects of tidal dispersion and time scales on numerical diffusion. In Chapter 6, the numerical model is employed to assess the implications of sea-level rise and hydrologic changes on salinity intrusion and estuarine circulation in North San Francisco Bay.

# Chapter 2

## San Francisco Bay numerical model

### 2.1 Introduction

In this chapter, we describe the setup and implementation of the SUNTANS model as applied to San Francisco Bay. Details of the calibration are presented, and model performance is assessed via validation against observations of sea-surface heights, currents, and salinity at several locations throughout the Bay. This chapter is a modified version of the published manuscript Chua and Fringer (2011).

### 2.2 Governing equations and numerical method

We employ the SUNTANS model (Fringer et al. 2006) to simulate the flow in San Francisco Bay. SUNTANS is a parallel nonhydrostatic coastal ocean solver that uses a finite-volume formulation to solve the hydrodynamics and scalar transport equations. Although SUNTANS is a nonhydrostatic model, the present implementation is hydrostatic since the dynamics of interest are strongly hydrostatic. The governing

equations are the three-dimensional, Reynolds-averaged primitive equations:

$$\frac{\partial u}{\partial t} + \nabla \cdot (\mathbf{u}u) - fv = -g \frac{\partial h}{\partial x} - g \frac{\partial r}{\partial x} + \nabla_H \cdot (\nu_H \nabla_H u) + \frac{\partial}{\partial z} \left( \nu_V \frac{\partial u}{\partial z} \right), \quad (2.1)$$

$$\frac{\partial v}{\partial t} + \nabla \cdot (\mathbf{u}v) + fu = -g \frac{\partial h}{\partial y} - g \frac{\partial r}{\partial y} + \nabla_H \cdot (\nu_H \nabla_H v) + \frac{\partial}{\partial z} \left( \nu_V \frac{\partial v}{\partial z} \right), \quad (2.2)$$

where the free-surface height is  $h$ , the velocity vector is  $\mathbf{u}$  and  $u(x, y, z, t)$  and  $v(x, y, z, t)$  are the Cartesian velocity components in the  $x$  and  $y$  directions, and the vertical velocity  $w(x, y, z, t)$  in the vertical  $z$  direction is computed via continuity:

$$\nabla \cdot \mathbf{u} = 0. \quad (2.3)$$

The baroclinic head is given by

$$r = \frac{1}{\rho_0} \int_z^h \rho dz, \quad (2.4)$$

where  $\rho_0$  is the constant reference density and the total density is given by  $\rho_0 + \rho$ . The Coriolis term is given by  $f = 2\Omega \sin \phi$ , where  $\phi$  is the latitude and  $\Omega$  is the angular velocity of the earth. The horizontal and vertical eddy-viscosities are given by  $\nu_H$  and  $\nu_V$ , respectively. The free-surface evolves according to the depth-averaged continuity equation:

$$\frac{\partial h}{\partial t} + \frac{\partial}{\partial x} \left( \int_{-d}^h u dz \right) + \frac{\partial}{\partial y} \left( \int_{-d}^h v dz \right) = 0. \quad (2.5)$$

The density perturbation,  $\rho$ , is computed with a linear equation of state in terms of the salinity  $s$  using  $\rho = \rho_0(1 + \beta(s - s_0^R))$ , where  $\rho_0$  and  $s_0^R$  are reference states and  $\beta = 7.5 \times 10^{-4} \text{ psu}^{-1}$  is the coefficient of salt expansivity. The effects of temperature on the stratification are neglected. The transport equation for salinity neglects horizontal diffusion and is given by

$$\frac{\partial s}{\partial t} + \nabla \cdot (\mathbf{u}s) = \frac{\partial}{\partial z} \left( \epsilon_V \frac{\partial s}{\partial z} \right), \quad (2.6)$$

where  $\epsilon_V$  is the vertical turbulent eddy diffusivity. These equations are solved using the methods described in Fringer et al. (2006), in which the free-surface height, vertical diffusion of momentum, and vertical scalar advection are advanced implicitly with the theta-method, and all other terms are advanced with the second-order Adams-Bashforth method. For advection of momentum, the Eulerian-Lagrangian method (ELM) is employed and is crucial for successful applications that incorporate wetting and drying (Wang et al. 2008).

### 2.2.1 Bottom shear stress and turbulence closure

The quadratic drag law is applied at the bottom boundary to compute the bottom stress with

$$\tau_b = \rho_0 C_d U_1 \mathbf{u}_1, \quad (2.7)$$

where  $\mathbf{u}_1$  is the horizontal velocity vector in the first grid cell above the bed and  $U_1 = \sqrt{\mathbf{u}_1 \cdot \mathbf{u}_1}$  is its magnitude, and the drag coefficient  $C_d$  is computed from the bottom roughness parameter  $z_0$  with:

$$C_d = \left[ \frac{1}{\kappa} \ln \left( \frac{z_1}{z_0} \right) \right]^{-2}. \quad (2.8)$$

Here,  $z_1$  is the location of  $U_1$  at a distance of one-half the bottom-most vertical grid spacing above the bed, and the roughness coefficient  $z_0$  is adjusted to calibrate the three-dimensional model. The surface elevations are relatively insensitive to the choice of  $z_0$ , and  $z_0$  is chosen so that the predicted velocities show a good level of agreement. No further tuning of  $z_0$  is required for salinity calibrations. A spatially-varying  $z_0$  is used, such that in the Bay,  $z_0 = 0.001$  mm, and in shallow regions (with depths less than 1.0 m),  $z_0 = 1$  mm. No interpolation of  $z_0$  is done, as we found that smooth transition over depths did not significantly change our results. Areas of marshland in San Pablo Bay and Suisun Bay account for the larger values of  $z_0 = 1$  mm, as intense vegetation in these shallow shoal regions can significantly increase the bottom drag (Nepf 1999). Similar values of  $z_0$  are used for the intertidal zone by Wang et al. (2008) and for depths less than 2.0 m in simulations of South Bay by Gross et al. (1999b).

Estimates of  $z_0$  by Cheng et al. (1999) show substantial variability of between 10 mm and 0.01 mm. Our choice of  $z_0 = 0.001$  mm is smaller than values used by Gross et al. (1999b) in South Bay ( $z_0 = 0.02$  mm) and from field experiments (Cheng et al. 1999), though it may be necessary to partially compensate for errors due to numerical diffusion when using ELM for advection of momentum (Wang et al. 2008).

The horizontal turbulent mixing of momentum is determined with a constant eddy-viscosity, while it is ignored for advection of scalars. The Mellor-Yamada level 2.5 (MY2.5) model (Mellor and Yamada 1982), with stability functions modified by Galperin et al. (1988) is used to compute the vertical eddy-viscosity and eddy-diffusivity. Details of the implementation of the turbulence model in SUNTANS are described in Wang et al. (2011a). A comparison of turbulence closure schemes in the Snohomish River estuary shows that differences between the schemes are relatively minor (Wang et al. 2011a).

### 2.2.2 Wet-dry treatment

The wet-dry treatment is developed in SUNTANS by Wang et al. (2008) and is used to simulate the flooding and draining of marshlands in the Bay. The buffering layer with thickness  $h_{\text{buffer}} = 0.1$  m is defined in which the drag coefficient is increased to  $C_d = 5$  in order to decelerate the flow when the water depth becomes very shallow. This is on the same order of magnitude as values used by Ip et al. (1998) ( $h_{\text{buffer}} = 0.25$  m), while Wang et al. (2008) and Zheng and Liu (2003) used  $h_{\text{buffer}} = 0.05$  m. Our choice of  $C_d = 5$  for dry cells follows from values used by Wang et al. (2008). For cells with water depth greater than  $h_{\text{buffer}}$ , the drag coefficient is computed from Eq. 2.8. A minimum depth  $h_{\text{dry}}$  is defined to ensure positive depth for numerical stability. Cells with depth less than  $h_{\text{dry}}$  are considered dry and tagged inactive. Wang et al. (2008) noted that the choice of  $h_{\text{dry}}$  is arbitrary, and we use  $h_{\text{dry}} = 0.05$  m.

### 2.2.3 Numerical method for scalar transport

A variety of scalar transport schemes for unstructured grids are available to interpolate scalar concentrations defined at cell centers of staggered grids to their cell

faces (Darwish and Moukalled 2003; Casulli and Zanolli 2005). Typical implementations of higher-order monotonicity-preserving schemes interpolate face values using a combination of first-order upwinding and a higher-order antidiffusive flux, the value of which is limited using a flux limiter to ensure monotonicity via the TVD (Total Variation Diminishing) constraint (Harten 1983). If the flux limiter is zero, then the scheme reverts to first-order upwinding, while other values of the limiter, which depend solely on the ratio of the upwind to the location scalar concentration gradient, depend on the particular limiter function which is devised to yield different properties. For example, in second-order accurate, five-point TVD schemes for the one-dimensional advection equation, the Superbee limiter (Roe 1984) is the largest possible value of the limiter that still retains monotonicity for one-dimensional advection, while the Minmod limiter (Sweby 1984) is the smallest possible value that ensures TVD and second-order accuracy. The Superbee scheme typically compresses fronts (Fringer and Street 2005; Gross et al. 1999a), while limiters that are closer to the Minmod scheme tend to smooth fronts. When applied to multidimensions on Cartesian grids, operator splitting is required if the TVD properties are to be ensured (Gross et al. 1999a), while on unstructured grids further limitations on the fluxes are required (Casulli and Zanolli 2005).

We implemented the TVD formulation of Casulli and Zanolli (2005) in SUNTANS, which allows specification of any of the existing flux limiters. Rather than presenting a comparison of numerous advection schemes as was done by Gross et al. (1999a) for South Bay, our focus is on the quantitative differences between a low- and a high-order scheme, and therefore we restrict comparison to two schemes, namely one that uses first-order upwind and the second of which employs the Superbee limiter. In the presence of wetting and drying, if a face abuts a dry cell, then first-order upwinding is always employed. This has a negligible effect on the overall character of the advection. In this chapter we refer to the scheme that employs the Superbee limiter as the TVD scheme, and this scheme is employed for the calibration simulations.

## 2.3 Setup of San Francisco Bay simulation

### 2.3.1 Computational domain

The computational domain depicted in Fig. 2.1 spans between the Pacific Ocean and the western and central portions of the Sacramento-San Joaquin Delta, including Central Bay, San Pablo Bay, Suisun Bay and South Bay. The ocean boundary extends to approximately 40 km west of Golden Gate. The radius of the semi-circular ocean boundary is chosen to align the northern most open boundary with Point Reyes. The complex and interconnected network of tributaries in the Sacramento-San Joaquin Delta is represented by a “false delta” consisting of two rectangles (Gross et al. 2005). This allows specification of inflow conditions emerging from the Delta. The length and depth of the “false deltas” are sized to obtain the correct tidal behavior of the Delta as seen by the eastern boundary of the SUNTANS domain.

The major watercourses included in the domain are the Petaluma and Napa rivers which drain into San Pablo Bay and the Suisun and Montezuma slough which feed into Suisun Bay (See Fig. 2.1). The smaller rivers, creeks and tributaries entering San Francisco Bay do not provide significant inflows and are not included in the simulations because they do not significantly affect the salinity results over the 1.5-month simulation period presented in this chapter.

### 2.3.2 Bathymetry

The model uses bathymetric data obtained from the National Geophysical Data Center (NGDC) database. The bathymetry was derived from US National Ocean Service (NOS) soundings in San Francisco Bay and the coastal ocean. The bathymetric source uses raw depths that have not been gridded and the average resolution of the soundings in the Bay is 10 m. Based on the work by Gross et al. (2005), a constant depth of 20 m is assumed for the rectangular “false deltas”. The vertical datum is defined as mean sea level (MSL). We find the resolution of the bathymetry is sufficient for this study as the bathymetric data set used to interpolate the depths to cell centers of the unstructured grid has higher resolution than the resolution of the grid. The



Figure 2.1: The San Francisco Bay model domain, bathymetry (in m) and locations of calibration. Legend: Surface elevations (black circles), currents (red circles), salinity (red squares), and vertical profile transect (black line), Petaluma River (PR), Napa River (NR), Suisun Slough (SS), Montezuma Slough (MS).



bathymetry of San Francisco Bay is shown in Fig. 2.1.

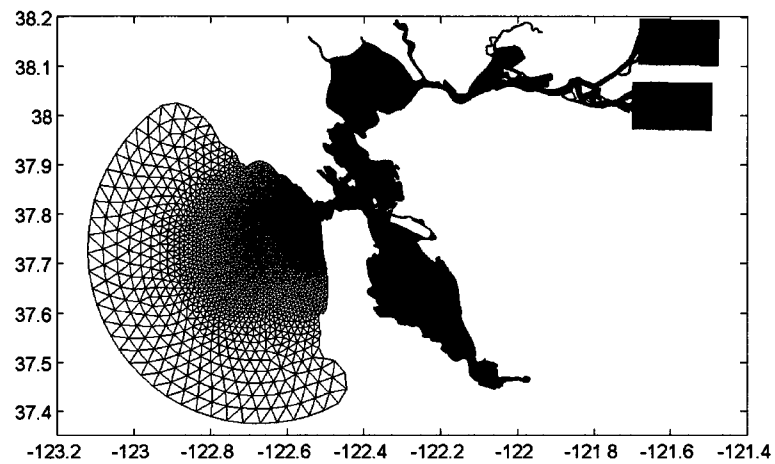
### 2.3.3 Unstructured grid

The unstructured grid for the domain (Fig. 2.2) was generated using SMS (Environmental Modeling Systems, Inc.). The average resolution of the grid, based on triangular cell lengths, is 50 m, and the grid resolution gradually become larger west of the Golden Gate. The gradual transition in grid cell lengths prevents numerical errors associated with abrupt transitions in grid size. SUNTANS uses an orthogonal unstructured mesh, and a metric of orthogonality for San Francisco Bay is shown in Fig. 2.3. Angle skewness is the maximum deviation from  $60^\circ$  among the three angles of a cell, such that the average angle skewness in the Bay is  $8.5^\circ$ .

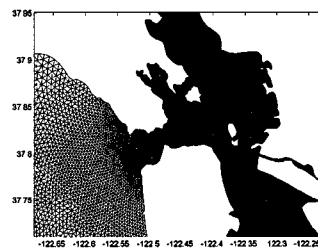
In the vertical, the grid has structured z-levels, with a maximum of 60 layers in the deepest portion of the domain. The minimum vertical resolution is in the top layer and is 0.29 m. The vertical resolution is refined in the upper layers with a stretching ratio of 10% moving downward to resolve the flow in shallow regions of the Bay and in the vicinity of the salt wedge at Carquinez Strait. Partial stepping is employed so that the bottom faces of the bottom-most cells coincide with the interpolated depth at the cell centers. The total number of cells in the horizontal is approximately 80,000 with more than 80% located in the Bay. The three-dimensional grid has approximately 2.5 million grid cells.

### 2.3.4 Initial and boundary conditions

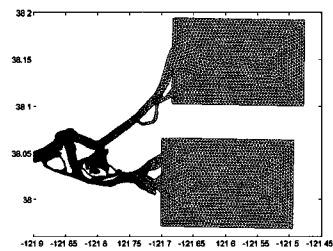
The simulation is initialized with a flat free surface and a quiescent velocity field. The ocean salinity is assumed to be 33.5 psu, which corresponds to typical values observed in the coastal ocean near San Francisco Bay (Dever and Lentz 1994). The salinity field in the Bay was initialized with US Geological Survey (USGS) synoptic observations collected on 11 January 2005. The dataset consists of vertical profiles of salinity at 1 m vertical resolution at 39 sampling locations along the longitudinal axis of San Francisco Bay. The salinity at the cell centers of the grid is obtained by interpolation using the three nearest-neighbors with an inverse-distance weighting



(a) Entire domain



(b) Refinement at Golden Gate



(c) Rectangular "false deltas"

Figure 2.2: The unstructured grid of San Francisco Bay. Entire domain (a), refinement at Golden Gate (b), and rectangular "false deltas" (c).

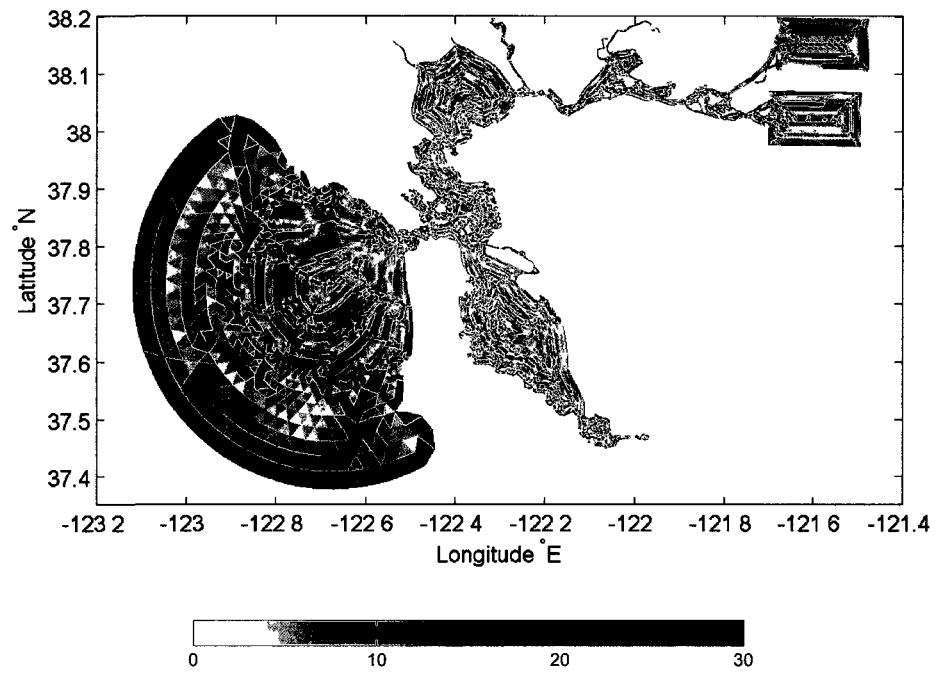


Figure 2.3: Metric of orthogonality for San Francisco Bay. Greyscale depicts the distribution of angle skewness, in degrees.

scheme. Because salinity observations are available in the main channel along the central axis of the Bay but not in the shoals, the initial conditions assume no lateral variation in salinity. By initializing salinity with the observed data, the spin-up time is reduced from approximately 30 days if the domain is initialized with ocean salinity to 15 days.

Open boundaries are located at the Pacific Ocean and at the Sacramento-San Joaquin Delta. The model is tidally forced at all nodes along the Pacific Ocean boundary with the 8 major tidal constituents from observed water surface elevations at Point Reyes (a single point). Specification of amplification and phase lag is not required when using observations at Point Reyes to drive the open ocean boundary, unlike the tidal boundary condition employed by Gross et al. (2005).

The Sacramento-San Joaquin Delta boundary is forced with freshwater inflow estimates from the DAYFLOW program (CDWR 1986). Daily-averaged flows at San Joaquin river past Jersey Point (QWEST) and Sacramento river past Rio Vista (QRIO) are used to force the open boundaries at the rectangular “false deltas”. The DAYFLOW program estimates flow using a volume balance approach, and can contain substantial errors due to uncertain terms in the water balance. Flow monitoring data collected by Oltmann (1998) suggest that the actual daily-averaged flows might be very different from DAYFLOW estimates. The cross-sectionally averaged velocities are imposed by dividing the inflow fluxes by the cross-sectional area at the Delta boundaries. The cross-sectionally averaged velocity is given by

$$u_b = \frac{Q}{A_b}, \quad (2.9)$$

where  $A_b$  is the surface area of the boundary and  $Q$  is the freshwater flow rate estimated from the DAYFLOW program.  $A_b$  is computed for each time step as the surface area changes with the tides.

A 45-day simulation is run during the period 1 Jan 2005 to 14 February 2005. In the winter river inflow is relatively high, and hence the influence of coastal upwelling/downwelling is negligible in our model. The surface elevations, currents and salinity from the 45-day run are compared to observations for the period in which field

data are available. A time step size of 10 s is employed and is dictated by stability of explicit horizontal advection of scalars, which requires, approximately:

$$\Delta t \leq \min \left( \frac{\Delta r_i}{|u_i|} \right), \quad (2.10)$$

the minimum of which occurs where the Voronoi distance between adjacent cells is  $\Delta r_i = 20$  m and the velocity is  $u_i = 2$  m s<sup>-1</sup>, and this occurs at the Golden Gate. Using this time step, simulation of the 45-day period requires 388,800 time steps which consumes 108 h of wallclock time using 32 processors on the Peter A. McCuen Environmental Computing Center at Stanford University. The simulation therefore requires one wallclock second to compute 10 s of simulation time, and thus simulations run roughly ten times faster than real time.

The horizontal eddy-diffusivity is ignored, while the background vertical eddy-diffusivity is set to  $\epsilon_v = 10^{-6}$  m<sup>2</sup> s<sup>-1</sup> which is required to allow turbulence to grow due to production in the turbulence model. The Coriolis parameter is assumed constant and is given by  $f = 9.36 \times 10^{-5}$  rad s<sup>-1</sup>. We neglect winds in our simulations as they do not influence the predictions over the time scale of interest. Winds may be more important for longer time-scale predictions. The implementation of wet-dry treatment in SUNTANS allows for the flooding and draining of the intertidal zones. Fig. 2.4 depicts the exposed areas in North San Francisco Bay during a strong low tide around day 30.9, where areas along the boundary in San Pablo Bay become dry.

## 2.4 Model calibration and validation

### 2.4.1 Surface elevations

Surface elevation calibration was performed via comparison to observations at NOAA stations throughout San Francisco Bay (Fig. 2.1). The predicted and observed surface elevations at four NOAA stations in the Bay (a) Fort Point (9414290), (b) Richmond (9414863), (c) Alameda (9414750), and (d) San Mateo Bridge (9414458) are shown in Fig. 2.5. The diurnal and semi-diurnal tidal ranges and spring-neap tidal cycle are

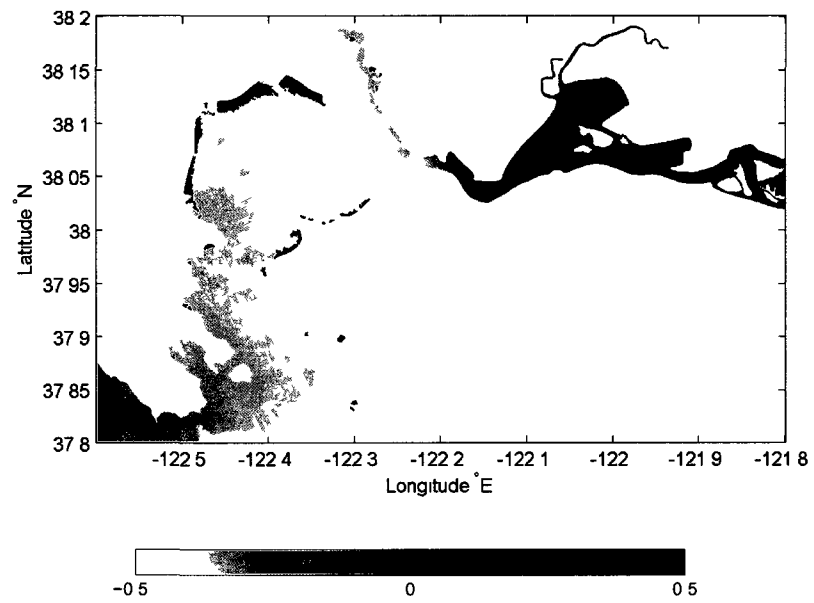


Figure 2.4 Intertidal mudflats in North San Francisco Bay are exposed during LLW (shown in black). Surface elevations (in m) on the wet areas are plotted for day 30.9

Table 2.1: Statistical evaluation of surface elevations

| Station    | RMS error<br>(m) | RMS error<br>(%) | Correlation coefficient |
|------------|------------------|------------------|-------------------------|
| Fort Point | 0.088            | 3.3              | 0.99                    |
| Richmond   | 0.098            | 3.5              | 0.99                    |
| Alameda    | 0.13             | 4.6              | 0.98                    |
| San Mateo  | 0.11             | 3.3              | 0.99                    |

well reproduced by the model at all stations. The predicted and observed surface elevation at Golden Gate show very good agreement, indicating that the ocean boundary condition is accurately specified. The surface elevation at Richmond, Alameda and San Mateo Bridge are also predicted reasonably well both in terms of tidal range and phase. Overall, the surface elevation calibrations demonstrate that the model is accurately propagating tides along the axis of the estuary.

Similar metrics to those of Gross et al. (2009), including mean and RMS errors and the correlation coefficients, are used for model skill assessment. We compute mean and RMS errors of time series with  $N$  elements using:

$$\text{Mean error} = \frac{1}{N} \sum (X_{\text{model}} - X_{\text{obs}}) \quad (2.11)$$

$$\text{RMS error} = \frac{1}{N} \sqrt{\sum (X_{\text{model}} - X_{\text{obs}})^2} \quad (2.12)$$

where  $X$  is the desired quantity to compare, i.e. free-surface, depth-averaged currents, or salinity. The correlation coefficient is computed with:

$$r = \frac{\sum (X_{\text{model}} - \bar{X}_{\text{model}})(X_{\text{obs}} - \bar{X}_{\text{obs}})}{\sqrt{(\sum (X_{\text{model}} - \bar{X}_{\text{model}})^2)(\sum (X_{\text{obs}} - \bar{X}_{\text{obs}})^2)}} \quad (2.13)$$

where  $\bar{X}$  is the quantity time-averaged over the calibration period. Statistical evaluation of the model performance for surface elevations is presented in Table 2.1. At the NOAA stations, the RMS errors are less than 5% of the tidal range and correlation coefficients exceed 0.98.

Harmonic analysis of surface elevations is carried out at NOAA stations where harmonic constituent data are available. A comparison of observed and predicted

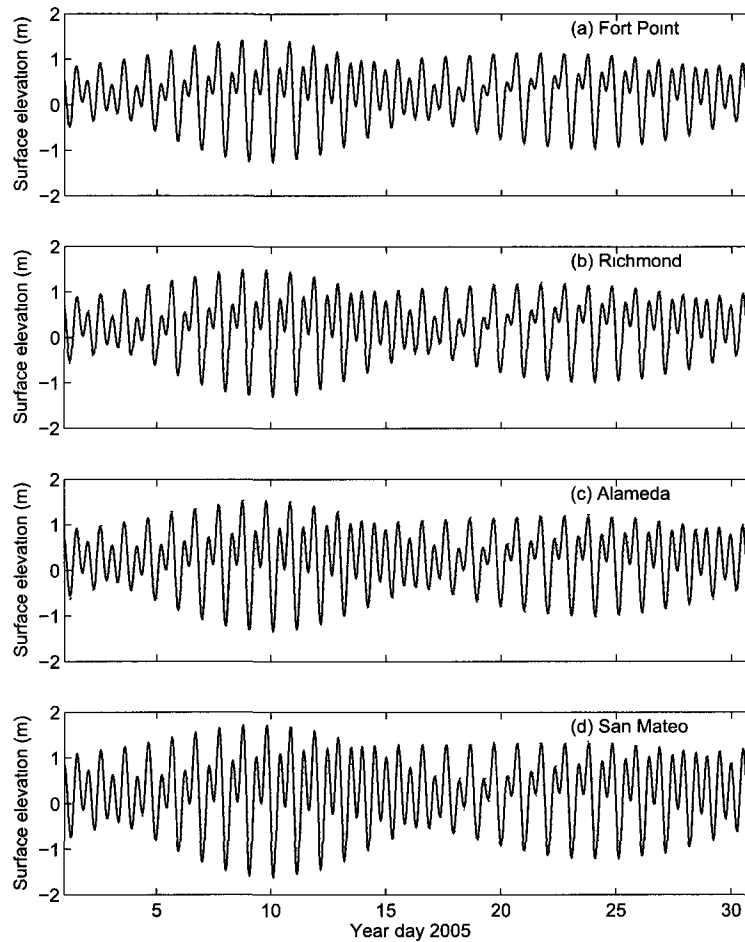


Figure 2.5: Comparison of predicted and observed surface elevations (in m) at (a) Fort Point (b) Richmond (c) Alameda and (d) San Mateo Bridge. Legend: predictions ( $\cdots$ ), observations ( $—$ )



Table 2.2: M2 surface elevation constituents

| Station            | Amplitude (m) |           |        | Phase (°) |           |       |
|--------------------|---------------|-----------|--------|-----------|-----------|-------|
|                    | Observed      | Predicted | Error  | Observed  | Predicted | Error |
| <b>Central Bay</b> |               |           |        |           |           |       |
| Fort Point         | 0.580         | 0.586     | -0.006 | 210.6     | 211.0     | -0.4  |
| Richmond           | 0.616         | 0.612     | 0.004  | 223.1     | 231.2     | -8.1  |
| <b>South Bay</b>   |               |           |        |           |           |       |
| North Point        | 0.607         | 0.624     | -0.017 | 213.3     | 221.1     | -7.8  |
| Pier 22 1/2        | 0.644         | 0.658     | -0.014 | 218.9     | 226.4     | -7.5  |
| Alameda            | 0.678         | 0.709     | -0.031 | 224.0     | 229.5     | -5.5  |
| Hunters Point      | 0.706         | 0.720     | -0.014 | 223.6     | 228.4     | -4.8  |
| Oyster Point       | 0.753         | 0.762     | -0.009 | 235.5     | 230.0     | 5.5   |
| San Mateo          | 0.826         | 0.814     | 0.012  | 238.0     | 231.9     | 6.1   |
| <b>North Bay</b>   |               |           |        |           |           |       |
| Mare Island        | 0.597         | 0.659     | -0.062 | 260.6     | 254.6     | 6.0   |
| Port Chicago       | 0.515         | 0.424     | 0.091  | 288.2     | 277.5     | 10.7  |

amplitudes and phases for the M2 constituent is shown in Table 2.2. The amplitude and phase errors are within 9 cm and 11°, respectively for all stations. The observed and predicted K1 harmonics are shown in Table 2.3. The errors for amplitudes and phases are within 9 cm and 10°, respectively. The effect of errors of S1, O1 and N2 harmonics on the tidal hydrodynamics are negligible as their amplitudes on the order of 0.1, 0.2 and 0.1 m respectively, are relatively small when compared to the M2 and K1 harmonics which are on the order of 0.6 m and 0.3 m, respectively (Table 2.4 - 2.6). The spatial distributions of the amplitude and phases for the M2 and K1 harmonics are plotted in Fig. 2.6, which shows that the errors in the predicted M2 and K1 amplitudes increase with distance from the Golden Gate. This occurs primarily because of the false delta which reflects too much of the barotropic tidal energy. Additionally, bathymetric variability upstream makes accurate specification of bottom roughness a difficult task, particularly where the shallow mudflats are extensive.

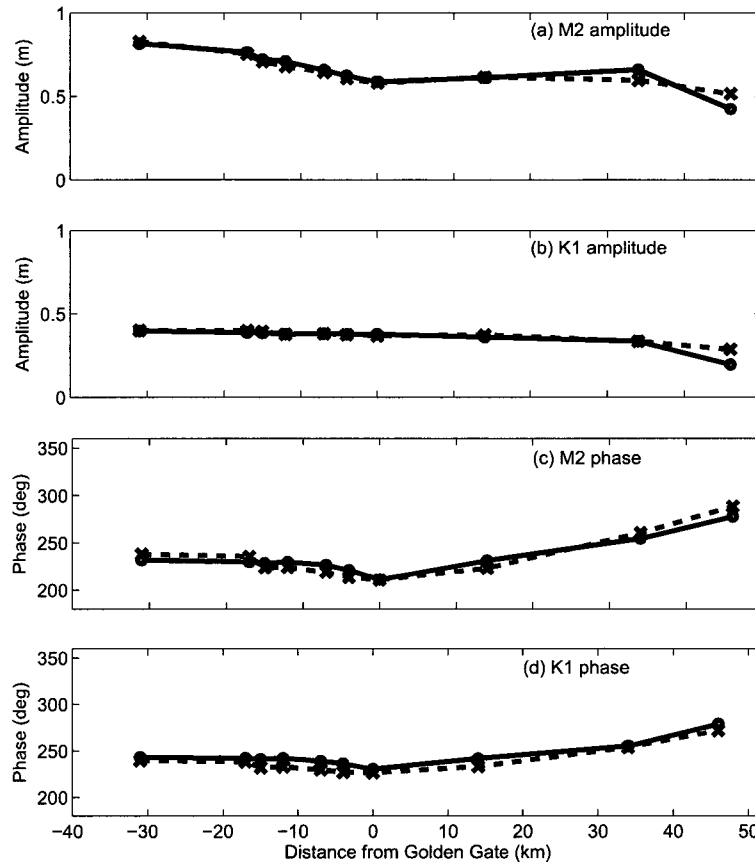


Figure 2.6: Distribution of amplitudes (in m) and phases (in degrees) for M2 and K1 harmonics plotted against distance from Golden Gate. Points in South Bay are negative and those in North Bay are positive. Legend: predictions (—o—), observations (—x—).

Table 2.3: K1 surface elevation constituents

| Station            | Amplitude (m) |           |        | Phase (°) |           |       |
|--------------------|---------------|-----------|--------|-----------|-----------|-------|
|                    | Observed      | Predicted | Error  | Observed  | Predicted | Error |
| <b>Central Bay</b> |               |           |        |           |           |       |
| Fort Point         | 0.368         | 0.378     | -0.010 | 226.5     | 230.2     | -3.7  |
| Richmond           | 0.374         | 0.360     | 0.014  | 233.1     | 241.5     | -8.4  |
| <b>South Bay</b>   |               |           |        |           |           |       |
| North Point        | 0.376         | 0.377     | -0.001 | 226.8     | 236.2     | -9.4  |
| Pier 22 1/2        | 0.381         | 0.381     | 0.000  | 229.5     | 239.0     | -9.5  |
| Alameda            | 0.377         | 0.377     | 0.000  | 232.7     | 241.8     | -9.1  |
| Hunters Point      | 0.394         | 0.385     | 0.009  | 232.1     | 240.8     | -8.7  |
| Oyster Point       | 0.400         | 0.388     | 0.012  | 238.3     | 242.0     | -3.7  |
| San Mateo          | 0.401         | 0.396     | 0.005  | 239.5     | 243.0     | -3.5  |
| <b>North Bay</b>   |               |           |        |           |           |       |
| Mare Island        | 0.336         | 0.336     | 0.000  | 253.7     | 255.2     | -1.5  |
| Port Chicago       | 0.287         | 0.196     | 0.091  | 271.9     | 278.8     | -6.9  |

Table 2.4: S1 surface elevation constituents

| Station            | Amplitude (m) |           |       | Phase (deg) |           |       |
|--------------------|---------------|-----------|-------|-------------|-----------|-------|
|                    | Observed      | Predicted | Error | Observed    | Predicted | Error |
| <b>Central Bay</b> |               |           |       |             |           |       |
| Fort Point         | 0.137         | 0.087     | 0.050 | 218.4       | 214.9     | 3.5   |
| Richmond           | 0.143         | 0.087     | 0.056 | 233.6       | 241.9     | -8.3  |
| <b>South Bay</b>   |               |           |       |             |           |       |
| North Point        | 0.141         | 0.088     | 0.053 | 220.7       | 233.3     | -12.6 |
| Pier 22 1/2        | 0.143         | 0.094     | 0.049 | 227.2       | 241.3     | -14.1 |
| Alameda            | 0.154         | 0.104     | 0.050 | 235.0       | 245.1     | -10.1 |
| Hunters Point      | 0.163         | 0.106     | 0.057 | 236.5       | 244.7     | -8.2  |
| Oyster Point       | 0.166         | 0.114     | 0.052 | 246.6       | 247.1     | -0.5  |
| San Mateo          | 0.182         | 0.123     | 0.059 | 253.3       | 249.8     | 3.5   |
| <b>North Bay</b>   |               |           |       |             |           |       |
| Mare Island        | 0.129         | 0.092     | 0.037 | 273.5       | 272.0     | 1.5   |
| Port Chicago       | 0.106         | 0.049     | 0.057 | 302.4       | 306.7     | -4.3  |

Table 2.5: O1 surface elevation constituents

| Station            | Amplitude (m) |           |        | Phase (deg) |           |       |
|--------------------|---------------|-----------|--------|-------------|-----------|-------|
|                    | Observed      | Predicted | Error  | Observed    | Predicted | Error |
| <b>Central Bay</b> |               |           |        |             |           |       |
| Fort Point         | 0.230         | 0.250     | -0.020 | 210.1       | 213.3     | -3.2  |
| Richmond           | 0.228         | 0.231     | -0.003 | 216.9       | 226.1     | -9.2  |
| <b>South Bay</b>   |               |           |        |             |           |       |
| North Point        | 0.231         | 0.248     | -0.017 | 209.7       | 219.7     | -10.0 |
| Pier 22 1/2        | 0.231         | 0.250     | -0.019 | 212.8       | 222.7     | -9.9  |
| Alameda            | 0.230         | 0.243     | -0.013 | 216.5       | 226.7     | -10.2 |
| Hunters Point      | 0.234         | 0.250     | -0.016 | 214.8       | 225.1     | -10.3 |
| Oyster Point       | 0.240         | 0.251     | -0.011 | 221.7       | 226.7     | -5.0  |
| San Mateo          | 0.241         | 0.256     | -0.015 | 223.9       | 227.6     | -3.7  |
| <b>North Bay</b>   |               |           |        |             |           |       |
| Mare Island        | 0.200         | 0.212     | -0.012 | 237.2       | 240.4     | -3.2  |
| Port Chicago       | 0.164         | 0.117     | 0.047  | 256.4       | 269.3     | -12.9 |

Table 2.6: N2 surface elevation constituents

| Station            | Amplitude (m) |           |        | Phase (deg) |           |       |
|--------------------|---------------|-----------|--------|-------------|-----------|-------|
|                    | Observed      | Predicted | Error  | Observed    | Predicted | Error |
| <b>Central Bay</b> |               |           |        |             |           |       |
| Fort Point         | 0.123         | 0.114     | 0.009  | 184.9       | 187.6     | -2.7  |
| Richmond           | 0.130         | 0.115     | 0.015  | 197.1       | 209.0     | -11.9 |
| <b>South Bay</b>   |               |           |        |             |           |       |
| North Point        | 0.129         | 0.119     | 0.010  | 187.0       | 199.9     | -12.9 |
| Pier 22 1/2        | 0.133         | 0.125     | 0.008  | 193.5       | 206.0     | -12.5 |
| Alameda            | 0.139         | 0.134     | 0.005  | 199.3       | 209.5     | -10.2 |
| Hunters Point      | 0.147         | 0.136     | 0.011  | 199.5       | 208.5     | -9.0  |
| Oyster Point       | 0.156         | 0.144     | 0.012  | 213.4       | 210.4     | 3.0   |
| San Mateo          | 0.166         | 0.153     | 0.013  | 216.0       | 212.5     | 3.5   |
| <b>North Bay</b>   |               |           |        |             |           |       |
| Mare Island        | 0.119         | 0.122     | -0.003 | 233.8       | 233.4     | 0.4   |
| Port Chicago       | 0.098         | 0.076     | 0.022  | 262.1       | 258.1     | 4.0   |

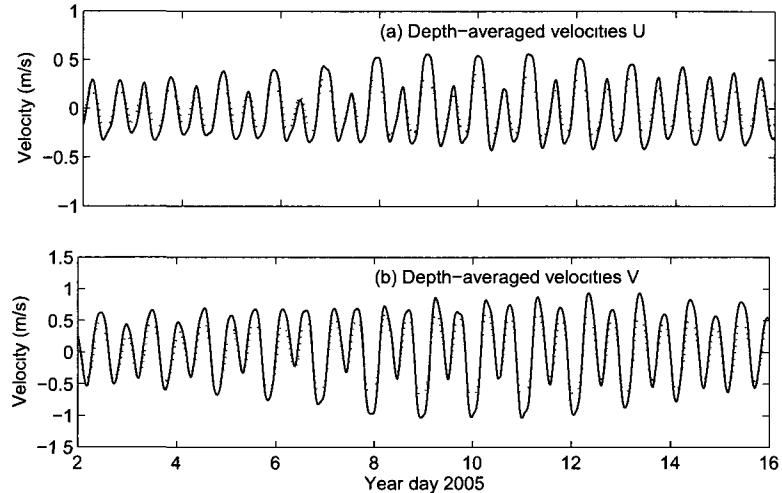


Figure 2.7: Comparison of predicted and observed depth-averaged velocities ( $\text{m s}^{-1}$ ) at Richmond. Legend: predictions ( $\cdots$ ), observations ( $\text{—}$ ).

### 2.4.2 Currents

Acoustic doppler profiler (ADP) current data are obtained from NOAA/NOS at two stations in San Francisco Bay, namely: (a) Richmond and (b) Oakland. Current data is available at the ADP stations from 1 January 2005 (year day 1) - 30 January 2005 (year day 30). The locations of the ADP stations are shown in Fig. 2.1. The raw ADP current data is filtered with a low-pass fifth-order Butterworth filter, with the cutoff frequency of seven cycles/day to remove the high-frequency non-tidal oscillations, following the approach of Sankaranarayanan and McCay (2003). The phase shift inherent to the Butterworth filter is eliminated by passing the current data forward and backward through the filter. The U and V directions are chosen as the east and north components of the velocities, respectively. A statistical evaluation of the model performance for the depth-averaged U and V velocities is presented in Table 2.7. The mean and RMS errors are computed with Eqs. 2.11 and 2.12 where  $X$  is either the depth-averaged U or V velocity.

As shown in Figs. 2.7 and 2.8, the model reproduces the spring-neap variability and the mixed diurnal and semi-diurnal variability in the observed currents at Richmond. The depth-averaged velocities in Fig. 2.7 show the phases of the U and V velocities

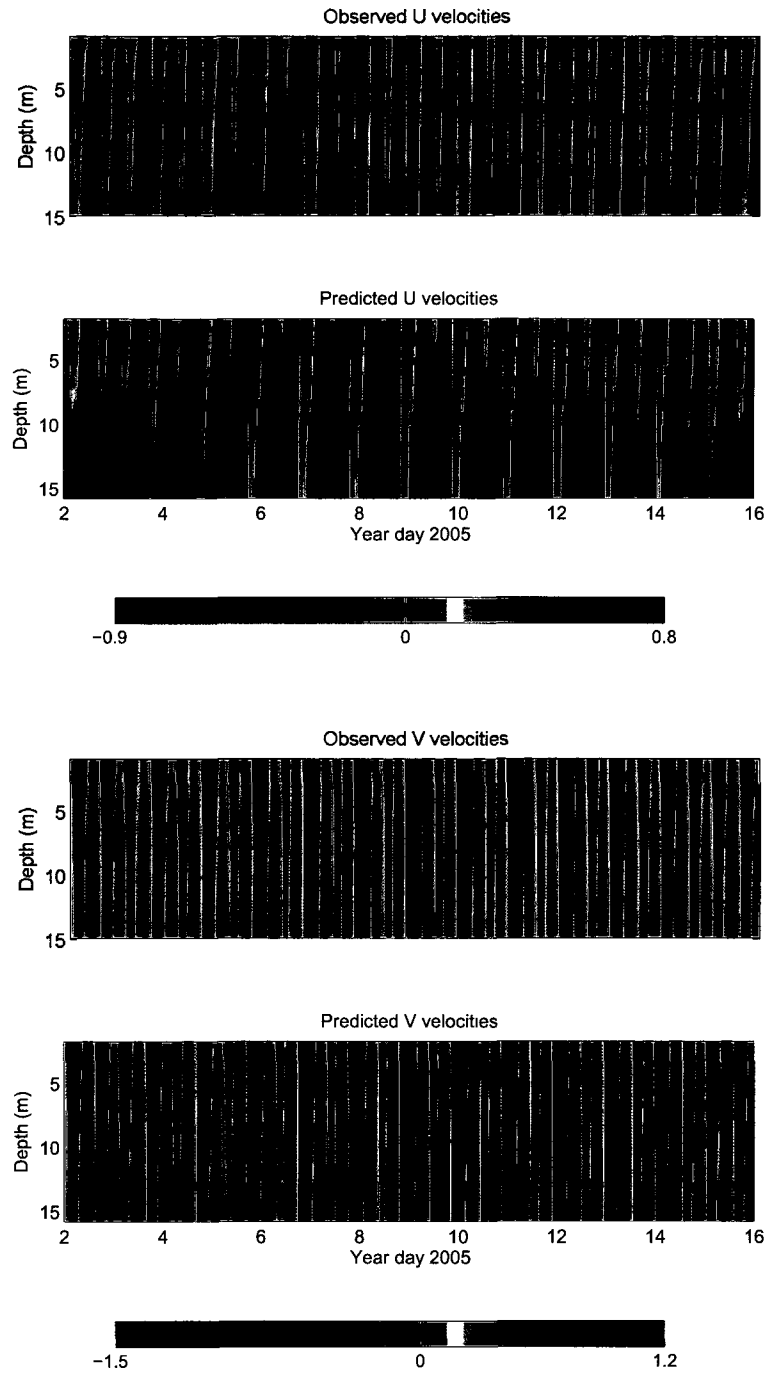


Figure 2.8: Comparison of predicted and observed U and V velocity profiles (in  $\text{m s}^{-1}$ ) at Richmond.

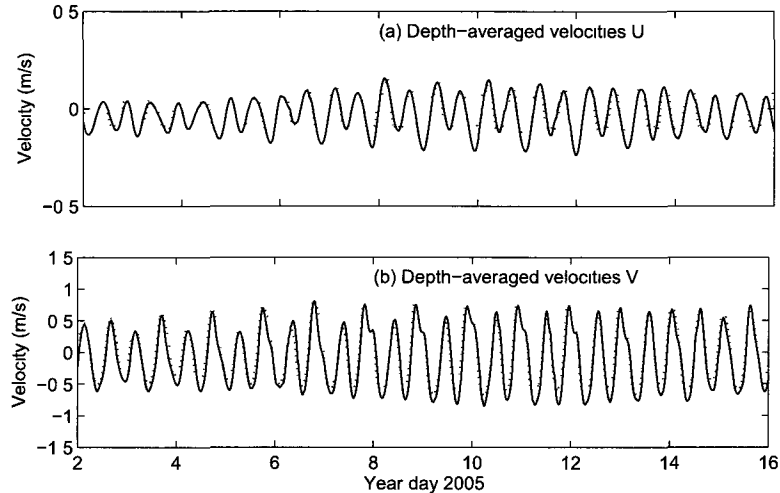


Figure 2.9: Comparison of predicted and observed depth-averaged velocities ( $\text{m s}^{-1}$ ) at Oakland. Legend: predictions ( $\cdots$ ), observations ( $\text{—}$ ).

compare well, and overall a good level of agreement is obtained for the magnitudes. Peak U and V depth-averaged velocities are slightly underpredicted by the model. U and V velocity profiles in Fig. 2.8 compare well throughout the water column. U velocity profiles close to the bottom are slightly underpredicted during flood and ebb. We attribute these errors to two sources. First, the Richmond ADP is located close to the intertidal mudflats and hence the flow at Richmond is influenced by the wetting and drying process of the mudflats, which is subject to numerical errors as a result of strong gradients inherent in the observations that may not be resolved by the simulations. Second, the accuracy of predicting velocities in the bottom half of the water column is dependent on accurate representation of the bottom shear layer which is difficult to capture correctly in the presence of strong bathymetric variability.

As shown in Figs. 2.9 and 2.10, at Oakland the model-predicted currents have similar spring-neap cycles and mixed diurnal and semi-diurnal patterns as the observed velocities. The phases and magnitudes of the U and V depth-averaged velocities show good overall agreement. The depth-averaged velocities in Fig. 2.9 show that the peak ebb U velocities are underpredicted by the model during spring tides, while peak flood U velocities are overpredicted by the model during neap tides. During spring

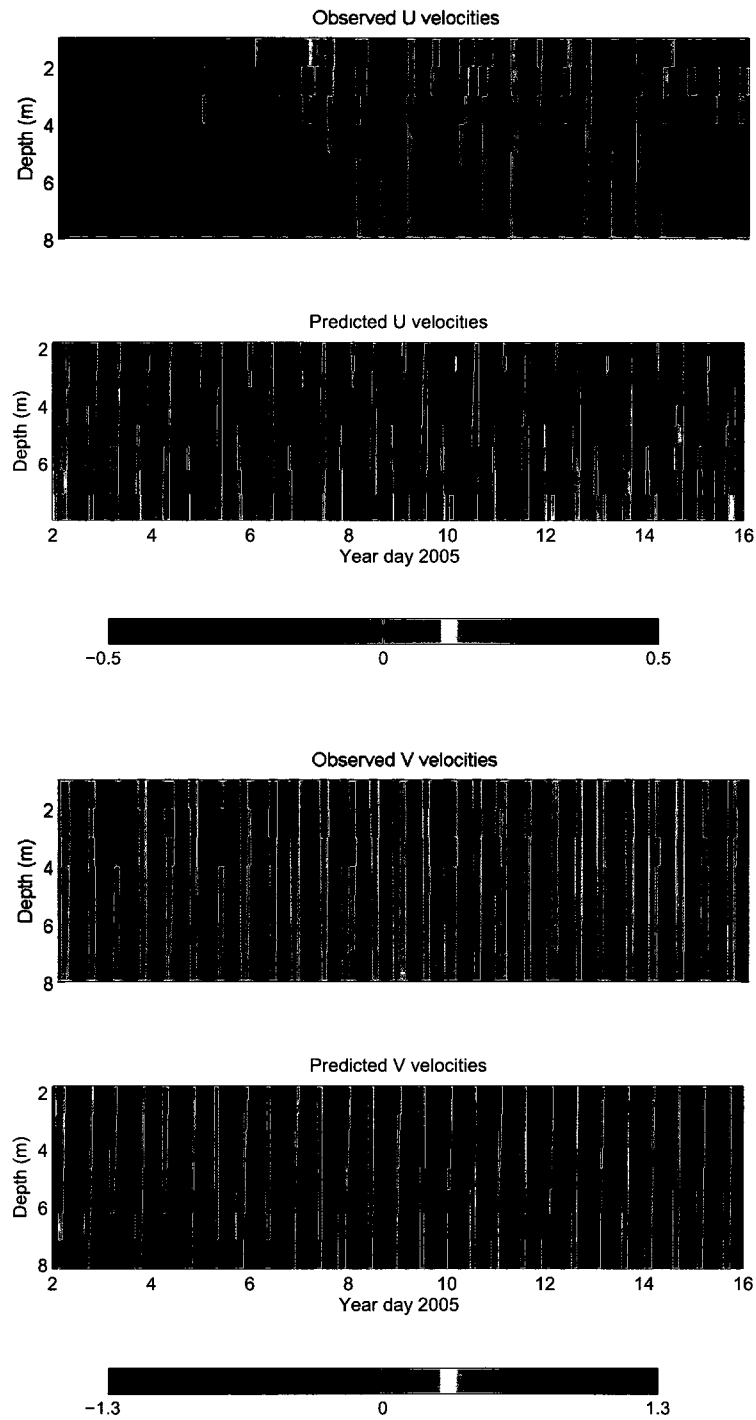


Figure 2.10: Comparison of predicted and observed U and V velocity profiles (in  $\text{m s}^{-1}$ ) at Oakland.



Table 2.7: Statistical evaluation of depth-averaged velocities

| Station         | Observed mean<br>(m s <sup>-1</sup> ) | Predicted mean<br>(m s <sup>-1</sup> ) | Mean error<br>(m s <sup>-1</sup> ) | RMS error<br>(m s <sup>-1</sup> ) |
|-----------------|---------------------------------------|--|------------------------------------|-----------------------------------|
| <b>Richmond</b> |                                       |  |                                    |                                   |
| U               | -0.0093                               | -0.0022                                | 0.0071                             | 0.11                              |
| V               | 0.057                                 | -0.0044                                | 0.061                              | 0.16                              |
| <b>Oakland</b>  |                                       |  |                                    |                                   |
| U               | -0.030                                | -0.0040                                | 0.026                              | 0.065                             |
| V               | -0.074                                | 0.017                                  | 0.096                              | 0.17                              |

tides peak flood V velocities are overpredicted by the model, and peak ebb V velocities are underpredicted by the model. V velocity profiles in Fig. 2.10 compare well throughout the water column, while U velocity profiles close to the surface during ebb are underpredicted by our model and U velocity profiles close to the bottom during flood are overpredicted by our model. The difficulty in obtaining good predictions at Oakland is due to the complex flow around Treasure Island and Yerba Buena Island which is highly variable, and may not be well-resolved by the resolution in our model.

### 2.4.3 Salinity

The salinity calibration is performed from 15 January 2005 (year day 15) to 15 February 2005 (year day 45). We calibrated salinity for this period as it takes at least 15 days to spin-up the three-dimensional salinity simulations. The salinity predictions are compared with observations from the US Geological Survey (USGS) at two locations in San Francisco Bay, namely (a) Point San Pablo (PSP) and (b) Benicia (BEN) (shown in Fig. 2.1). The salinity observations consist of both near-surface and near-bottom salinity at both stations. The observed salinity data is filtered with a low-pass fifth-order ButterWorth filter to remove non-tidal oscillations, and forward and backward passed to eliminate the phase shift inherent in the filter.

Time series of surface and bottom salinity, and bottom-top salinity difference at Point San Pablo are shown in Fig. 2.11. In general, there is good qualitative agreement between the predicted and observed salinities in terms of amplitude and phase. The predicted stratification compares well with observations, with the exception that our

model predicts lower maximum stratification (3 psu) from year day 48 to year day 50, as a consequence of overprediction of minimum surface salinity during this period.

Time series of surface and bottom salinity, and bottom-top salinity difference at Benicia are shown in Fig. 2.12. The salinity predictions are generally in good agreement with the observations. The predicted onset and breakdown of stratification occurs roughly with the correct magnitude and phase relative to the observations. Periodically stratified conditions are present during spring tides, in which the water column is well-mixed during the strong tide and weakly stratified during the weak tide. The minimum stratification from our model is relatively insensitive to the spring-neap variability. The errors may be due to inaccuracies in the inflow estimates from DAYFLOW, the effects of which are larger when the strength of the tidal currents is weak. Flow boundary conditions imposed at the Delta use daily-averaged flow values, and this averaging may also contribute to the errors.

Statistical evaluation of the model performance for salinity is presented in Table 2.8. The mean and RMS errors are computed with Eqs. 2.11 and 2.12. The mean errors at PSP at the surface and bottom sensors are 0.14 psu and 0.25 psu, respectively, while the RMS errors at the surface and bottom sensors are 1.4 psu and 1.2 psu, respectively. Our mean errors are lower than those of Gross et al. (2009), in which the mean errors for the surface and bottom sensors are 1.0 psu and 0.8 psu, respectively (Gross et al. (2009) did not compute RMS errors for salinity). MacWilliams et al. (2007) compared bottom salinities at this station, and found mean and RMS errors of 1.22 psu and 1.70 psu, respectively.

The mean errors at Benicia at the surface and bottom sensors are 0.08 psu and 0.36 psu respectively, while the RMS errors at the surface and bottom sensors are 1.2 psu and 1.4 psu, respectively. At a nearby location (Martinez in Carquinez Strait) Gross et al. (2009) found mean errors for the surface and bottom sensors of 0.5 psu and 1.4 psu, respectively (Gross did not compute RMS errors for salinity). MacWilliams et al. (2007) computed the mean and RMS errors at the bottom sensors to be 1.56 psu and 2.21 psu, respectively. Overall, our model therefore has errors that are lower than the three-dimensional simulations of San Francisco Bay performed with TRIM (Gross et al. 2009) and UnTRIM (MacWilliams et al. 2007).

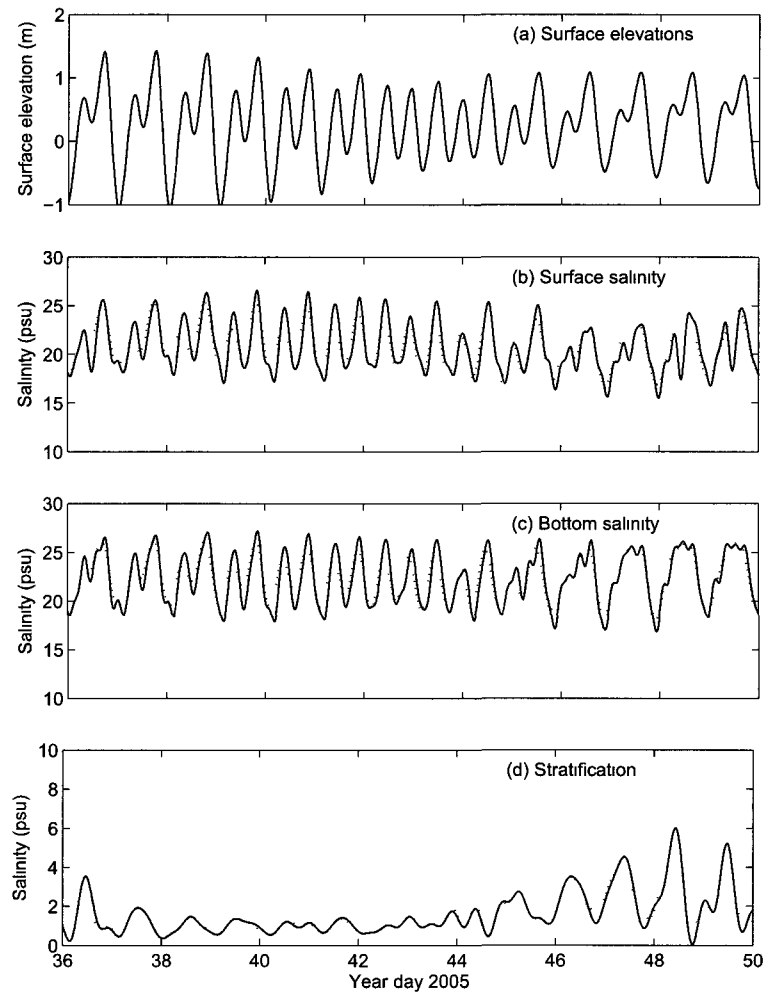


Figure 2.11: Comparison of predicted and observed salinities (in psu) at Point San Pablo (a) surface elevations (b) surface salinity (c) bottom salinity (d) stratification. Surface and bottom salinities are 7.9 m and 0.9 m from the bottom, respectively. Legend: predictions ( $\cdots$ ), observations ( $---$ ).

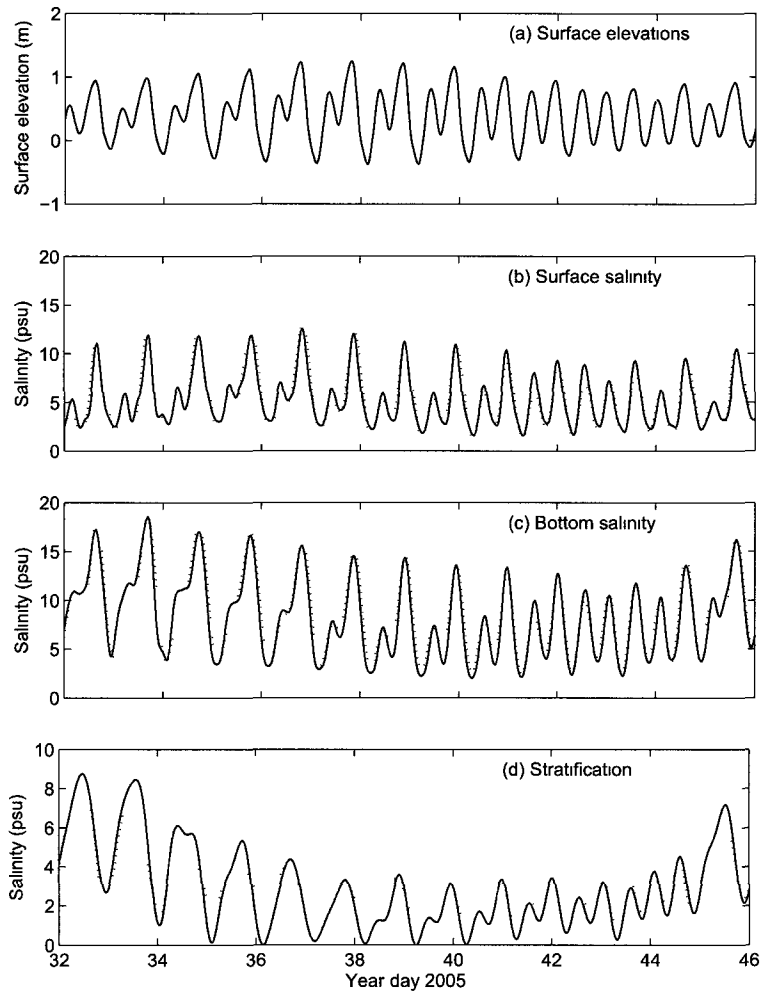


Figure 2.12: Comparison of predicted and observed salinities (in psu) at Benicia (a) surface elevations (b) surface salinity (c) bottom salinity (d) stratification. Surface and bottom salinities are 22.5 m and 7.6 m from the bottom, respectively. Legend: predictions ( $\cdots$ ), observations ( $-$ ).

Table 2.8: Statistical evaluation of salinity.

| Station                      | Observed mean<br>(psu) | Predicted mean<br>(psu) | Mean error<br>(psu) | RMS error<br>(psu) |
|------------------------------|------------------------|-------------------------|---------------------|--------------------|
| <b>Point San Pablo (PSP)</b> |                        |                         |                     |                    |
| Surface                      | 20.7                   | 20.9                    | 0.14                | 1.4                |
| Bottom                       | 22.3                   | 22.6                    | 0.25                | 1.2                |
| <b>Benicia Bridge (BEN)</b>  |                        |                         |                     |                    |
| Surface                      | 5.3                    | 5.4                     | 0.08                | 1.2                |
| Bottom                       | 8.2                    | 8.6                     | 0.36                | 1.4                |

## 2.5 Summary

The unstructured-grid SUNTANS model applied to San Francisco Bay is employed to perform three-dimensional simulations of flow. Scalar transport is accomplished with a TVD formulation modified to work in the presence of wetting and drying. The model inputs include high resolution bathymetry from the NGDC database and an unstructured grid with an average resolution of 50 m. The model is forced at the open ocean boundary with water surface elevations and at the Delta boundary with freshwater inflows. The calibration is performed for a 45-day period with a time step size of 10 s, so that the simulations run roughly ten times faster than real time.

The model is calibrated by adjusting the bottom roughness to reproduce sea-surface heights, currents and salinity at locations throughout the Bay. Comparisons of predicted surface elevations and depth-averaged currents with observations match well at most locations in the Bay. The spring and neap tidal cycles and the mixed semi-diurnal and diurnal tidal ranges for surface elevations and currents are reproduced by the model. However, large errors are observed in surface elevations predictions at the upstream locations at Mare Island and Port Chicago. These errors arise likely due to the false delta approximation which does not absorb enough barotropic tidal energy. As the focus of our work is on salinity simulations at the location of the salt wedge in Carquinez Strait, these errors have little effect on the results presented in this chapter and throughout this dissertation.

Small errors in amplitudes and phases for the depth-averaged currents are observed at the Richmond and Oakland ADP, and comparisons of predicted velocity profiles

with observations do not match as well. The errors are likely attributed to inadequate resolution and to numerical diffusion when employing first-order interpolation in the ELM scheme. These errors could be reduced by employing quadratic interpolation (Wang et al. 2011b). The salinity predictions are in good qualitative agreement with observations in terms of amplitude and phase. The salinity predictions also capture the periodic stratification of the estuary, validating the inputs and choice of parameterizations.

# Chapter 3

## Sensitivity analysis of salinity simulations

### 3.1 Introduction

In this chapter, we perform a sensitivity study to understand the effects of grid resolution, the turbulence model, and the scalar transport scheme on salinity simulations. Three levels of grid refinement are employed, and the results of a second-order accurate, TVD scalar transport scheme are compared to those with first-order upwinding. The relative contributions of numerical diffusion associated with the advection scheme and physical diffusion resulting from vertical eddy-diffusivity in the turbulence model on salinity intrusion and stratification are also presented. This chapter is also taken from Chua and Fringer (2011).

### 3.2 Sensitivity to grid resolution

To understand model sensitivity with respect to grid resolution, we perform simulations with three different levels of horizontal grid refinement. The coarse mesh has grid cell edge lengths of 200 m in the Bay, the medium mesh has grid cell edge lengths of 100 m in the Bay and the fine mesh has grid cell edge lengths of 50 m in the Bay. The fine mesh results correspond to those presented in Chapter 2. For all

three meshes, the grid resolution gradually becomes larger west of the Golden Gate. The vertical structured z-level grid is not changed. Comparisons of salinity predictions with observations are made at Benicia with the three levels of grid resolution. We perform the simulations on each mesh with four different scenarios to evaluate the relative effects of the scalar transport scheme and the turbulence model. The scenarios are referred to as: (A) TVD with turbulence model (B) TVD without turbulence model (C) First-order upwind with turbulence model (D) First-order upwind without turbulence model. When the turbulence model is not employed, this implies that we ignore vertical eddy-diffusivity in the scalar transport equation by setting it to zero, although vertical eddy-viscosity is still retained in the momentum equations. All other parameters are the same as those presented in Chap. 2.

The mean and RMS errors in the bottom salinity at Benicia and Point San Pablo are plotted as a function of grid refinement in Fig. 3.1. The most obvious source of error in the plots is the monotonic increase in errors moving from scenario A to D for a fixed grid resolution (A possessing the smallest error and D possessing the largest error). The largest increase in error occurs from implementation of first-order upwind for scalar advection, which is apparent in both the mean and RMS errors. The second greatest source of error results from implementation of the turbulence model. Lack of the turbulence model, and hence lack of vertical eddy-diffusivity, leads to a greater error for all levels of grid refinement. The impact of the turbulence model is relatively weak for all cases except for its impact on the mean salinity error when the TVD scheme is employed (runs A and B). Although the impact of not using the turbulence model on the mean salinity is large for these cases, the mean error in the bottom salinity is the same without the turbulence model on the fine grid as that with the turbulence model on the coarse grid.

Fig. 3.1 shows that convergence with respect to grid refinement is achieved with the TVD advection scheme (runs A and B), but convergence is extremely weak for the first-order scheme (runs C and D). This is shown with the least squares fitted convergence rates tabulated in Table 3.1. For runs A and B, convergence is near 1.5-order with respect to grid refinement for the mean error. However, convergence is



weaker for the RMS error. Although second-order convergence is expected for the one-dimensional five-point TVD schemes (Roe 1984), errors arising from implementation on the unstructured grid reduce the rate of convergence to less than second order.

The depth-averaged salinity at a particular location within the salt wedge can be approximated by assuming that it lies in a region of relatively constant horizontal salinity gradient  $\Gamma$  (Monismith et al. 2002), such that

$$s(t) = S - \frac{u\Gamma}{\omega} \sin(\omega t), \quad (3.1)$$

where  $S$  is the time- and depth-averaged salinity, and  $u$  is magnitude of the depth-averaged tidal currents at frequency  $\omega$ . If we denote an observed value with subscript  $o$  and a modeled or predicted value with subscript  $p$ , then the error in the salinity can be approximated by

$$\Delta s(t) = s_p(t) - s_o(t) = \Delta S - \frac{u\Delta\Gamma}{\omega} \sin(\omega t),$$

where  $\Delta S = S_p - S_o$  and  $\Delta\Gamma = \Gamma_p - \Gamma_o$ , and we have assumed that most of the error arises from differences in the modeled salinity field and not in the depth-averaged currents  $u$ . Denoting the time-average over a period  $2\pi/\omega$  with an overbar gives the time-average of the error as

$$\overline{\Delta s(t)} = \Delta S,$$

and the RMS error as

$$\begin{aligned} \left( \overline{(\Delta s - \overline{\Delta s})^2} \right)^{1/2} &= \left( \overline{\Delta s^2} - (\overline{\Delta s})^2 \right)^{1/2}, \\ &= \frac{1}{\sqrt{2}} \frac{u\Delta\Gamma}{\omega}. \end{aligned}$$

This shows that the mean error indicates errors in the time- and depth-averaged salinity at a point, while the RMS error depends more strongly on errors in the horizontal salinity gradient, i.e.,  $\Delta\Gamma$ .

Hence, the mean error is a measure of model ability to produce the correct salinity intrusion, and the RMS error is a measure of model ability to reproduce horizontal

Table 3.1: Least squares fitted convergence rates for runs A – D

| Runs | Benicia |       | Point San Pablo |       |
|------|---------|-------|-----------------|-------|
|      | Mean    | RMS   | Mean            | RMS   |
| A    | 1.3     | 0.38  | 1.4             | 0.45  |
| B    | 0.90    | 0.31  | 1.0             | 0.38  |
| C    | 0.13    | 0.076 | 0.16            | 0.076 |
| D    | 0.037   | 0.033 | 0.043           | 0.065 |

salinity gradients. This implies that model ability to predict salinity values converges at near 1.5-order, while model ability to predict salinity gradients converges with less than first order. Since both Benicia and Point San Pablo lie within the salt wedge, the errors at the two locations behave similarly. However, convergence rates at Point San Pablo are slightly higher, and this may be due to smoother bathymetry and weaker currents there.

Despite an expected first-order convergence rate, Fig. 3.1 shows that use of the first-order upwinding scheme (runs C and D) exhibits lack of convergence for the grid resolutions employed. The relative impact of the turbulence model on the errors is also negligible when first-order upwinding is employed. We hypothesize that lack of convergence occurs because excessive numerical diffusion due to first-order upwinding eliminates the feedback mechanism between vertical turbulent mixing and stratification. This is exhibited by the ineffectiveness of the turbulence model in reducing the errors for first-order upwinding in Fig. 3.1. On the other hand, when the TVD scheme is employed, the nonlinear feedback causes a reduction in errors by roughly one order of magnitude (the difference between run A and run B).

As shown in Fig. 3.2, the impact of first-order upwinding is not only to reduce the horizontal salinity gradient, but also to reduce the vertical stratification. The reduction of the stratification occurs because the reduced horizontal salinity gradient reduces the gravitational circulation which acts to decrease the stratification. Monismith et al. (2002) and Geyer and Chant (2006) show that, to leading order, friction balances the baroclinic pressure gradient caused by the longitudinal salinity gradient, from which they demonstrate that the magnitude of the estuarine circulation

depends on the horizontal salinity gradient. As shown by the depth-averaged longitudinal salinity profiles in Fig. 3.3, the stronger vertical stratification resulting from the TVD scheme leads to nonlinear feedback between vertical mixing and stratification. The nonlinear feedback reduces the vertical mixing, which leads to more salinity intrusion for run A over run C. Figure 3.4 depicts the vertical eddy-diffusivity over time at Benicia and shows that indeed the vertical eddy-diffusivity is substantially lower when the TVD scheme is employed.

Overlaid on the results in Fig. 3.1 are the errors computed by MacWilliams et al. (2007) and Gross et al. (2009). MacWilliams et al. (2007) employed the UnTRIM model using an unstructured grid with a nominal resolution of 400 m in the Bay, while Gross et al. (2009) used the Cartesian-grid TRIM model with a fixed horizontal resolution of 200 m. Although those simulations were calibrated over much longer periods than the present simulations, it is still useful to compare their results to ours in the context of understanding the impact of grid resolution. UnTRIM and TRIM employ the same TVD scheme as in SUNTANS (which is based on the method of Casulli and Zanolli (2005)). While the turbulence models are different, the relative impact of different two-equation turbulence models on the salinity predictions is very small (Wang et al. 2011a). All three codes employ the same first-order Eulerian-Lagrangian method for momentum advection. Because the implementations are very similar to one another, differences in predictions can be attributed solely to grid resolution. This is clearly demonstrated in Fig. 3.1. Both the mean and RMS errors computed by MacWilliams et al. (2007) at Benicia and Point San Pablo are on the same asymptotic trajectories as those inferred from the results of run A. The mean error of Gross et al. (2009) is slightly higher than the results for run A at the same grid resolution. It is difficult to determine the source of the small difference of 1.0 psu at Benicia and 0.5 psu at Point San Pablo between our model and that of Gross et al. (2009), particularly since the result of Gross was calibrated over a one-year period. Nevertheless, these results suggest that the differences between the results are mainly due to grid resolution and not to the details of the implementation or numerical methods.

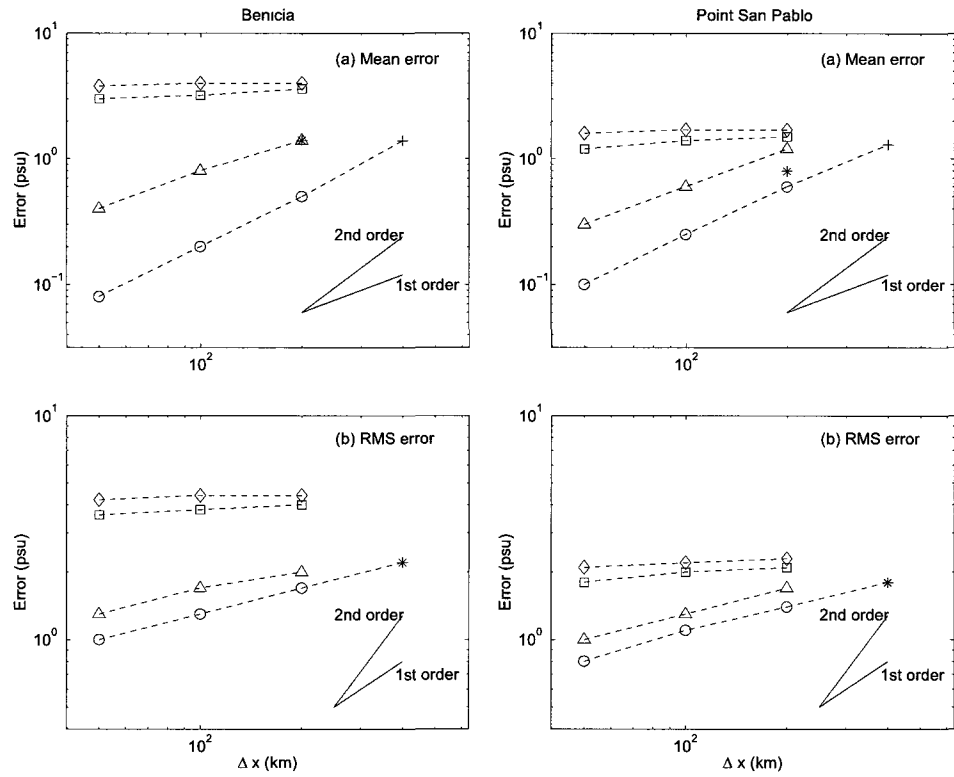


Figure 3.1: Convergence of the mean (a) and RMS (b) bottom salinity errors (in psu) as a function of grid refinement  $\Delta x$  (km) at Benicia and Point San Pablo. Legend: Run A ( $\circ$ ), Run B ( $\triangle$ ), Run C ( $\square$ ), Run D ( $\diamond$ ), result of Gross et al. (2009) (\*), result of MacWilliams et al. (2007) (+).

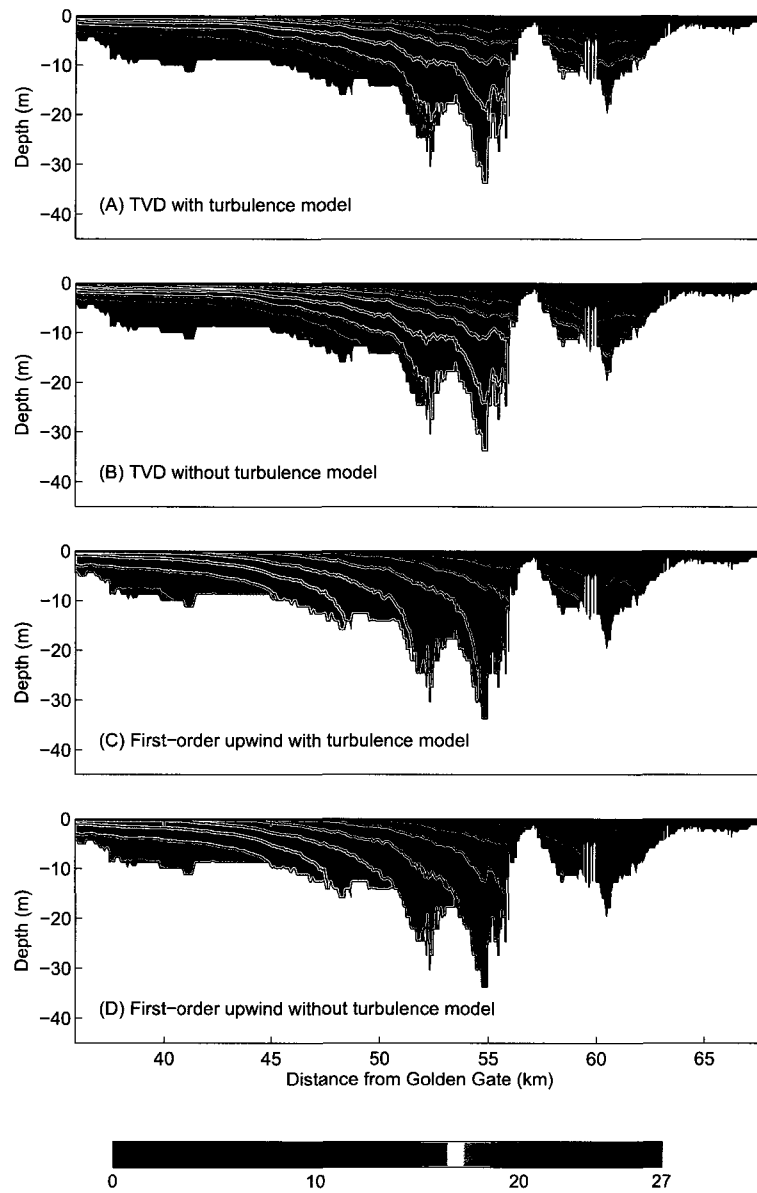


Figure 3.2: Vertical profiles of salinity (in psu) along the transect depicted in Fig. 2.1 in Carquinez Strait tidally-averaged on year day 44 on the finest mesh. Runs: (A) TVD with turbulence model (B) TVD without turbulence model (C) First-order upwind with turbulence model (D) First-order upwind without turbulence model.

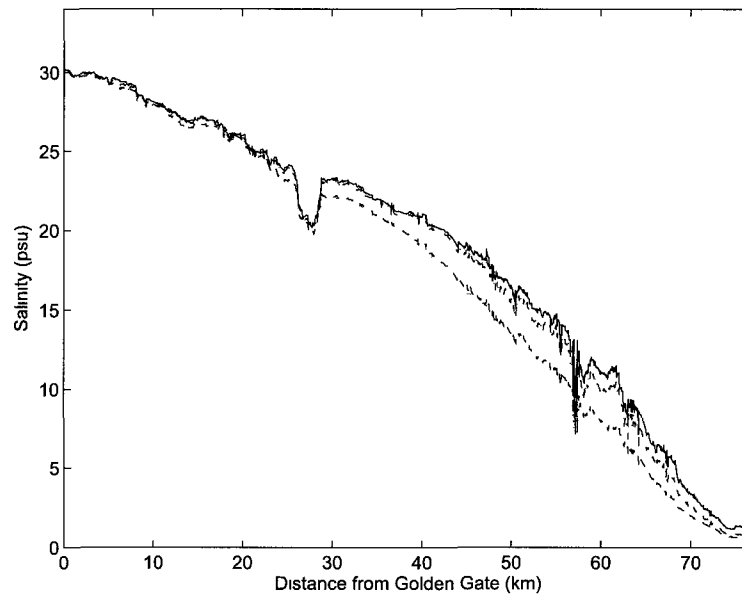


Figure 3.3: Depth-averaged salinities (in psu) from the Golden Gate along the longitudinal axis in North San Francisco Bay. Legend: (A) TVD with turbulence model (—), (B) TVD without turbulence model (---), (C) First-order upwind with turbulence model (-.-), (D) First-order upwind without turbulence model (···). Results are computed for the finest mesh.

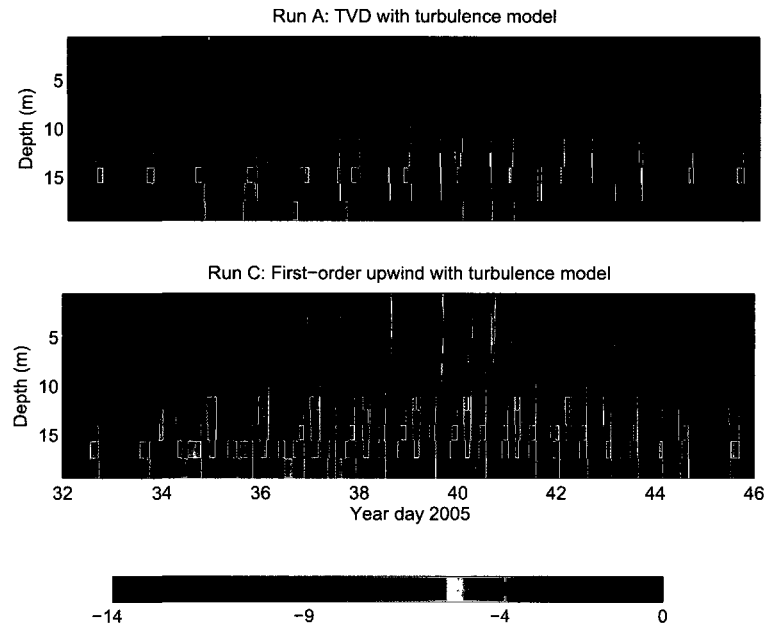


Figure 3.4: Time series of vertical profiles of the vertical eddy-diffusivity (in  $\log(\text{m}^2\text{s}^{-1})$ ) at Benicia on the finest mesh.

### 3.3 Salt flux analysis

In this section we quantify the effects of the grid resolution, advection scheme and the turbulence model on the salt flux. We compare tidally-averaged steady state salt fluxes at a cross-section in Carquinez Strait (at the location of Benicia in Fig. 2.1) for Runs A - D on the fine and coarse meshes. The salt flux simulations are performed with simplified forcing that employ idealized tides. To ensure periodicity, only two constituents are employed, namely the M2 component and an idealized K1 component which has a period that is exactly double that of M2. Simulations are run over 50 K1 cycles until the tidally-averaged salt flux is roughly in steady state. We assume steady state is reached when the difference between the seaward advection of salt is balanced by landward dispersion by less than 5% (i.e.  $(\text{advective flux} - \text{dispersive flux})/(\text{advective flux}) < 5\%$ ).

Following Fischer et al. (1979), if  $\langle \cdot \rangle$  represents the tidal average and  $\bar{\cdot}$  represents the cross-sectional integral, then the velocity normal to a cross section,  $u$ , and the salinity at the cross section,  $s$ , can be decomposed with

$$\begin{aligned} u &= u_a + u_c + u_s, \\ s &= s_a + s_c + s_s, \end{aligned}$$

where the tidally-averaged and area-integrated velocity is  $u_a = \langle \bar{u} \rangle$  and the tidally-averaged and area-integrated salinity is  $s_a = \langle \bar{s} \rangle$ . The cross-sectionally varying, tidally-averaged terms are

$$\begin{aligned} u_s &= \langle u \rangle - u_a, \\ s_s &= \langle s \rangle - s_a, \end{aligned}$$

and the cross-sectionally varying, tidally-varying terms are

$$\begin{aligned} u_c &= \bar{u} - u_a, \\ s_c &= \bar{s} - s_a. \end{aligned}$$



The tidally-averaged salt flux through a cross-section can then be written as

$$F = \left\langle \int (u_a + u_s + u_c)(s_a + s_s + s_c) dA \right\rangle = \underbrace{u_a s_a A_0}_{F_R} + \underbrace{\int u_s s_s dA_0}_{F_E} + \underbrace{\left\langle \int u_c s_c dA \right\rangle}_{F_T} \quad (3.2)$$

where  $F_R$  is the river flux,  $F_E$  is the steady exchange flux,  $F_T$  is the tidal flux, and  $A_0 = \bar{A}$  is the tidally-averaged cross-sectional area. The river flux represents mean seaward advection, while the steady exchange and tidal terms account for dispersive mechanisms. These fluxes for Runs A to D on the fine and coarse meshes are shown in Fig. 3.5. The figure also shows  $\nu = F_T/(F_E + F_T)$ , which represents the ratio of tidal to total dispersive flux (Hansen and Rattray 1965), and  $1 - \nu = F_E/(F_E + F_T)$ , which represents the ratio of steady exchange flux to the total dispersive flux.

Fig. 3.5 shows that the relative effect of the grid resolution on the salt fluxes is weak when first-order upwinding is used (runs C and D). For these runs strong numerical diffusion reduces the horizontal salinity gradients, which results in weaker baroclinic circulation and smaller stratification. This is seen in observations by Geyer (2010) in the Hudson River estuary and Monismith et al. (2002) in San Francisco Bay where the strong horizontal salinity gradient induces a baroclinic pressure gradient, which drives estuarine circulation and suppresses vertical mixing to increase stratification. We observe that the steady exchange flux,  $F_E$  is smaller than the tidal flux,  $F_T$  with first-order upwinding. When the TVD scheme is used, the resulting compressed horizontal salinity gradients lead to exchange fluxes that are larger than the tidal fluxes regardless of whether or not the turbulence model is used. Lack of the turbulence model decreases the exchange flux for runs A and B on both the fine and coarse meshes. The absence of vertical mixing leads to stronger estuarine circulation, and this weakens the longitudinal salinity gradient. The result is a reduced estuarine circulation and decreased exchange flux. This is described in Park and Kuo (1996) who show the effect of variation in vertical mixing on estuarine circulation over short and long time scales in a numerical model application to Chesapeake Bay. While lack of vertical mixing produces stronger estuarine circulation, lack of the turbulence model on the fine grid significantly increases the tidal flux ( $\nu$  increases by a factor

of four). On the coarse grid, lack of the turbulence model for run B has very little effect on the tidal flux but instead leads to a river flux that is smaller roughly by an amount equal to the decrease in steady exchange flux. Therefore, the value of  $\nu$  remains relatively unchanged on the coarse grid for runs A and B.

### 3.4 Summary

A sensitivity study is performed to understand the effects of grid resolution, the turbulence model, and the scalar transport scheme on salinity simulations in North San Francisco Bay. The best convergence rate in space is achieved when the TVD scheme is employed for salt transport and the turbulence model is employed. This accuracy degrades without the turbulence model due to a lack of feedback between vertical turbulent mixing and stratification. An expected first-order rate of convergence with respect to grid refinement is not achieved with first-order upwinding. Significant horizontal numerical diffusion associated with first-order upwinding leads to a diffuse salt wedge and decreased baroclinic circulation, resulting in negligible influence of the turbulence model and grid refinement.

The effects of grid resolution, the turbulence model and the scalar transport scheme on salt flux are investigated. Employing first-order upwinding, the salt fluxes are relatively insensitive to the turbulence model and the grid resolution. When the TVD scheme is used, the salt fluxes are larger on the fine mesh compared to the coarse mesh, as the fine mesh provides better resolution of the compressed salinity front. Lack of the turbulence model decreases the exchange flux on both fine and coarse meshes due to the absence of feedback between vertical mixing and stratification.

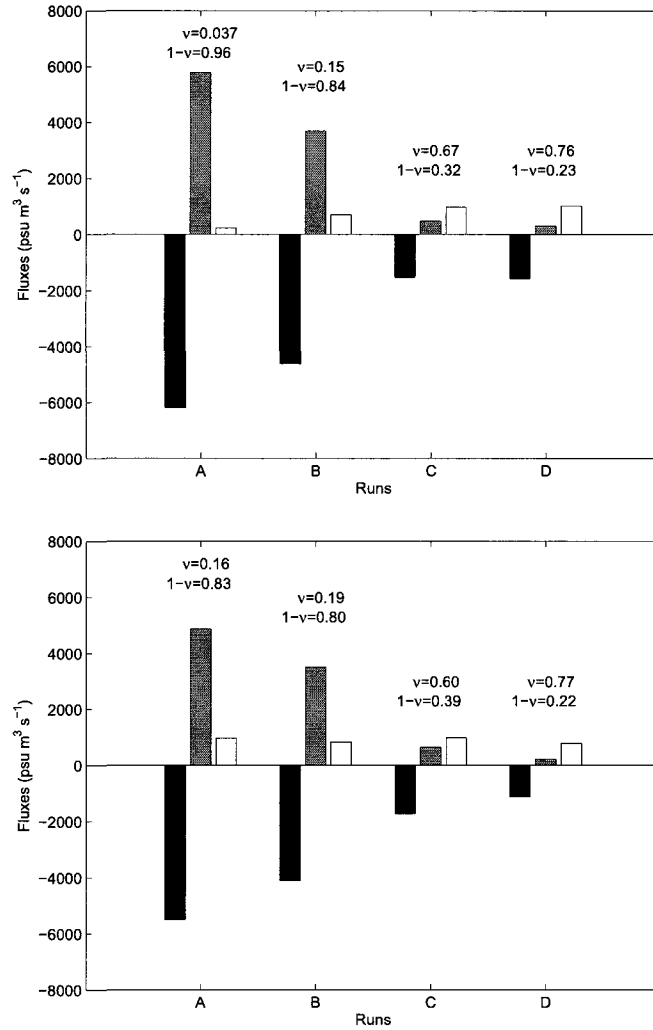


Figure 3.5: Influence of the scalar advection scheme and turbulence model on tidally-averaged salt fluxes (in  $\text{psu m}^3/\text{s}$ ) on fine (a) and coarse (b) meshes. Runs: (A) TVD with turbulence model, (B) TVD without turbulence model, (C) First-order upwind with turbulence model, (D) First-order upwind without turbulence model. Legend: Black:  $F_R$ , Gray:  $F_E$ , White:  $F_T$ . Diffusive fraction  $\nu = F_T / (F_T + F_E)$  and  $1 - \nu = F_E / (F_T + F_E)$ .

# Chapter 4

## Numerical scalar diffusion on unstructured grids

### 4.1 Introduction

In this chapter, we propose an approach to analytically derive numerical diffusion coefficients for finite-volume methods on unstructured grids by extending the Hirt analysis on Cartesian grids to unstructured grids. Two forms of computing the modified equation, termed the independent analysis and the combined analysis are presented. The numerical diffusion coefficients are analytically derived for first-order upwinding and a second-order scheme which stabilizes central differencing but introduces dispersion. A stability analysis is performed for the high- and low-order schemes, and an accuracy analysis determines the accuracy in time and space.

### 4.2 Quantification of numerical diffusion

#### 4.2.1 Numerical diffusion on Cartesian grids

If the one-dimensional advection equation with constant velocity  $u_0$  is given by

$$\frac{\partial s}{\partial t} + u_0 \frac{\partial s}{\partial x} = 0, \quad (4.1)$$

then a first-order forward in time and first-order backward in space (FTBS) discretization on a uniform Cartesian grid gives

$$s_i^{n+1} = (1 - C_0) s_i^n + C_0 s_{i-1}^n, \quad (4.2)$$

where  $C_0 = u_0 \Delta t / \Delta x$  is the Courant number, which must satisfy  $0 \leq C_0 \leq 1$  for stability. By performing a Hirt analysis (Hirt 1968) and substituting the Taylor-series expansions to obtain  $s_i^{n+1}$  and  $s_{i-1}^n$  in terms of time and space derivatives at  $i$  and  $n$ , the modified partial differential equation of the discretization (4.2) is given by, to  $O(\Delta x^2, \Delta t^2)$ ,

$$\frac{\partial s}{\partial t} + u_0 \frac{\partial s}{\partial x} = k_{xx}^{1d} \frac{\partial^2 s}{\partial x^2}, \quad (4.3)$$

where the numerical diffusion coefficient is given by

$$k_{xx}^{1d} = \frac{1}{2} u_0 \Delta x (1 - C_0) = \frac{1}{2} \frac{\Delta x^2}{\Delta t} C_0 (1 - C_0). \quad (4.4)$$

Eq. (4.3) shows that the FTBS discretization of the one-dimensional advection equation (4.1) gives the solution of the modified equation (4.3), which contains numerical diffusion that is proportional to  $\Delta x$ . The numerical diffusion coefficient gives positive diffusion under the same criteria as the stability constraint.

The two-dimensional advection equation with constant velocity  $u_0$  is given by

$$\frac{\partial s}{\partial t} + u \frac{\partial s}{\partial x} + v \frac{\partial s}{\partial y} = 0, \quad (4.5)$$

where  $u = u_0 \cos \theta$  is the velocity in the x direction and  $v = u_0 \sin \theta$  is the velocity in the y direction. A first-order forward in time and first-order backward in space (FTBS) discretization on a uniform two-dimensional Cartesian grid gives

$$s_{i,j}^{n+1} = (1 - C_x - C_y) s_{i,j}^n + C_x s_{i-1,j}^n + C_y s_{i,j-1}^n, \quad (4.6)$$

where  $C_x = C_0 \cos \theta$  and  $C_y = C_0 \sin \theta$  are Courant numbers on the x and y faces, respectively. By performing a Hirt analysis (Hirt 1968), the modified partial differential

equation of the discretization (4.6) is given by, to  $O(\Delta x^2, \Delta t^2)$ ,

$$\frac{\partial s}{\partial t} + u \frac{\partial s}{\partial x} + v \frac{\partial s}{\partial y} = k_{xx}^{2d} \frac{\partial^2 s}{\partial x^2} + k_{yy}^{2d} \frac{\partial^2 s}{\partial y^2} + k_{xy}^{2d} \frac{\partial^2 s}{\partial x \partial y}, \quad (4.7)$$

where the numerical diffusion coefficients are given by

$$\begin{aligned} k_{xx}^{2d} &= \frac{1}{2} u_0 \Delta x (1 - C_0 \cos \theta) \cos \theta, \\ k_{yy}^{2d} &= \frac{1}{2} u_0 \Delta y (1 - C_0 \sin \theta) \sin \theta, \\ k_{xy}^{2d} &= -\frac{1}{2} u_0 \Delta x C_0 \sin 2\theta. \end{aligned} \quad (4.8)$$

The FTBS discretization of the two-dimensional advection equation (4.5) leads to the modified equation (4.7) which has numerical diffusion that is proportional to the grid spacing. When  $\theta = 0$  the numerical diffusion coefficients are the same as the one-dimensional Cartesian grid, and stability is governed by  $0 \leq C_0 \leq 1$ .

A stability analysis is performed to derive the general constraint for arbitrary  $\theta$ . The numerical diffusion coefficients are written as a diffusion tensor of the form

$$K_D = \begin{bmatrix} k_{xx} & \frac{1}{2} k_{xy} \\ \frac{1}{2} k_{xy} & k_{yy} \end{bmatrix}, \quad (4.9)$$

where the factor of 1/2 is required to satisfy the identity

$$\frac{\partial}{\partial x_i} \left( K_{ij} \frac{\partial s}{\partial x_j} \right) = k_{xx} \frac{\partial^2 s}{\partial x^2} + k_{xy} \frac{\partial^2 s}{\partial x \partial y} + k_{yy} \frac{\partial^2 s}{\partial y^2},$$

where the Einstein summation convention is assumed and  $i, j=1, 2$ . The stability properties are determined by diagonalizing the diffusion tensor  $K_D$  to obtain

$$D = M^{-1} K_D M, \quad (4.10)$$

where  $D$  is the diagonal matrix constructed from the corresponding eigenvalues and  $M$  is a matrix composed of the eigenvectors of  $K_D$ . Diagonalizing a matrix is equivalent to transforming the diffusion tensor into a special set of coordinate axes such that the

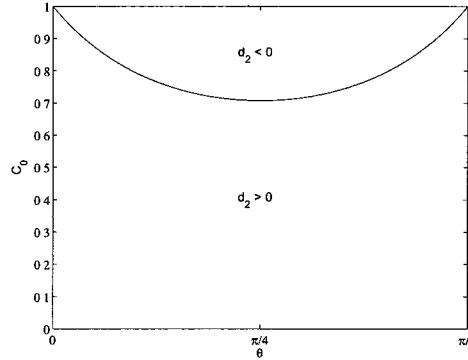


Figure 4.1: Stability region for first-order upwinding based on the sign of the principle components of the diffusion tensor  $d_1^{2d}$  and  $d_2^{2d}$ . When  $d_1^{2d} \geq 0$  and  $d_2^{2d} \geq 0$  the scheme is stable. The black line shows the contour of  $d_2^{2d} = 0$  while  $d_1^{2d} \geq 0$  for  $0 \leq C_0 \leq 1$  and  $0 \leq \theta \leq \pi/2$ .

diagonal matrix still shares the fundamental properties of the diffusion tensor. The diagonal matrix  $D$  has the form

$$D = \begin{bmatrix} d_1 & 0 \\ 0 & d_2 \end{bmatrix}. \quad (4.11)$$

Stability is achieved when the principal diagonal components of  $D$  are non-negative, such that  $d_1 \geq 0$  and  $d_2 \geq 0$  (Leveque 2011).

Fig. 4.1 shows the contours of the diffusion tensor  $d_1^{2d} = 0$  and  $d_2^{2d} = 0$  with respect to  $C_0$  and  $\theta$  for first-order upwinding in the interval  $\theta = [0, \pi/2]$ .  $d_1^{2d}$  is always positive, and thus the Courant number restriction is dependent on  $d_2^{2d}$ . The least restrictive Courant number occurs when  $\theta = 0$  and  $\pi/2$  which requires that  $0 \leq C_0 \leq 1$ , and the most restrictive Courant number occurs when the flow is offset by angle  $\pi/4$  relative to the grid which requires that  $0 \leq C_0 \leq 1/\sqrt{2}$ . This satisfies the Courant number restriction  $C_x + C_y \leq 1$  (Fletcher 1997).

### Second-order schemes

The first-order upwind scheme introduces first-order numerical diffusion, which tends to excessively smooth scalar gradients. An alternative is to employ forward-in-time

and centered-in-space differencing (FTCS) which leads to unconditional instability due to the introduction of negative diffusion. A well-known method that combats this negative diffusion is the Lax-Wendroff scheme (Lax and Wendroff 1960) that introduces enough positive diffusion to cancel the negative diffusion arising from central differencing. This gives rise to numerical dispersion as the leading term in the truncation error. The second-order discretization of Eq. (4.1) can be written as

$$s_i^{n+1} = s_i^n - \frac{1}{2}C_0 (s_{i+1}^n - s_{i-1}^n) + \frac{1}{2}\psi C_0^2 (s_{i+1}^n - 2s_i^n + s_{i-1}^n), \quad (4.12)$$

where  $\psi$  is a constant. When  $\psi = 0$ , Eq. (4.12) reduces to FTCS, while when  $\psi = 1$  it becomes the Lax-Wendroff scheme. By performing a Hirt analysis (Hirt 1968), the modified partial differential equation of the discretization (4.12) is given by, to  $O(\Delta x^3, \Delta t^3)$ ,

$$\frac{\partial s}{\partial t} + u_0 \frac{\partial s}{\partial x} = k_{\text{xx}}^{1d} \frac{\partial^2 s}{\partial x^2} + k_{\text{xxx}}^{1d} \frac{\partial^3 s}{\partial x^3}, \quad (4.13)$$

where the numerical diffusion coefficient is given by

$$k_{\text{xx}}^{1d} = \frac{1}{2}u_0\Delta x C_0(\psi - 1) = \frac{1}{2} \frac{\Delta x^2}{\Delta t} C_0^2(\psi - 1), \quad (4.14)$$

and the numerical dispersion coefficient is given by

$$k_{\text{xxx}}^{1d} = -\frac{1}{6}u_0\Delta x^2(1 - C_0^2) = -\frac{1}{6} \frac{\Delta x^3}{\Delta t} C_0(1 - C_0^2). \quad (4.15)$$

This shows how, when  $\psi = 0$ , the resulting FTCS discretization is unstable due to the introduction of negative diffusion. By setting  $\psi = 1$ , Eq. (4.12) reduces to the Lax-Wendroff scheme (Lax and Wendroff 1960) which produces  $k_{\text{xx}}^{1d} = 0$  and  $k_{\text{xxx}}^{1d} \neq 0$ . In this case stability is governed by the requirement of negative dispersion or  $0 \leq C_0 \leq 1$ , which can be interpreted as requiring that dispersion must produce waves that are slower than  $u_0$ . While more accurate, the Lax-Wendroff scheme produces oscillations due to the numerical dispersion. These oscillations can be eliminated by adjusting the amount of anti-diffusion in a way that satisfies the Total Variation Diminishing (TVD) constraint (Harten 1983). TVD schemes employ a nonconstant  $\psi$ , which



makes a Hirt analysis difficult. Therefore, the modified equation is derived using a constant  $\psi$ .

The second-order discretization of the two-dimensional advection equation (4.5) is given by

$$\begin{aligned} s_{i,j}^{n+1} = & s_{i,j} - \frac{1}{2}C_x (s_{i+1,j} - s_{i-1,j}) - \frac{1}{2}C_y (s_{i,j+1} - s_{i,j-1}) \\ & + \frac{1}{2}\psi C_x^2 (s_{i+1,j} - 2s_{i,j} + s_{i-1,j}) + \frac{1}{2}\psi C_y^2 (s_{i,j+1} - 2s_{i,j} + s_{i,j-1}). \end{aligned} \quad (4.16)$$

In theory the extension of one-dimensional methods to multi-dimensions is unstable (Lax and Wendroff 1964), however, many ocean models employ single-step advection schemes with higher-order interpolation on cell faces (Casulli and Zanolli 2005; Gross et al. 1999a). We find that a larger value of  $\psi$  can be chosen to obtain positive numerical diffusion, which is required to obtain stability.

By performing a Hirt analysis (Hirt 1968), the modified partial differential equation of the discretization (4.16) is given by, to  $O(\Delta x^3, \Delta t^3)$ ,

$$\begin{aligned} \frac{\partial s}{\partial t} + u \frac{\partial s}{\partial x} + v \frac{\partial s}{\partial y} = & k_{xx}^{2d} \frac{\partial^2 s}{\partial x^2} + k_{yy}^{2d} \frac{\partial^2 s}{\partial y^2} + k_{xy}^{2d} \frac{\partial^2 s}{\partial x \partial y} + k_{xxx}^{2d} \frac{\partial^3 s}{\partial x^3} + k_{yyy}^{2d} \frac{\partial^3 s}{\partial y^3} \\ & + k_{xxy}^{2d} \frac{\partial^3 s}{\partial x^2 \partial y} + k_{xyy}^{2d} \frac{\partial^3 s}{\partial y^2 \partial x}, \end{aligned} \quad (4.17)$$

where the numerical diffusion coefficients are given by

$$\begin{aligned} k_{xx}^{2d} &= \frac{1}{2}u_0^2 \Delta t (\psi - 1) \cos^2 \theta, \\ k_{yy}^{2d} &= \frac{1}{2}u_0^2 \Delta t (\psi - 1) \sin^2 \theta, \\ k_{xy}^{2d} &= -\frac{1}{2}u_0^2 \Delta t \sin 2\theta. \end{aligned} \quad (4.18)$$

The numerical dispersion coefficients are given by

$$\begin{aligned}
 k_{xxx}^{2d} &= -\frac{1}{6}u_0\Delta x^2(1 - C_0^2 \cos^2 \theta) \cos \theta, \\
 k_{yyy}^{2d} &= -\frac{1}{6}u_0\Delta y^2(1 - C_0^2 \sin^2 \theta) \sin \theta, \\
 k_{xxy}^{2d} &= \frac{1}{4}u_0^3\Delta t^2 \sin 2\theta \cos \theta, \\
 k_{xyy}^{2d} &= \frac{1}{4}u_0^3\Delta t^2 \sin 2\theta \sin \theta.
 \end{aligned} \tag{4.19}$$

When  $\psi = 0$ , Eq. 4.16 reduces to FTCS, which is unstable since the numerical diffusion is negative. When  $\psi = 1$  it becomes the Lax-Wendroff scheme, which eliminates numerical diffusion with  $k_{xx}^{2d} = k_{yy}^{2d} = k_{xy}^{2d} = 0$  for the case that  $\theta = 0$ . Similar to first-order upwinding on two-dimensional Cartesian grids, a stability analysis is performed by diagonalizing the diffusion tensor. The Lax-Wendroff scheme is unstable since  $d_1^{2d} > 0$  and  $d_2^{2d} < 0$  except when  $\theta = 0$  and  $\pi/2$ . By setting  $\psi = 2$ , the second-order scheme can be stabilized. Similar to the second-order scheme on one-dimensional Cartesian grids, stability is governed by the requirement of negative dispersion which results in the Courant number restriction  $0 \leq C_0 \leq 1\sqrt{2}$ , and this is identical to the constraint for first-order upwinding on two-dimensional Cartesian grids.

### 4.2.2 Numerical diffusion on unstructured grids

As with the form of the discrete scalar advection equation on Cartesian grids, the fundamental problem of scalar advection on unstructured grids is interpolation of the triangle-centered values  $s_i$  onto the faces. For higher-order schemes, the difficulty in determining the directional next-neighbor information to ensure that the scheme is monotonicity preserving translates into increased difficulties in implementation (Darwish and Moukalled 2003). A number of methods are available that are based on the one-dimensional methods, and these are discussed by Darwish and Moukalled (2003) and Casulli and Zanolli (2005). The numerical diffusion associated with scalar advection on unstructured grids is determined by extending the Hirt analysis (Hirt

1968) on Cartesian grids to unstructured grids.

If we consider the multi-dimensional advection equation with a constant velocity  $\mathbf{u}_0$  of the form

$$\frac{\partial s}{\partial t} + \mathbf{u}_0 \cdot \nabla s = 0, \quad (4.20)$$

then its finite-volume form on a two-dimensional equilateral triangle in the x-y plane (shown in Fig. 4.2) with side lengths  $\Delta l_j = \Delta l$  and area  $a = \frac{\sqrt{3}}{4} \Delta l^2$  is given by

$$s_i^{n+1} = s_i^n - \frac{\Delta t \Delta l}{a} [U_\alpha (s_f)_\alpha^n + U_\beta (s_f)_\beta^n + U_\gamma (s_f)_\gamma^n], \quad (4.21)$$

where  $U_j$  is the component of the velocity in the direction of the outward normal in triangle  $i$  on face  $j$ , and  $(s_f)_j$  is the scalar concentration on face  $j$ . Using this notation, the finite-volume form of the continuity equation is given by

$$U_\alpha + U_\beta + U_\gamma = 0, \quad (4.22)$$

which ensures consistency with continuity (Gross et al. 2002). In what follows we restrict our attention to the one-dimensional advection equation and assume  $\mathbf{u}_0 = u_0 \mathbf{e}_x$ . This does not present a loss of generality because the unstructured grid problem is sensitive to the angle between the triangle edges and the flow direction. Therefore, we assume the flow direction is parallel to the x-axis and rotate the grid rather than the velocity field.

The magnitudes of the velocities on the faces of triangle  $i$  in Fig. 4.2 are given by

$$|U_\alpha| = u_0 \sin \theta, \quad (4.23)$$

$$|U_\beta| = u_0 \sin \left( \theta + \frac{\pi}{3} \right), \quad (4.24)$$

$$|U_\gamma| = u_0 \sin \left( \theta + \frac{2\pi}{3} \right). \quad (4.25)$$

We consider  $\theta$  in the interval  $[0, \pi/3]$ , since outside this range the signs of the face velocities will switch and the upwind cell for some of the faces will change. To obtain the numerical diffusion coefficients outside this range, we can add or subtract

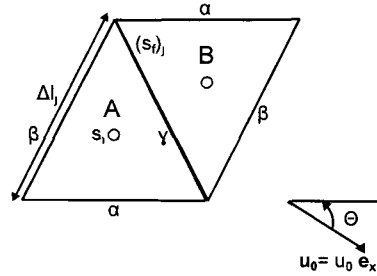


Figure 4.2: Depiction of two-dimensional equilateral triangles.  $(s_f)_j$  is the scalar concentration on face  $j$ ,  $\Delta l_j$  is the length of face  $j$ ,  $s_i$  is the scalar concentration of cell  $i$ . Three types of edges are denoted by  $\alpha$ ,  $\beta$  and  $\gamma$ . The velocity field is aligned with the x-axis and we assume  $\theta$  is defined as the angle that edge  $\alpha$  makes with the flow direction.

multiples of  $\pi/3$  until  $\theta$  falls within the  $[0, \pi/3]$  interval.

Following this convention, there are two types of triangles in our analysis as shown in Fig. 4.3 depending on the orientation of edge  $\alpha$  with respect to the x-axis or the velocity vector. The outward normal velocity components are positive on two edges and negative on one edge for type A cells (i.e.,  $U_\alpha = |U_\alpha|$ ,  $U_\beta = -|U_\beta|$  and  $U_\gamma = |U_\gamma|$ ), while there is only one edge in type B cells with a positive outward component (i.e.,  $U_\alpha = -|U_\alpha|$ ,  $U_\beta = |U_\beta|$  and  $U_\gamma = -|U_\gamma|$ ). For a grid composed of equilateral triangles, type A cells become type B cells and type B cells become type A cells if the grid is rotated by an amount  $(2m + 1)\pi/3$  ( $m = 0, 1, 2, \dots$ ). As shown in Fig. 4.4, type A cells are surrounded by type B cells, while type B cells are surrounded by type A cells.

### First-order upwinding

The simplest method to interpolate scalar values defined at the triangle centers to the faces is first-order upwinding, for which

$$(s_f)_j = \begin{cases} s_i & U_j \geq 0, \\ s_j & \text{otherwise.} \end{cases} \quad (4.26)$$

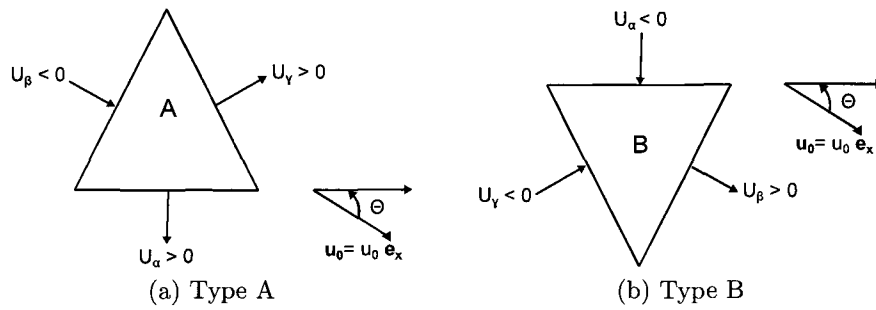


Figure 4.3: Two types of cells on unstructured grids. For type A cells, the velocity components are given by  $U_\alpha = |U_\alpha|$ ,  $U_\beta = -|U_\beta|$  and  $U_\gamma = |U_\gamma|$ . For type B cells, the velocity components are given by  $U_\alpha = -|U_\alpha|$ ,  $U_\beta = |U_\beta|$  and  $U_\gamma = -|U_\gamma|$ .

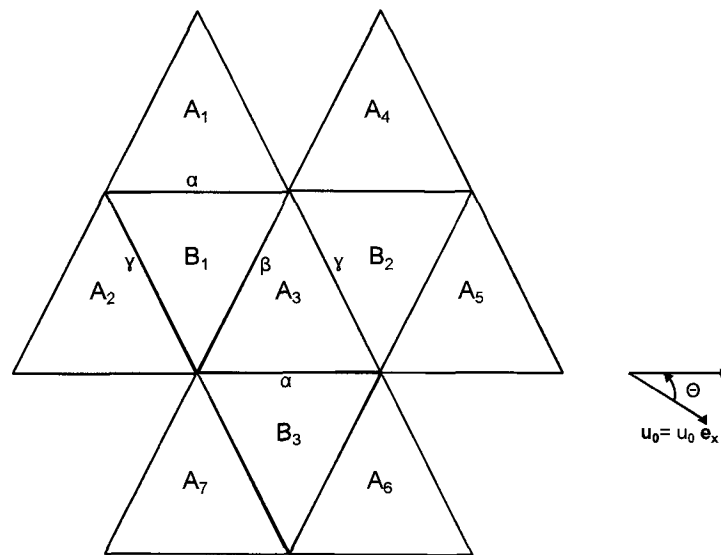


Figure 4.4: Unstructured grid composed of equilateral triangles, showing how type A cells are surrounded by type B cells and vice-versa.

Here,  $s_j$  is the scalar value in the triangle adjacent to face  $j$ , and a lack of superscript implies time step  $n$ . The cells considered in the derivation of first-order upwinding are shown in Fig. 4.4. Following Holleman et al. (2011), we adopt the notation that the scalar in type A cell  $i$  is denoted by  $A_i$  and the scalar in type B cell  $i$  is denoted by  $B_i$ . In this chapter we derive two forms of computing the modified equivalent form of the advection equation (4.20), termed the independent analysis and the combined analysis. The independent analysis separately derives the modified equations for each of the cell types A and B, while the combined analysis employs a recurrence relation to derive one equation.

### Independent analysis for first-order upwinding

If we consider a type A cell, the discretization given by Eq. (4.21) for cell  $A_3$  in Fig. 4.4 at time step  $n + 1$  is given by

$$\begin{aligned} A_3^{n+1} &= A_3^n - \frac{\Delta t \Delta l}{a} [-|U_\beta| B_1^n + |U_\alpha| A_3^n + |U_\gamma| A_3^n] \\ &= (1 - C_\beta) A_3^n + C_\beta B_1^n, \end{aligned} \quad (4.27)$$

where the Courant number on face  $j$  is defined as  $C_j = |U_j| \Delta t \Delta l / a$ . The Taylor-series expansion about time level  $n + 1$  to obtain  $A_3^{n+1}$  is given by

$$A_3^{n+1} = A_3^n + \Delta t \frac{\partial A_3^n}{\partial t} + \frac{1}{2} \Delta t^2 \frac{\partial^2 A_3^n}{\partial t^2} + \frac{1}{6} \Delta t^3 \frac{\partial^3 A_3^n}{\partial t^3} + O(\Delta t^4). \quad (4.28)$$

The Taylor-series expansion about  $A_3$  to obtain  $B_i$  is given by

$$\begin{aligned} B_i &= A_3 + \delta_{xi}^{BA} \frac{\partial A_3}{\partial x} + \delta_{yi}^{BA} \frac{\partial A_3}{\partial y} + \frac{1}{2} (\delta_{xi}^{BA})^2 \frac{\partial^2 A_3}{\partial x^2} + \frac{1}{2} (\delta_{yi}^{BA})^2 \frac{\partial^2 A_3}{\partial y^2} \\ &+ \delta_{xi}^{BA} \delta_{yi}^{BA} \frac{\partial^2 A_3}{\partial x \partial y} + \frac{1}{6} (\delta_{xi}^{BA})^3 \frac{\partial^3 A_3}{\partial x^3} + \frac{1}{6} (\delta_{yi}^{BA})^3 \frac{\partial^3 A_3}{\partial y^3} \\ &+ (\delta_{xi}^{BA})^2 \delta_{yi}^{BA} \frac{\partial^3 A_3}{\partial x^2 \partial y} + \delta_{xi}^{BA} (\delta_{yi}^{BA})^2 \frac{\partial^3 A_3}{\partial y^2 \partial x} \\ &+ O\left(\sum_{m=0}^4 \binom{4}{m} (\delta_{xi}^{BA})^m (\delta_{yi}^{BA})^{4-m}\right), \end{aligned} \quad (4.29)$$

where  $\delta_{xi}^{BA}$  and  $\delta_{yi}^{BA}$  are the x- and y-components, respectively, of the vector pointing from the center of cell  $B$  to cell  $A_3$  (see Appendix for details). Differentiation of Eq. (4.29) in time gives

$$\begin{aligned}\frac{\partial B_i}{\partial t} &= -u_0 \left[ \frac{\partial A_3}{\partial x} + \delta_{xi}^{BA} \frac{\partial^2 A_3}{\partial x^2} + O\left((\delta_{xi}^{BA})^2\right) \right], \\ \frac{\partial^2 B_i}{\partial t^2} &= u_0^2 \left[ \frac{\partial^2 A_3}{\partial x^2} + O(\delta_{xi}^{BA}) \right],\end{aligned}\tag{4.30}$$

where we have used the one-dimensional advection equation to convert the time-derivatives of  $A_3$  to space derivatives, viz

$$\begin{aligned}\frac{\partial A_3}{\partial t} &= -u_0 \frac{\partial A_3}{\partial x}, \\ \frac{\partial^2 A_3}{\partial t^2} &= u_0^2 \frac{\partial^2 A_3}{\partial x^2}.\end{aligned}$$

Substitution of the Taylor-series expansions in time and space from Eqs. (4.28) and (4.29) into the finite-volume discretization for a type A cell (4.27) gives the modified equivalent partial differential equation, to  $O(\Delta t^2, \Delta l^2)$ ,

$$\frac{\partial A}{\partial t} + u^A \frac{\partial A}{\partial x} + v^A \frac{\partial A}{\partial y} = k_{xx}^A \frac{\partial^2 A}{\partial x^2} + k_{yy}^A \frac{\partial^2 A}{\partial y^2} + k_{xy}^A \frac{\partial^2 A}{\partial x \partial y},\tag{4.31}$$

where the modified equivalent advective velocities are given by

$$\begin{aligned}u^A &= \frac{1}{3}u_0 \left( 1 + 2 \cos^2 \theta + \sqrt{3} \sin 2\theta \right), \\ v^A &= \frac{1}{\sqrt{3}}u_0 \left( 1 - 2 \cos^2 \theta + \frac{1}{\sqrt{3}} \sin 2\theta \right),\end{aligned}$$

and the modified equivalent diffusion coefficients are given by

$$\begin{aligned} k_{xx}^A &= \frac{1}{2}u_0\Delta l \left[ \frac{4}{3\sqrt{3}} \sin^3 \left( \frac{\pi}{3} + \theta \right) - C_l \right], \\ k_{yy}^A &= \frac{1}{3\sqrt{3}}u_0\Delta l \sin 2 \left( \frac{\pi}{3} + \theta \right) \cos \left( \frac{\pi}{3} + \theta \right), \\ k_{xy}^A &= -\frac{2}{3\sqrt{3}}u_0\Delta l \sin 2 \left( \frac{\pi}{3} + \theta \right) \sin \left( \frac{\pi}{3} + \theta \right), \end{aligned}$$

where  $C_l = u_0\Delta t/\Delta l$  is the unstructured-grid analogue of the Courant number.

The same analysis can be performed to show that, for a type B cell, the modified equivalent partial differential equation of the discretization

$$\begin{aligned} B_1^{n+1} &= B_1^n - \frac{\Delta t \Delta l}{a} [-|U_\alpha|A_1^n - |U_\gamma|A_2^n + |U_\beta|B_1^n] \\ &= (1 - C_\alpha - C_\gamma)B_1^n + C_\alpha A_1^n + C_\gamma A_2^n \end{aligned} \quad (4.32)$$

is given by

$$\frac{\partial B}{\partial t} + u^B \frac{\partial B}{\partial x} + v^B \frac{\partial B}{\partial y} = k_{xx}^B \frac{\partial^2 B}{\partial x^2} + k_{yy}^B \frac{\partial^2 B}{\partial y^2} + k_{xy}^B \frac{\partial^2 B}{\partial x \partial y}, \quad (4.33)$$

where the modified equivalent advective velocities are given by

$$\begin{aligned} u^B &= \frac{1}{3}u_0 \left( 1 + 2 \cos^2 \theta + 4 \sin^2 \theta - \sqrt{3} \sin 2\theta \right), \\ v^B &= -\frac{1}{\sqrt{3}}u_0 \left( 1 - 2 \cos^2 \theta + \frac{1}{\sqrt{3}} \sin 2\theta \right), \end{aligned}$$

and the modified equivalent diffusion coefficients are given by

$$\begin{aligned} k_{xx}^B &= \frac{1}{2}u_0\Delta l \left[ \frac{4}{3\sqrt{3}} \cos^3 \left( \frac{\pi}{6} + \theta \right) + \frac{4}{3\sqrt{3}} \sin^3 \theta - C_l \right], \\ k_{yy}^B &= \frac{1}{3\sqrt{3}}u_0\Delta l \left[ \sin 2\theta \cos \theta + \sin 2 \left( \theta + \frac{\pi}{3} \right) \sin \left( \theta + \frac{\pi}{3} \right) \right], \\ k_{xy}^B &= \frac{2}{3\sqrt{3}}u_0\Delta l \left[ \sin 2 \left( \frac{\pi}{6} + \theta \right) \cos \left( \frac{\pi}{6} + \theta \right) - \sin 2\theta \sin \theta \right]. \end{aligned}$$

As pointed out by Holleman et al. (2011), the modified equivalent partial differential



equations for type A and B cells in Eqs. (4.31) and (4.33) show that the finite-volume discretizations (4.27) and (4.32) are inconsistent with the one-dimensional advection equation (4.1) because of the introduction of nonzero lateral advection  $v^A$  and  $v^B$  which vanish only when  $\theta = \pi/6$ . Furthermore, streamwise velocities  $u^A \neq u_0$  and  $u^B \neq u_0$  unless  $\theta = 0$  and  $\pi/3$ . Despite the inconsistency with the modified equations, the average of the independent forms for types A and B cells is consistent since  $u^A + u^B = 2u_0$  and  $v^A + v^B = 0$ . The average of the modified equations for type A and B cells in Eqs. (4.31) and (4.33) is thus given by, to  $O(\Delta t^2, \Delta l^2)$  and after substitution of  $s = (A + B)/2$ ,

$$\frac{\partial s}{\partial t} + u_0 \frac{\partial s}{\partial x} = k_{xx} \frac{\partial^2 s}{\partial x^2} + k_{yy} \frac{\partial^2 s}{\partial y^2} + k_{xy} \frac{\partial^2 s}{\partial x \partial y}, \quad (4.34)$$

where the numerical diffusion coefficients are given by

$$\begin{aligned} k_{xx} &= \frac{1}{2} u_0 \Delta l \left[ \frac{5}{12\sqrt{3}} \sin \theta + \frac{7}{12} \cos \theta - C_l \right], \\ k_{yy} &= \frac{1}{12} u_0 \Delta l \cos \theta \left[ 1 + \frac{2}{\sqrt{3}} \sin 2\theta \right], \\ k_{xy} &= \frac{1}{6} u_0 \Delta l \sin \theta \left[ 1 - \frac{2}{\sqrt{3}} \sin 2\theta \right]. \end{aligned} \quad (4.35)$$

Although the independent analysis results in the correct advective speed  $u_0$  and the lateral modified velocities cancel, we would expect the lateral diffusion coefficient  $k_{yy}$  to vanish when  $\theta = 0$  because there cannot be any net lateral transport when one of the triangles edges is aligned with the flow, i.e. when  $\theta = 0$  and  $\pi/3$ . However, from Eq. 4.35 when  $\theta = 0$  and  $\pi/3$  the lateral diffusion coefficient is  $k_{yy} = (1/12)u_0\Delta l$ . As described in the next section, the combined analysis of Holleman et al. (2011) removes the diffusive bias and gives the correct numerical diffusion coefficient.

### Combined analysis for first-order upwinding

Following the method in Holleman et al. (2011), a combined analysis is performed using a recurrence relation by expanding the values for type B cells in terms of values

in type A cells. Details can be found in Holleman et al. (2011), although the basic methodology is repeated here for clarity. Considering a type B cell, the discretization given by Eq. (4.21) for cell  $B_1$  in Fig. 4.4 at time step  $n$  is given by

$$\begin{aligned} B_1^n &= B_1^{n-1} - \frac{\Delta t \Delta l}{a} [-|U_\alpha| A_1^{n-1} - |U_\gamma| A_2^{n-1} + |U_\beta| B_1^{n-1}] \\ &= (1 - C_\alpha - C_\gamma) B_1^{n-1} + C_\alpha A_1^{n-1} + C_\gamma A_2^{n-1} \\ &= \epsilon B_1^{n-1} + C_\alpha A_1^{n-1} + C_\gamma A_2^{n-1}, \end{aligned} \quad (4.36)$$

where  $\epsilon = 1 - C_\alpha - C_\gamma$ . Expressing  $B_1^n$  in terms of  $k$  time steps prior to time step  $n$  gives

$$B_1^n = \epsilon^k B_1^{n-k} + C_\alpha \sum_{j=1}^k A_1^{n-j} \epsilon^{j-1} + C_\gamma \sum_{j=1}^k A_2^{n-j} \epsilon^{j-1}. \quad (4.37)$$

The Taylor-series expansion about time level  $n-1$  to obtain  $B_1^{n-1}$  is given by

$$B_1^{n-1} = B_1^n - \Delta t \frac{\partial B_1^n}{\partial t} + \frac{1}{2} \Delta t^2 \frac{\partial^2 B_1^n}{\partial t^2} - \frac{1}{6} \Delta t^3 \frac{\partial^3 B_1^n}{\partial t^3} + O(\Delta t^4). \quad (4.38)$$

Using Eqs. (4.37) and (4.38) together gives

$$\begin{aligned} B_1^n &= \sum_{j=0}^{\infty} \epsilon^j \left\{ C_\alpha \left[ A_1^n - (j+1)\Delta t \frac{\partial A_1^n}{\partial t} + \frac{1}{2}(j+1)^2 \Delta t \frac{\partial^2 A_1^n}{\partial t^2} \right] \right. \\ &\quad \left. + C_\gamma \left[ A_2^n - (j+1)\Delta t \frac{\partial A_2^n}{\partial t} + \frac{1}{2}(j+1)^2 \Delta t \frac{\partial^2 A_2^n}{\partial t^2} \right] \right\}. \end{aligned} \quad (4.39)$$

Rearranging Eq. (4.39) gives

$$\begin{aligned} B_1^n &= \sum_{j=0}^{\infty} \epsilon^j \left[ C_\alpha A_1^n + C_\gamma A_2^n - (j+1)\Delta t \left( C_\alpha \frac{\partial A_1^n}{\partial t} + \Delta C_\gamma \frac{\partial A_2^n}{\partial t} \right) \right. \\ &\quad \left. + \frac{(j+1)^2 \Delta t^2}{2} \left( C_\alpha \frac{\partial^2 A_1^n}{\partial t^2} + C_\gamma \frac{\partial^2 A_2^n}{\partial t^2} \right) \right]. \end{aligned} \quad (4.40)$$

The infinite series in Eq. (4.40) can be expressed in closed form to give

$$B_1^n = \frac{1}{1-\epsilon}(C_\alpha A_1^n + C_\gamma A_2^n) - \frac{\Delta t}{(1-\epsilon)^2} \left( C_\alpha \frac{\partial A_1^n}{\partial t} + C_\gamma \frac{\partial A_2^n}{\partial t} \right) + \frac{(1+\epsilon)\Delta t^2}{2(1-\epsilon)^3} \left( C_\alpha \frac{\partial^2 A_1^n}{\partial t^2} + C_\gamma \frac{\partial^2 A_2^n}{\partial t^2} \right). \quad (4.41)$$

Considering a type A cell, the discretization given by Eq. (4.21) for cell  $A_3$  at time step  $n+1$  is given by

$$A_3^{n+1} = A_3^n - \frac{\Delta t \Delta l}{a} [-|U_\beta| B_1^n + |U_\alpha| A_3^n + |U_\gamma| A_3^n] = (1 - C_\beta) A_3^n + C_\beta B_1^n. \quad (4.42)$$

Substitution of  $B_1^n$  from Eq. (4.41) into Eq. (4.42) produces a discrete equation in terms of  $A_i^n$ ,  $A_i^{n+1}$  and the time derivatives of  $A_i$ . Expressions for  $A_1$  and  $A_2$  are obtained in terms of  $A_3$  using the Taylor-series expansion about  $A_3$  to obtain

$$\begin{aligned} A_i = & A_3 + \delta_{xi}^{AA} \frac{\partial A_3}{\partial x} + \delta_{yi}^{AA} \frac{\partial A_3}{\partial y} + \frac{1}{2} (\delta_{xi}^{AA})^2 \frac{\partial^2 A_3}{\partial x^2} + \frac{1}{2} (\delta_{yi}^{AA})^2 \frac{\partial^2 A_3}{\partial y^2} \\ & + \delta_{xi}^{AA} \delta_{yi}^{AA} \frac{\partial^2 A}{\partial x \partial y} + \frac{1}{6} (\delta_{xi}^{AA})^3 \frac{\partial^3 A_3}{\partial x^3} + \frac{1}{6} (\delta_{yi}^{AA})^3 \frac{\partial^3 A_3}{\partial y^3} \\ & + \frac{1}{2} (\delta_{xi}^{AA})^2 \delta_{yi}^{AA} \frac{\partial^3 A_3}{\partial x^2 \partial y} + \frac{1}{2} \delta_{xi}^{AA} (\delta_{yi}^{AA})^2 \frac{\partial^3 A_3}{\partial x \partial y^2} \\ & + O \left( \sum_{m=0}^4 \binom{4}{m} (\delta_{xi}^{AA})^m (\delta_{yi}^{AA})^{4-m} \right), \end{aligned} \quad (4.43)$$

where  $\delta_{xi}^{AA}$  and  $\delta_{yi}^{AA}$  are the x- and y-components, respectively, of the vector pointing from the center of cell  $A_i$  to cell  $A_3$ . Differentiation of Eq. (4.43) in time and applying Eq. (4.1) gives

$$\begin{aligned} \frac{\partial A_i}{\partial t} &= -u_0 \left( \frac{\partial A_3}{\partial x} + \delta_{xi}^{AA} \frac{\partial^2 A}{\partial x^2} + O \left( (\delta_{xi}^{AA})^2 \right) \right), \\ \frac{\partial^2 A_i}{\partial t^2} &= u_0^2 \left( \frac{\partial^2 A_3}{\partial x^2} \right) + O \left( \delta_{xi}^{AA} \right). \end{aligned} \quad (4.44)$$

Substitution of the Taylor-series expansions for  $A_1$  and  $A_2$  from Eq. (4.43) into Eq. (4.42) and converting the second time derivative to a spatial derivative with Eq. (4.44) gives, to  $O(\Delta t^2, \Delta l^2)$ , the modified partial differential equation of the finite-volume discretization for type A cells upon replacing  $A$  by  $s$ ,

$$\frac{\partial s}{\partial t} + u_0 \frac{\partial s}{\partial x} = k_{xx} \frac{\partial^2 s}{\partial x^2} + k_{yy} \frac{\partial^2 s}{\partial y^2} + k_{xy} \frac{\partial^2 s}{\partial x \partial y}, \quad (4.45)$$

where the numerical diffusion coefficients are given by

$$\begin{aligned} k_{xx} &= \frac{1}{2} u_0 \Delta l \left[ \frac{\gamma}{8\sqrt{3} \sin^2(\theta + \pi/3)} - C_l \right], \\ k_{yy} &= \frac{1}{4\sqrt{3}} u_0 \Delta l \sin 3\theta, \\ k_{xy} &= \frac{1}{2} u_0 \Delta l \sin \theta \left( 1 - \frac{2}{\sqrt{3}} \sin 2\theta \right), \end{aligned} \quad (4.46)$$

and  $\gamma = -8 \sin^5 \theta + 4\sqrt{3} \sin 2\theta \sin^3 \theta + 2 \sin^3 \theta - 3\sqrt{3} \sin 2\theta \sin \theta + 6 \sin \theta + 3\sqrt{3} \cos \theta$ . This shows that the combined analysis produces a modified equivalent partial differential equation that is consistent with the one-dimensional equation (4.1). Furthermore, the lateral and cross diffusion coefficients vanish when  $\theta = 0$  which gives  $k_{yy} = k_{xy} = 0$  and

$$k_{xx} = \frac{1}{2} u_0 \Delta l \left( \frac{1}{2} - C_l \right). \quad (4.47)$$

The equivalent one-dimensional grid spacing between triangle centers is  $\Delta x = \Delta l/2$ , so that the diffusion coefficient is given by

$$k_{xx}^{\text{e,1d}} = \frac{1}{2} u_0 \Delta x (1 - C_0), \quad (4.48)$$

which is identical to the form of the diffusion coefficient on Cartesian grids in Eq. (4.4). Like the Cartesian discretization, first-order upwinding with forward in time contains numerical diffusion that is proportional to the grid spacing.

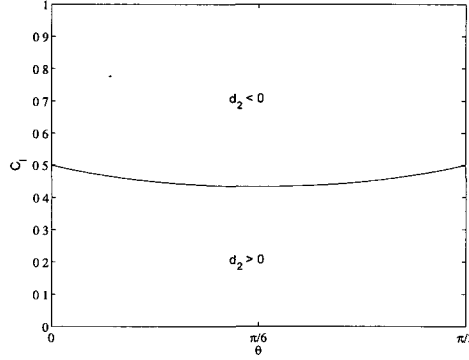


Figure 4.5: Stability region for first-order upwinding based on the sign of the principle components of the diffusion tensor  $d_1$  and  $d_2$  obtained from the combined analysis. When  $d_1 \geq 0$  and  $d_2 \geq 0$  the scheme is stable. The black line shows the contour of  $d_2 = 0$  while  $d_1 \geq 0$  for  $0 \leq C_l \leq 1$  and  $0 \leq \theta \leq \pi/3$ .

### Stability analysis of first-order upwinding

Eq. (4.48) shows that the condition on stability for the unstructured-grid discretization when  $\theta = 0$  is identical to that for the discretization on one-dimensional Cartesian grids which requires  $0 \leq C_0 \leq 1$  in order for  $k_{xx}^{1d} \geq 0$ . In general, however, the constraint can be more limiting for  $\theta \neq 0$ . A stability analysis is performed by diagonalizing the diffusion tensor, and stability is guaranteed when  $d_1 \geq 0$  and  $d_2 \geq 0$ .

Fig. 4.5 shows the contours of  $d_1 = 0$  and  $d_2 = 0$  with respect to  $C_l$  and  $\theta$  using the combined analysis for  $\theta = [0, \pi/3]$ . The Courant number constraints are obtained numerically.  $d_1$  is always positive, and thus the Courant number restriction is dependent on  $d_2$ . The least restrictive Courant number occurs when  $\theta = 0$  and  $\pi/3$  which requires that  $0 \leq C_l \leq 1/2$ , and the most restrictive Courant number occurs when  $\theta = \pi/6$  which requires that  $0 \leq C_l \leq \sqrt{3}/4 \approx 0.43$ . The equivalent condition by assuming  $\Delta l = 2\Delta x$  when  $\theta = 0$  is  $0 \leq C_0 \leq 1$  and when  $\theta = \pi/6$  is  $0 \leq C_0 \leq \sqrt{3}/2 \approx 0.87$ . In comparison, the constraint is stricter on two-dimensional Cartesian grids, and the most restrictive Courant number occurs when  $\theta = \pi/4$ , which requires that  $0 \leq C_0 \leq 1/\sqrt{2} \approx 0.71$ .

### Second-order scheme

In this section, we derive the form of the numerical diffusion coefficients for a second-order advection scheme for which the face values are given by

$$(s_f)_j = \frac{1}{2}(s_j + s_i) - \frac{1}{2}\psi C_j(s_j - s_i), \quad (4.49)$$

where  $s_j$  is the scalar value in the triangle sharing face  $j$  with triangle  $i$ , the face Courant number is given by  $C_j = U_j \Delta t \Delta l / a$ , and  $\psi$  is the limiter function. Eq. (4.49) represents a sum of a higher-order average term from central-differencing and a lower-order diffusive term. When  $\psi = 0$ , Eq. (4.49) reduces to central-differencing, and when  $\psi = 1$ , it becomes the Lax-Wendroff scheme. On one-dimensional Cartesian grids the Lax-Wendroff scheme eliminates numerical diffusion when  $\psi = 1$  which introduces anti-diffusion at the expense of dispersion. However, on unstructured grids, the choice of  $\psi = 1$  merely reduces the numerical diffusion and produces dominant numerical dispersion. In the case of the TVD scheme, the value of  $\psi$  can be chosen such that the total variation does not increase in time, which ensures that the method is monotonicity preserving (Roe 1984; Sweby 1984). Hirt analysis cannot be performed for the TVD scheme with a nonconstant  $\psi$ , and thus we assume  $\psi$  is constant in our derivation.

The cells considered in the derivation of the modified equivalent equation for the second-order scheme are shown in Fig. 4.4. For a type A cell (i.e.,  $U_\alpha = |U_\alpha|$ ,  $U_\beta = -|U_\beta|$  and  $U_\gamma = |U_\gamma|$ ), the scalar values on the three faces of cell  $A_3$  are given by

$$\begin{aligned} s_\alpha &= \frac{1}{2}(A_3 + B_3) - \frac{1}{2}\psi C_\alpha(B_3 - A_3), \\ s_\gamma &= \frac{1}{2}(A_3 + B_2) - \frac{1}{2}\psi C_\gamma(B_2 - A_3), \\ s_\beta &= \frac{1}{2}(A_3 + B_1) + \frac{1}{2}\psi C_\beta(B_1 - A_3). \end{aligned} \quad (4.50)$$

For a type B cell (i.e.,  $U_\alpha = -|U_\alpha|$ ,  $U_\beta = |U_\beta|$  and  $U_\gamma = -|U_\gamma|$ ), the scalar values on

the three faces of cell  $B_1$  are given by

$$\begin{aligned} s_\alpha &= \frac{1}{2}(B_1 + A_1) + \frac{1}{2}\psi C_\alpha(A_1 - B_1), \\ s_\gamma &= \frac{1}{2}(B_1 + A_2) + \frac{1}{2}\psi C_\gamma(A_2 - B_1), \\ s_\beta &= \frac{1}{2}(B_1 + A_3) - \frac{1}{2}\psi C_\beta(A_3 - B_1). \end{aligned} \quad (4.51)$$

Applying a similar analysis as in first-order upwinding, we perform the Hirt analysis (Hirt 1968) to determine the modified partial differential equation using both independent and combined analyses.

### Independent analysis for the second-order scheme

Considering a type A cell, the discretization given by Eq. (4.21) for cell  $A_3$  at time step  $n + 1$  is given by

$$\begin{aligned} A_3^{n+1} &= A_3^n - \frac{\Delta t \Delta l}{a} \left\{ |U_\alpha| \left[ \frac{1}{2}(A_3^n + B_3^n) - \frac{1}{2}\psi C_\alpha(B_3^n - A_3^n) \right] \right. \\ &\quad + |U_\gamma| \left[ \frac{1}{2}(A_3^n + B_2^n) - \frac{1}{2}\psi C_\gamma(B_2^n - A_3^n) \right] \\ &\quad \left. - |U_\beta| \left[ \frac{1}{2}(A_3^n + B_1^n) + \frac{1}{2}\psi C_\beta(B_1^n - A_3^n) \right] \right\} \\ &= [1 - P_\alpha - P_\gamma - P_\beta] A_3^n - M_\alpha B_3^n - M_\gamma B_2^n - M_\beta B_1^n, \end{aligned} \quad (4.52)$$

where  $P_\alpha = \frac{1}{2}C_\alpha(1 + \psi C_\alpha)$ ,  $P_\gamma = \frac{1}{2}C_\gamma(1 + \psi C_\gamma)$ ,  $P_\beta = -\frac{1}{2}C_\beta(1 - \psi C_\beta)$ ,  $M_\alpha = \frac{1}{2}C_\alpha(1 - \psi C_\alpha)$ ,  $M_\gamma = \frac{1}{2}(1 - \psi C_\gamma)$ ,  $M_\beta = -\frac{1}{2}C_\beta(1 + \psi C_\beta)$ . Applying the Taylor-series expansions in time and space (4.28 and 4.29), the modified partial differential equation of the finite-volume discretization (4.27) for type A cells is given by, to  $O(\Delta t^3, \Delta l^3)$ ,

$$\begin{aligned} \frac{\partial A}{\partial t} + u^A \frac{\partial A}{\partial x} + v^A \frac{\partial A}{\partial y} &= k_{xx}^A \frac{\partial^2 A}{\partial x^2} + k_{yy}^A \frac{\partial^2 A}{\partial y^2} + k_{xy}^A \frac{\partial^2 A}{\partial x \partial y} + k_{xxx}^A \frac{\partial^3 A}{\partial x^3} \\ &\quad + k_{yyy}^A \frac{\partial^3 A}{\partial y^3} + k_{xxy}^A \frac{\partial^3 A}{\partial x^2 \partial y} + k_{xyy}^A \frac{\partial^3 A}{\partial y^2 \partial x}, \end{aligned} \quad (4.53)$$

where the modified equivalent advective velocities are given by

$$\begin{aligned} u^A &= u_0 \left( 1 - \frac{2}{\sqrt{3}} \psi C_l \sin \theta + \frac{4}{\sqrt{3}} \psi C_l \sin 2\theta \cos \theta \right), \\ v^A &= -2\sqrt{3} u_0 \psi C_l \cos \theta \left( 1 - \frac{4}{3} \cos^2 \theta \right), \end{aligned} \quad (4.54)$$

the modified equivalent diffusion coefficients are given by

$$\begin{aligned} k_{xx}^A &= \frac{1}{12} u_0 \Delta l \left[ 6(\psi - 1) C_l - \sqrt{3} \sin \theta + 2\sqrt{3} \sin 2\theta \cos \theta \right], \\ k_{yy}^A &= -\frac{1}{12} u_0 \Delta l \left[ 2\psi C_l + \sqrt{3} \sin \theta - 2\sqrt{3} \sin 2\theta \cos \theta \right], \\ k_{xy}^A &= \frac{\sqrt{3}}{2} u_0 \Delta l \cos \theta \left( 1 - \frac{4}{3} \cos^2 \theta \right), \end{aligned} \quad (4.55)$$

and the modified equivalent dispersion coefficients are given by

$$\begin{aligned} k_{xxx}^A &= -\frac{1}{24} u_0 \Delta l^2 \left( 1 - 4C_l^2 - \frac{10}{3\sqrt{3}} \psi C_l \sin \theta \right. \\ &\quad \left. + \frac{20}{3\sqrt{3}} \psi C_l \sin 2\theta \cos \theta \right), \\ k_{yyy}^A &= -\frac{1}{12\sqrt{3}} u_0 \Delta l^2 \psi C_l \cos \theta \left( 1 - \frac{4}{3} \cos^2 \theta \right), \\ k_{xxy}^A &= -\frac{\sqrt{3}}{4} u_0 \Delta l^2 \psi C_l \cos \theta \left( 1 - \frac{4}{3} \cos^2 \theta \right), \\ k_{xyy}^A &= -\frac{1}{24} u_0 \Delta l^2 \left( 1 + \frac{2}{\sqrt{3}} \psi C_l \sin \theta - \frac{4}{\sqrt{3}} \psi C_l \sin 2\theta \cos \theta \right). \end{aligned} \quad (4.56)$$



Similarly, for a type B cell, the discretization given by Eq. (4.21) for cell  $B_1$  at time step  $n + 1$  is given by

$$\begin{aligned}
B_1^{n+1} &= B_1^n - \frac{\Delta t \Delta l}{a} \left\{ -|U_\alpha| \left[ \frac{1}{2}(B_1^n + A_1^n) + \frac{1}{2}\psi C_\alpha(A_1^n - B_1^n) \right] \right. \\
&\quad - |U_\gamma| \left[ \frac{1}{2}(B_1^n + A_2^n) + \frac{1}{2}\psi C_\gamma(A_2^n - B_1^n) \right] \\
&\quad \left. + |U_\beta| \left[ \frac{1}{2}(B_1^n + A_3^n) - \frac{1}{2}\psi C_\beta(A_3^n - B_1^n) \right] \right\} \\
&= (1 + M_\alpha + M_\gamma + M_\beta)B_1^n + P_\alpha A_1^n + P_\gamma A_2^n + P_\beta A_3^n.
\end{aligned} \tag{4.57}$$

Applying the Taylor-series expansions in time and space (4.28 and 4.29), the modified partial differential equation for type B cells is given by, to  $O(\Delta t^3, \Delta l^3)$ ,

$$\begin{aligned}
\frac{\partial B}{\partial t} + u^B \frac{\partial B}{\partial x} + v^B \frac{\partial B}{\partial y} &= k_{xx}^B \frac{\partial^2 B}{\partial x^2} + k_{yy}^B \frac{\partial^2 B}{\partial y^2} + k_{xy}^B \frac{\partial^2 B}{\partial x \partial y} + k_{xxx}^B \frac{\partial^3 B}{\partial x^3} \\
&\quad + k_{yyy}^B \frac{\partial^3 B}{\partial y^3} + k_{xxy}^B \frac{\partial^3 B}{\partial x^2 \partial y} + k_{xyy}^B \frac{\partial^3 B}{\partial y^2 \partial x},
\end{aligned} \tag{4.58}$$

where the modified equivalent advective velocities are given by

$$\begin{aligned}
u^B &= u_0 \left( 1 + \frac{2}{\sqrt{3}}\psi C_l \sin \theta - \frac{4}{\sqrt{3}}\psi C_l \sin 2\theta \cos \theta \right), \\
v^B &= 2\sqrt{3}u_0\psi C_l \cos \theta \left( 1 - \frac{4}{3}\cos^2 \theta \right),
\end{aligned} \tag{4.59}$$

the modified equivalent diffusion coefficients are given by

$$\begin{aligned}
k_{xx}^B &= \frac{1}{12}u_0\Delta l \left[ 6(1 - \psi)C_l - \sqrt{3}\sin \theta + 2\sqrt{3}\sin 2\theta \cos \theta \right], \\
k_{yy}^B &= \frac{1}{12}u_0\Delta l \left[ 2\psi C_l - \sqrt{3}\sin \theta + 2\sqrt{3}\sin 2\theta \cos \theta \right], \\
k_{xy}^B &= -\frac{\sqrt{3}}{2}u_0\Delta l \cos \theta \left( 1 - \frac{4}{3}\cos^2 \theta \right),
\end{aligned} \tag{4.60}$$

and the modified equivalent dispersion coefficients are given by

$$\begin{aligned}
k_{xxx}^B &= -\frac{1}{24}u_0\Delta l^2 \left( 1 - 4C_l^2 + \frac{10}{3\sqrt{3}}\psi C_l \sin \theta - \frac{20}{3\sqrt{3}}\psi C_l \sin 2\theta \cos \theta \right), \\
k_{yyy}^B &= \frac{1}{12\sqrt{3}}u_0\Delta l^2\psi C_l \cos \theta \left( 1 - \frac{4}{3}\cos^2 \theta \right), \\
k_{xxy}^B &= \frac{\sqrt{3}}{4}u_0\Delta l^2\psi C_l \cos \theta \left( 1 - \frac{4}{3}\cos^2 \theta \right), \\
k_{xyy}^B &= -\frac{1}{24}u_0\Delta l^2 \left( 1 - \frac{2}{\sqrt{3}}\psi C_l \sin \theta + \frac{4}{\sqrt{3}}\psi C_l \sin 2\theta \cos \theta \right).
\end{aligned} \tag{4.61}$$

The second-order scheme results in numerical dispersion in the streamwise, lateral and cross directions, and this is similar on two-dimensional Cartesian grids. The modified equivalent equations for types A and B cells in Eqs. (4.53) and (4.58) for the second-order scheme show that, like the first-order scheme, the finite-volume discretizations (4.52) and (4.57) are inconsistent with the one-dimensional advection equation (4.1). This is due to the introduction of nonzero lateral advection  $v^A$  and  $v^B$  which vanish only when  $\theta = \pi/6$ . Furthermore, the streamwise advection  $u^A \neq u_0$  and  $u^B \neq u_0$  except when  $\theta = 0$  and  $\pi/3$ . Averaging the modified equations for type A and B cells with Eqs. (4.53) and (4.58), the modified partial differential equation is given by, to  $O(\Delta t^3, \Delta l^3)$  and after substitution of  $s = (A + B)/2$ ,

$$\begin{aligned}
\frac{\partial s}{\partial t} + u_0 \frac{\partial s}{\partial x} &= k_{xx} \frac{\partial^2 s}{\partial x^2} + k_{yy} \frac{\partial^2 s}{\partial y^2} + k_{xy} \frac{\partial^2 s}{\partial x \partial y} + k_{xxx} \frac{\partial^3 s}{\partial x^3} + k_{yyy} \frac{\partial^3 s}{\partial y^3} \\
&\quad + k_{xxy} \frac{\partial^3 s}{\partial x^2 \partial y} + k_{xyy} \frac{\partial^3 s}{\partial y^2 \partial x},
\end{aligned} \tag{4.62}$$

where the numerical diffusion coefficients are given by

$$\begin{aligned}
k_{xx} &= \frac{1}{2}u_0^2\Delta t(\psi - 1), \\
k_{yy} &= \frac{1}{6}u_0^2\Delta t\psi, \\
k_{xy} &= 0,
\end{aligned} \tag{4.63}$$

and the numerical dispersion coefficients are given by

$$\begin{aligned}
 k_{xxx} &= -\frac{1}{24}u_0\Delta l^2 (1 - 4C_l^2) , \\
 k_{yyy} &= 0 , \\
 k_{xxy} &= -\frac{\sqrt{3}}{16}u_0\Delta l^2\psi C_l \left( \frac{4}{3}\cos^2\theta - 1 \right) \cos\theta , \\
 k_{xyy} &= -\frac{1}{32}u_0\Delta l^2 \left[ \frac{4}{3\sqrt{3}}\psi C_l \sin 2\theta \cos\theta - \frac{2}{3\sqrt{3}}\psi C_l \sin\theta + 1 \right] .
 \end{aligned} \tag{4.64}$$

In contrast to those for first-order upwinding in Eq. (4.34), the numerical diffusion coefficients are independent of  $\theta$  and the cross diffusion vanishes. When  $\psi = 0$ , the negative streamwise diffusion leads to an unstable scheme, and the lateral diffusion vanishes as expected when one of the triangle edges is aligned with the flow. However, when  $\psi = 1$  the streamwise diffusion vanishes and the lateral diffusion which is independent of  $\theta$  is positive. This leads to net lateral transport when one of the triangle edges is aligned with flow, i.e.  $\theta = 0$  and  $\pi/3$ . Similar to first-order upwinding, this diffusive bias can be removed with the combined analysis as described in the next section.

### Combined analysis for the second-order scheme

Following the methodology for first-order upwinding, we perform a combined analysis by using a recurrence relation to expand the values for type B cells in terms of values in type A cells for the second-order scheme. Considering a type B cell, the discretization

given by Eq. (4.21) for cell  $B_1$  at time step  $n$  is given by

$$\begin{aligned}
B_1^n &= B_1^{n-1} - \frac{\Delta t \Delta l}{a} [-|U_\alpha| s_\alpha^{n-1} - |U_\gamma| s_\gamma^{n-1} + |U_\beta| s_\beta^{n-1}] \\
&= B_1^{n-1} - \frac{\Delta t \Delta l}{a} \left\{ -|U_\alpha| \left[ \frac{1}{2}(B_1^{n-1} + A_1^{n-1}) + \frac{1}{2}\psi C_\alpha (A_1^{n-1} - B_1^{n-1}) \right] \right. \\
&\quad - |U_\gamma| \left[ \frac{1}{2}(B_1^{n-1} + A_2^{n-1}) + \frac{1}{2}\psi C_\gamma (A_2^{n-1} - B_1^{n-1}) \right] \\
&\quad \left. + |U_\beta| \left[ \frac{1}{2}(B_1^{n-1} + A_3^{n-1}) - \frac{1}{2}\psi C_\beta (A_3^{n-1} - B_1^{n-1}) \right] \right\} \\
&= \left[ 1 + \frac{1}{2}C_\alpha(1 - \psi C_\alpha) + \frac{1}{2}C_\gamma(1 - \psi C_\gamma) - \frac{1}{2}C_\beta(1 + \psi C_\beta) \right] B_1^{n-1} \\
&\quad + \frac{1}{2}C_\alpha(1 + \psi C_\alpha)A_1^{n-1} + \frac{1}{2}C_\gamma(1 + \psi C_\gamma)A_2^{n-1} - \frac{1}{2}C_\beta(1 - \psi C_\beta)A_3^{n-1}.
\end{aligned} \tag{4.65}$$

Assuming  $\lambda = 1 + \frac{1}{2}C_\alpha(1 - \psi C_\alpha) + \frac{1}{2}C_\gamma(1 - \psi C_\gamma) - \frac{1}{2}C_\beta(1 + \psi C_\beta)$ , Eq. (4.65) simplifies to

$$B_1^n = \lambda B_1^{n-1} + P_\alpha A_1^{n-1} + P_\gamma A_2^{n-1} + P_\beta A_3^{n-1}. \tag{4.66}$$

Expressing  $B_1^n$  in terms of  $k$  time steps prior to time step  $n$  gives

$$B_1^n = \lambda^k B_1^{n-k} + P_\alpha \sum_{j=1}^k A_1^{n-j} \lambda^{j-1} + P_\gamma \sum_{j=1}^k A_2^{n-j} \lambda^{j-1} + P_\beta \sum_{j=1}^k A_3^{n-j}. \tag{4.67}$$

Using Eqs. (4.67) and (4.38) together gives

$$\begin{aligned}
B_1^n &= \sum_{j=0}^{\infty} \lambda^j \left\{ P_\alpha \left[ A_1^n - (j+1)\Delta t \frac{\partial A_1^n}{\partial t} + \frac{1}{2}(j+1)^2 \Delta t^2 \frac{\partial^2 A_1^n}{\partial t^2} \right] \right. \\
&\quad + P_\gamma \left[ A_2^n - (j+1)\Delta t \frac{\partial A_2^n}{\partial t} + \frac{1}{2}(j+1)^2 \Delta t^2 \frac{\partial^2 A_2^n}{\partial t^2} \right] \\
&\quad \left. + P_\beta \left[ A_3^n - (j+1)\Delta t \frac{\partial A_3^n}{\partial t} + \frac{1}{2}(j+1)^2 \Delta t^2 \frac{\partial^2 A_3^n}{\partial t^2} \right] \right\}.
\end{aligned} \tag{4.68}$$

Rearranging Eq. (4.68) gives

$$\begin{aligned}
B_1^n &= \frac{1}{\lambda} \sum_{j=0}^{\infty} \lambda^j \left\{ [P_\alpha A_1^n + P_\gamma A_2^n + P_\beta A_3^n] - j\Delta t \left[ P_\alpha \frac{\partial A_1^n}{\partial t} + P_\gamma \frac{\partial A_2^n}{\partial t} \right. \right. \\
&\quad \left. \left. + P_\beta \frac{\partial A_3^n}{\partial t} \right] + \frac{j^2 \Delta t^2}{2} \left[ P_\alpha \frac{\partial^2 A_1^n}{\partial t^2} + P_\gamma \frac{\partial^2 A_2^n}{\partial t^2} + P_\beta \frac{\partial^2 A_3^n}{\partial t^2} \right] \right\} \\
&\quad - \frac{1}{\lambda} [P_\alpha A_1^n + P_\gamma A_2^n + P_\beta A_3^n].
\end{aligned} \tag{4.69}$$

The infinite series in Eq. (4.69) can be expressed in closed form to give

$$\begin{aligned}
B_1^n &= \frac{1}{1-\lambda} [P_\alpha A_1^n + P_\gamma A_2^n + P_\beta A_3^n] - \frac{\Delta t}{(1-\lambda)^2} \left[ P_\alpha \frac{\partial A_1^n}{\partial t} + P_\gamma \frac{\partial A_2^n}{\partial t} \right. \\
&\quad \left. + P_\beta \frac{\partial A_3^n}{\partial t} \right] + \frac{(1+\lambda)\Delta t^2}{2(1-\lambda)^3} \left[ P_\alpha \frac{\partial^2 A_1^n}{\partial t^2} + P_\gamma \frac{\partial^2 A_2^n}{\partial t^2} + P_\beta \frac{\partial^2 A_3^n}{\partial t^2} \right] \\
&\quad - \frac{(\lambda^2 + 4\lambda + 1)\Delta t^3}{6(1-\lambda)^4} \left[ P_\alpha \frac{\partial^3 A_1^n}{\partial t^3} + P_\gamma \frac{\partial^3 A_2^n}{\partial t^3} + P_\beta \frac{\partial^3 A_3^n}{\partial t^3} \right].
\end{aligned} \tag{4.70}$$

Similarly, the infinite series in the expressions for  $B_2^n$  and  $B_3^n$  can be expressed in closed form to give

$$\begin{aligned}
B_2 &= \frac{1}{1-\lambda} [P_\alpha A_4^n + P_\gamma A_3^n + P_\beta A_5^n] - \frac{\Delta t}{(1-\lambda)^2} \left[ P_\alpha \frac{\partial A_4^n}{\partial t} + P_\gamma \frac{\partial A_3^n}{\partial t} \right. \\
&\quad \left. + P_\beta \frac{\partial A_5^n}{\partial t} \right] + \frac{(1+\lambda)\Delta t^2}{2(1-\lambda)^3} \left[ P_\alpha \frac{\partial^2 A_4^n}{\partial t^2} + P_\gamma \frac{\partial^2 A_3^n}{\partial t^2} + P_\beta \frac{\partial^2 A_5^n}{\partial t^2} \right] \\
&\quad - \frac{(\lambda^2 + 4\lambda + 1)\Delta t^3}{6(1-\lambda)^4} \left[ P_\alpha \frac{\partial^3 A_4^n}{\partial t^3} + P_\gamma \frac{\partial^3 A_3^n}{\partial t^3} + P_\beta \frac{\partial^3 A_5^n}{\partial t^3} \right], \\
B_3 &= \frac{1}{1-\lambda} [P_\alpha A_3^n + P_\gamma A_7^n + P_\beta A_7^n] - \frac{\Delta t}{(1-\lambda)^2} \left[ P_\alpha \frac{\partial A_3^n}{\partial t} + P_\gamma \frac{\partial A_7^n}{\partial t} \right. \\
&\quad \left. + P_\beta \frac{\partial A_6^n}{\partial t} \right] + \frac{(1+\lambda)\Delta t^2}{2(1-\lambda)^3} \left[ P_\alpha \frac{\partial^2 A_3^n}{\partial t^2} + P_\gamma \frac{\partial^2 A_7^n}{\partial t^2} + P_\beta \frac{\partial^2 A_6^n}{\partial t^2} \right] \\
&\quad - \frac{(\lambda^2 + 4\lambda + 1)\Delta t^3}{6(1-\lambda)^4} \left[ P_\alpha \frac{\partial^3 A_3^n}{\partial t^3} + P_\gamma \frac{\partial^3 A_7^n}{\partial t^3} + P_\beta \frac{\partial^3 A_6^n}{\partial t^3} \right].
\end{aligned} \tag{4.71}$$

Considering a type A cell, the discretization given by Eq. (4.21) for cell  $A_3$  at time step  $n + 1$  is given by

$$\begin{aligned} A_3^{n+1} &= A_3^n - \frac{\Delta t \Delta l}{a} [|U_\alpha| s_\alpha^n + |U_\gamma| s_\gamma^n - |U_\beta| s_\beta^n] \\ &= [1 - P_\alpha - P_\gamma - P_\beta] A_3^n - M_\alpha B_3^n - M_\gamma B_2^n - M_\beta B_1^n. \end{aligned} \quad (4.72)$$

Substitution of  $B_1^n$ ,  $B_2^n$  and  $B_3^n$  from Eqs. (4.70) and (4.71) into Eq. (4.72) produces a discrete equation in terms of  $A_i^n$ ,  $A_i^{n+1}$  and the time derivatives of  $A_i$ . Substitution of the Taylor-series expansions for  $A_1$ ,  $A_2$ ,  $A_4$ ,  $A_5$ ,  $A_6$  and  $A_7$  from Eq. (4.43) into Eq. (4.72) and converting the second time derivative to a spatial derivative with Eq. (4.44) gives, to  $O(\Delta t^3, \Delta l^3)$ , the modified partial differential equation of the finite-volume discretization for type A cells upon replacing  $A$  by  $s$ ,

$$\begin{aligned} \frac{\partial s}{\partial t} + u_0 \frac{\partial s}{\partial x} &= k_{xx} \frac{\partial^2 s}{\partial x^2} + k_{yy} \frac{\partial^2 s}{\partial y^2} + k_{xy} \frac{\partial^2 s}{\partial x \partial y} + k_{xxx} \frac{\partial^3 s}{\partial x^3} + k_{yyy} \frac{\partial^3 s}{\partial y^3} \\ &\quad + k_{xxy} \frac{\partial^3 s}{\partial x^2 \partial y} + k_{xyy} \frac{\partial^3 s}{\partial y^2 \partial x}, \end{aligned} \quad (4.73)$$

where the numerical diffusion coefficients are given by

$$\begin{aligned} k_{xx} &= \frac{1}{2} u_0^2 \Delta t \left( \frac{16}{3} \psi \cos^6 \theta - 8 \psi \cos^4 \theta + 3 \psi \cos^2 \theta + \frac{2}{3} \psi - 1 \right), \\ k_{yy} &= \frac{1}{6} u_0^2 \Delta t \psi \sin^2 \theta (1 - 8 \cos^2 \theta + 16 \cos^4 \theta), \\ k_{xy} &= \frac{1}{2} u_0^2 \Delta t \psi \sin 2\theta \left( 1 - \frac{16}{3} \cos^2 \theta + \frac{16}{3} \cos^4 \theta \right), \end{aligned} \quad (4.74)$$

and the numerical dispersion coefficients are given by

$$\begin{aligned} k_{xxx} &= -\frac{1}{24} u_0 \Delta l^2 (1 - 4C_l^2), \\ k_{yyy} &= \frac{1}{48} u_0 \Delta l^2 \sin 2\theta (16 \cos^4 \theta - 16 \cos^2 \theta + 3), \\ k_{xxy} &= -\frac{1}{16} u_0 \Delta l^2 \sin 2\theta (16 \cos^4 \theta - 16 \cos^2 \theta + 3), \\ k_{xyy} &= -\frac{1}{8} u_0 \Delta l^2 \sin^2 \theta (16 \cos^4 \theta - 8 \cos^2 \theta + 1). \end{aligned} \quad (4.75)$$

This shows that the combined analysis produces a modified equivalent partial differential equation that is consistent with the one-dimensional equation (4.1). Similar to first-order upwinding, the lateral and cross diffusion coefficients vanish when  $\theta = 0$  which gives

$$k_{xx} = \frac{1}{2}u_0^2\Delta t(\psi - 1). \quad (4.76)$$

which is identical to the form of  $k_{xx}$  for two-dimensional Cartesian grids in Eq. (4.18) when  $\theta = 0$ . Similar to Cartesian grids, the lateral and cross-dispersion coefficients vanish when  $\theta = 0$  and the longitudinal dispersion is

$$k_{xxx} = -\frac{1}{24}u_0\Delta l^2(1 - 4C_l^2). \quad (4.77)$$

Using  $\Delta x = \Delta l/2$ , the equivalent longitudinal dispersion coefficient is

$$k_{xxx}^{e,1d} = -\frac{1}{6}u_0\Delta x^2(1 - C_0^2), \quad (4.78)$$

which is identical to the dispersion coefficient on two-dimensional Cartesian grids in Eq. (4.19) when  $\theta = 0$ .

### Stability analysis for the second-order scheme

A stability analysis is performed by analyzing the principal diagonal components, which are obtained from diagonalization of the diffusion tensor as was performed for first-order upwinding in Section 4.2.2. For the case that  $\psi = 1$ , the unstructured-grid scheme is unstable with  $d_1 \geq 0$  and  $d_2 \leq 0$ , although the Lax-Wendroff scheme on one-dimensional Cartesian grids removes numerical diffusion, i.e.,  $k_{xx}^{1d} = 0$  with  $\psi = 1$  (Eq. 4.14).  $\psi \geq 1.5$  results in a stable unstructured-grid scheme with  $d_1 \geq 0$  and  $d_2 \geq 0$ . We choose  $\psi = 1.5$  in our simulations to minimize numerical diffusion and for stability.

The Courant number constraint is determined from Von Neumann stability analysis (VonNeumann and Richtmyer 1950) and by substituting  $s = \hat{s} \exp[i(kx + ly)]$ , which gives us  $0 \leq C_l \leq 1/2\sqrt{\psi}$ . The choice  $\psi = 1.5$  leads to the Courant number

condition  $0 \leq C_l \leq 1/\sqrt{6} \approx 0.41$  for all  $\theta$ . The equivalent constraint by assuming  $\Delta l = 2\Delta x$  is  $0 \leq C_0 \leq 2/\sqrt{6} \approx 0.82$ . This is similar to the most restrictive Courant number constraint for first-order upwinding on unstructured grids, which is  $0 \leq C_0 \leq \sqrt{3}/2 \approx 0.87$  when  $\theta = \pi/6$ . A more restrictive Courant condition is found on Cartesian grids for both the first- and second-order schemes, which require  $0 \leq C_0 \leq 1/\sqrt{2} \approx 0.71$  for stability. We validate the diffusion and dispersion coefficients in the next section.

### 4.3 Numerical simulations

We perform numerical simulations to verify the analytical theory developed in the previous sections. The method of spatial moments analysis is employed to estimate the numerical diffusion coefficients in idealized simulations. This technique is commonly used to study the transport of a solute plume in groundwater (Freyberg 1986; Roberts et al. 1986; Sudicky 1986; LeBlanc et al. 1991). The zeroth moment yields the total mass of the plume, the first moment yields the mean location of the center of mass of the plume, and the second moment relates to spreading of the plume about its center of mass. We define the numerical diffusion coefficients that are computed with the spatial moments analysis as  $k_{xx,m}$ ,  $k_{yy,m}$ , and  $k_{xy,m}$ , and these are given by

$$k_{xx,m} = \frac{1}{2} \frac{\partial \sigma_x^2}{\partial t}, \quad (4.79)$$

$$k_{yy,m} = \frac{1}{2} \frac{\partial \sigma_y^2}{\partial t}, \quad (4.80)$$

$$k_{xy,m} = \frac{1}{2} \frac{\partial \text{cov}_{xy}}{\partial t}, \quad (4.81)$$

where  $\sigma_x = \frac{m_{2x}}{m_0} - \left(\frac{m_{1x}}{m_0}\right)^2$  is the variance in the x direction,  $\sigma_y = \frac{m_{2y}}{m_0} - \left(\frac{m_{1y}}{m_0}\right)^2$  is the variance in the y direction, and  $\text{cov}_{xy} = \frac{1}{m_0} m_{xy}$  is the x-y covariance. Here,  $m_0$  is the zeroth moment,  $m_{1x}$  is the first moment in the x direction,  $m_{1y}$  is the first moment in the y direction,  $m_{2x}$  is the second moment in the x direction,  $m_{2y}$  is the second moment in the y direction and  $m_{xy}$  is the cross-correlation. The diffusion coefficients computed with the spatial moments analysis are written as a diffusion tensor of the



form

$$K_m = \begin{bmatrix} k_{xx} & \frac{1}{2}k_{xy} \\ \frac{1}{2}k_{xy} & k_{yy} \end{bmatrix}. \quad (4.82)$$

In order to compare these to the flow-aligned analytically derived coefficients,  $K_m$  is transformed into a coordinate system that is aligned with the flow using

$$K_r = R_\theta K_m R_\theta^T, \quad (4.83)$$

where the rotated diffusion tensor is given by

$$K_r = \begin{bmatrix} k_{xx,r} & \frac{1}{2}k_{xy,r} \\ \frac{1}{2}k_{xy,r} & k_{yy,r} \end{bmatrix}, \quad (4.84)$$

and where the rotation matrix is given by

$$R_\theta = \begin{bmatrix} \cos \theta & -\sin \theta \\ \sin \theta & \cos \theta \end{bmatrix}. \quad (4.85)$$

In what follows, rather than rotating the grid, we keep the grid fixed but rotate the flow by an angle  $\theta$  with respect to the grid. This amounts to a rotation in the opposite sense of that depicted in Fig. 4.2. The diffusion coefficients in Section 4.2.2 are then compared to the transformed coefficients in Eq. (4.84).

We advect a passive tracer field in a channel of length  $L = 100$  km and width  $W = 100$  km. The tracer field is advected in a steady velocity field with a magnitude of  $u_0 = 1$  m s<sup>-1</sup> and a Courant number  $C_l = 0.1$ , so that the time step size is given by  $\Delta t = C_l \Delta l / u_0$ . The velocity field is given by  $\mathbf{u}_0 = u_0 \cos \theta \mathbf{e}_x + u_0 \sin \theta \mathbf{e}_y$ , and the tracer field is advected for a total time of 50,000 s.

The domain is initialized with a Gaussian passive tracer field at  $t = 0$  of the form

$$s(x, y, t = 0) = \exp \left[ -\frac{(x - x_0)^2}{2R^2} - \frac{(y - y_0)^2}{2R^2} \right], \quad (4.86)$$

where  $x_0 = 20$  km,  $y_0 = 20$  km, and  $R = 5$  km. We compute advection of the passive tracer on three different grids consisting of equilateral triangles with side lengths given

by  $\Delta l = 2000$  m,  $\Delta l = 1000$  m, and  $\Delta l = 500$  m using first-order upwind and the second-order scheme with  $\psi = 1.5$ . For each grid, advection is computed with the flow aligned at an angle  $\theta = m\pi/12$ ,  $m = 0, 1, 2, 3, 4$ , with respect to the grid.

## Results

The numerical diffusion and dispersion coefficients are highly sensitive to the direction of flow (Eqs. 4.46, 4.74 and 4.75). The coefficients are periodic in the interval  $\theta = [0, \pi/3]$ , since when the grid becomes aligned with the flow, i.e.,  $\theta = 0$  and  $\pi/3$  there are no fluxes through faces, and numerical diffusion and dispersion only exist in the streamwise direction parallel to the flow. We present two cases in our numerical simulations, namely  $\theta = 0$  which has anisotropic diffusion, and  $\theta = \pi/6$  which has approximately isotropic diffusion.

The Gaussian passive tracer field advected with first-order upwind and the second-order scheme after a total time of 50,000 s is shown in Fig. 4.6 for the mesh with  $\Delta l = 2000$  m (the coarse grid is shown to accentuate the errors). The exact solution is obtained by translating the initial tracer field and shown in black for comparison. First-order upwinding shows greater streamwise compared to lateral diffusion when  $\theta = 0$ , and we observe  $d_1 > d_2$ . This is evident from Eq. (4.46) which shows  $d_1 = k_{xx} \neq 0$  and  $d_2 = k_{yy} = 0$  when  $\theta = 0$ . A larger amount of diffusion is obtained when  $\theta = \pi/6$  compared to  $\theta = 0$ , since the maximum contour is 0.25 when  $\theta = \pi/6$ , and the maximum contour is 0.5 when  $\theta = 0$ . For the case that  $\theta = \pi/6$ , the diffusion is nearly isotropic, i.e.  $d_1 \approx d_2$ . The second-order scheme introduces less numerical diffusion than first-order upwinding, and for both  $\theta = 0$  and  $\pi/6$  the maximum contours are 0.75. Negative contours are observed for the second-order scheme which is expected since the Lax-Wendroff scheme produces oscillations due to the numerical dispersion. For the case that  $\theta = \pi/6$ , greater numerical dispersion is obtained compared to  $\theta = 0$  (indicated by the negative contours) and this explains the slightly distorted numerical solution with  $\theta = \pi/6$ .

Fig. 4.7 compares nondimensional analytical diffusion coefficients to those computed from idealized simulations as a function of  $\theta$ . The results show that the combined analysis produces the correct diffusion coefficients although the independent

analysis does not. For first-order upwinding, the streamwise diffusion coefficients are consistently overpredicted using the independent analysis. The lateral coefficients are overpredicted using the independent analysis except when  $\theta = \pi/6$ , and the magnitudes of the cross-diffusion coefficients are underpredicted using the independent analysis with the exception of  $\theta = 0, \pi/6$  and  $\pi/3$ . For the second-order scheme, the magnitudes of the streamwise, lateral and cross-diffusion are overpredicted with the independent analysis except when  $\theta = 0, \pi/6$  and  $\pi/3$ , which produces the correct diffusion coefficients using both methods.

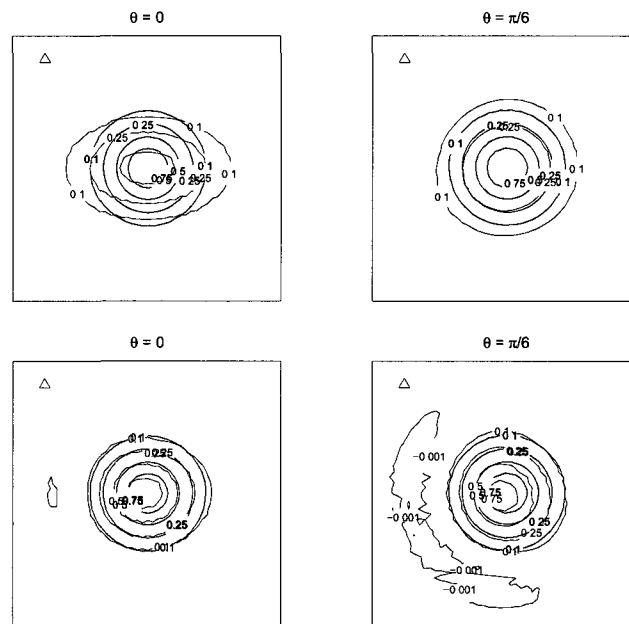


Figure 4.6: Result of advecting a Gaussian passive tracer field using first-order upwind (top row) and the second-order scheme (bottom row) on the grid with  $\Delta x = 2000$  m. The results are shown after 50,000 s for  $\theta = 0$  and  $\theta = \pi/6$ . The grid cell size is represented by a small triangle on the top left hand corner of the plots. Legend: Numerical solution (black), Exact solution (red).

As the method of spatial moments analysis cannot be employed to compute numerical dispersion coefficients from idealized simulations, the dispersion coefficients in Eq. (4.75) are verified by comparing results from idealized simulations on unstructured grids to those obtained with a pseudospectral method. The pseudospectral

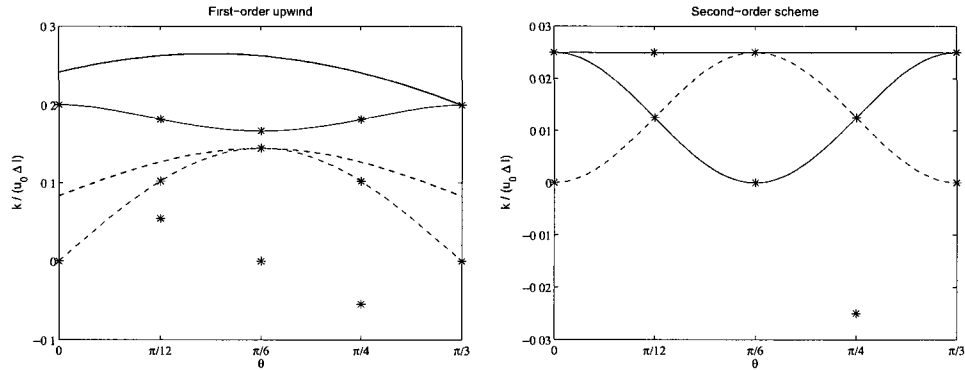


Figure 4.7: Comparison of theoretical diffusion coefficients to those computed using first-order upwind and the second-order scheme on the grid with  $\Delta l = 500$  m. Legend: Analytical  $k_{xx}$  (—),  $k_{yy}$  (---),  $k_{xy}$  (···), Idealized simulations using spatial moments analysis (\*), Independent analysis (red), and Combined analysis (black).

method (Kosloff et al. 1984; Reshef et al. 1988) is a highly accurate numerical modeling technique that computes the spatial derivatives by means of the Fast Fourier Transform (FFT). The time advancement is performed with the Runge-Kutta method (RK4) (Runge 1895; Kutta 1901), which leads to an essentially “exact” solution of the partial differential equation. The pseudospectral method solves the following partial differential equation on Cartesian grids,

$$\begin{aligned} \frac{\partial s}{\partial t} + \mathbf{u} \cdot \nabla s = & k_{xx,s} \frac{\partial^2 s}{\partial x^2} + k_{yy,s} \frac{\partial^2 s}{\partial y^2} + k_{xy,s} \frac{\partial^2 s}{\partial x \partial y} + k_{xxx,s} \frac{\partial^3 s}{\partial y^3} + k_{yyy,s} \frac{\partial^3 s}{\partial y^3} \\ & + k_{xxy,s} \frac{\partial^3 s}{\partial x^2 \partial y} + k_{xyy,s} \frac{\partial^3 s}{\partial y^2 \partial x}, \end{aligned} \quad (4.87)$$

where the diffusion and dispersion coefficients are aligned with the Cartesian grid and not with the flow direction. These coefficients are obtained by rotating the flow-aligned coefficients in Eqs. (4.74) and (4.75) to a Cartesian coordinate system by the angle  $-\theta$ .

The results from our unstructured-grid simulations are compared to those obtained from the pseudospectral method by advecting a Gaussian passive tracer field with the second-order scheme. The unstructured-grid simulations employ a grid with side



given by

$$E = \frac{[\sum_i (s_2 - s_1)^2]^{1/2}}{[\sum_i (s_1)^2]^{1/2}}. \quad (4.88)$$

For the spatial analysis,  $s_2$  is the tracer field at a given time and  $s_1$  is the exact tracer field, which is obtained simply by translating the original tracer field after the given time in the absence of diffusion. Comparison to the exact solution eliminates the necessity of unstructured-grid interpolation. For the temporal analysis,  $s_1$  is the tracer field computed with a time step of  $\Delta t$  and  $s_2$  is the tracer field computed with a time step of  $\Delta t/2$ .

The accuracy analysis is performed for first-order upwind and the second-order scheme with  $\psi = 1.5$  after running the simulation for 50,000 s. For the spatial analysis, the tracer field is advected on three different grids consisting of equilateral triangles with side lengths given by  $\Delta l = 4000$  m,  $\Delta l = 2000$  m and  $\Delta l = 1000$  m. The steady velocity field has a magnitude  $u_0 = 1$  m s<sup>-1</sup>, and we use a time step of  $\Delta t = 100$  s. For the temporal analysis, the tracer field is advected on a fine mesh with the side length given by  $\Delta l = 500$  m, using time steps of  $\Delta t = 200$  s,  $\Delta t = 100$  s,  $\Delta t = 50$  s and  $\Delta t = 25$  s.

Fig. 4.9 shows accuracy in time and space using first-order upwind and the second-order scheme. As expected, first-order upwinding is first-order accurate in time and space, while the second-order scheme is second-order accurate in time and space. The second-order scheme is more effective in reducing errors compared to first-order upwinding, and smaller errors are obtained with  $\theta = 0$  compared to  $\theta = \pi/6$ . This is evident from Fig. 4.7 which shows numerical diffusion coefficients are one order of magnitude smaller for the second-order scheme compared to first-order upwinding, and Fig. 4.6 which shows  $\theta = 0$  is less diffusive than  $\theta = \pi/6$ .

## 4.4 Summary and discussion

The quantification of numerical diffusion from scalar transport is employed to assess the performance of first-order upwind and second-order scalar advection schemes on unstructured grids. A novel approach is proposed to analytically derive numerical

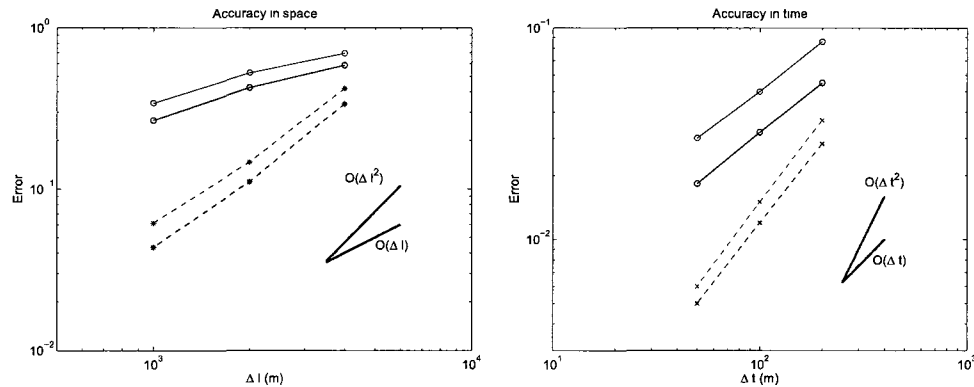


Figure 4.9: Accuracy in space and time for  $\theta = 0$  and  $\theta = \pi/6$ . Legend:  $\theta = 0$  (red),  $\theta = \pi/6$  (black), first-order upwind ( $—, \circ$ ), second-order scheme ( $---, *$ ).

diffusion coefficients by extending the Hirt analysis (Hirt 1968) on Cartesian grids to unstructured grids. We assume uniform flow on a grid composed of equilateral triangles in the derivation of analytical numerical diffusion coefficients.

Two methods, termed the independent analysis and combined analysis are applied to compute the modified form of the advection equation. The independent analysis separately derives the modified equations for the two types of cells, and this method leads to an overprediction of numerical diffusion coefficients. The combined analysis uses a recurrence relation to derive the equation for one cell, and Holleman et al. (2011) show the combined analysis obtains the correct diffusion coefficients for first-order upwinding. We extend this method to derive diffusion coefficients for the second-order scheme, and show that these match coefficients obtained from idealized simulations. The second-order scheme is based on the Lax-Wendroff scheme on Cartesian grids which stabilizes central differencing but introduces numerical dispersion.

The numerical diffusion and dispersion coefficients on unstructured grids are compared to those on two-dimensional Cartesian grids. In this discussion, we refer to the diffusion and dispersion coefficients on Cartesian grids as  $d^{2d}$  and  $k^{2d}$  respectively. Fig. 4.10 shows nondimensional  $d_1$  and  $d_2$  from the diffusion tensor as a function of  $\theta$  with  $C_0 = 0.1$  on Cartesian and unstructured grids. The figure shows that numerical diffusion is comparable on two-dimensional Cartesian grids and unstructured grids.

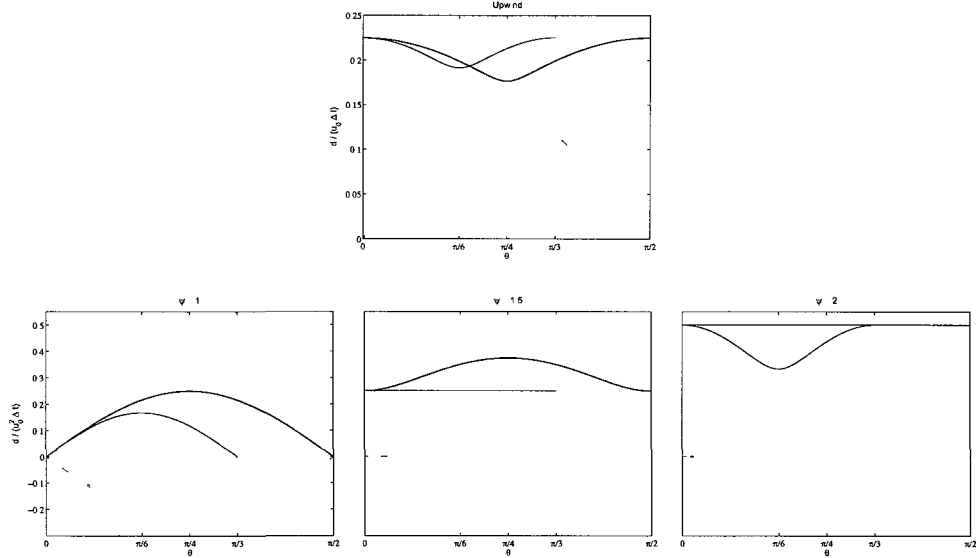


Figure 4.10: Nondimensional  $d_1$  and  $d_2$  from the diffusion tensor as a function of  $\theta$  with  $C_0 = 0.1$  for first-order upwind and the second-order scheme from the combined analysis. First-order upwind is nondimensionalized with  $(u_0\Delta l)$  and the second-order scheme is nondimensionalized with  $(u_0^2\Delta t)$ . First row is first-order upwind and second row is the second-order scheme, with  $\psi = 1, 1.5$  and  $2$ . Legend:  $d_1$  (—) and  $d_2$  (---), black (unstructured grids), red (two-dimensional Cartesian grids).

For both high- and low-order schemes,  $d_1^{2d} = d_1$  and  $d_2^{2d} = d_2$  when one of the edges is aligned with the flow. For first-order upwinding, the ratios of  $\min(d_1^{2d}) : \min(d_1)$  and  $\max(d_2^{2d}) : \max(d_2)$  are respectively 0.92 and 1.04. The second-order scheme with  $\psi = 1$  is unstable on both Cartesian and unstructured grids except when one of the edges is aligned with the flow since  $d_2 < 0$ . The minimum  $\psi$  that results in a stable scheme on unstructured and Cartesian grids are respectively  $\psi = 1.5$  and  $\psi = 2$ . Setting the minimum  $\psi$  for stability on both grids lead to the ratio  $d_1^{2d} : d_1 = 2.5$ , as we require a larger  $\psi$  for stability on Cartesian grids.

Fig. 4.11 shows the nondimensional dispersion coefficients as a function of  $\theta$  for the second-order scheme from the combined analysis with  $C_0 = 0$  on Cartesian and unstructured grids. The figure shows that numerical dispersion is comparable on unstructured and two-dimensional Cartesian grids. The dispersion coefficients are identical on unstructured and Cartesian grids when one of the edges is aligned with



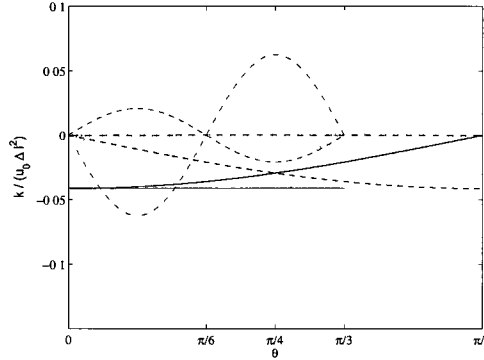


Figure 4.11: Nondimensional dispersion coefficients as a function of  $\theta$  with  $C_0 = 0.1$  for the second-order scheme from the combined analysis. Legend:  $k_{xxx}/(u_0\Delta t^2)$  (—),  $k_{yyy}/(u_0\Delta t^2)$  (---),  $k_{xxy}/(u_0\Delta t^2)$  (- · -),  $k_{xyy}/(u_0\Delta t^2)$  (···), black (unstructured grids), red (two-dimensional Cartesian grids).

the flow as  $k_{xxx}^{2d}/(u_0\Delta t^2) = k_{xxx}/(u_0\Delta t^2) = -0.04$  and the remaining terms vanish. The maximum differences in the dispersion coefficients occur when  $\theta = \pi/6$  on unstructured grids and  $\theta = \pi/4$  on Cartesian grids, which results in the cross-dispersion terms  $k_{xxy}/(u_0\Delta t^2) = 0$  and  $k_{xyy}/(u_0\Delta t^2) = -0.125$  on unstructured grids while  $k_{xxy}^{2d}/(u_0\Delta t^2) = -0.03$  and  $k_{xyy}^{2d}/(u_0\Delta t^2) = 0$  on Cartesian grids. For this choice of  $\theta$ , the remaining terms are comparable on both grids with the ratio  $k_{xxx}^{2d}/(u_0\Delta t^2) : k_{xxx}/(u_0\Delta t^2) = 1.33$  and  $k_{xxy}^{2d}/(u_0\Delta t^2) = k_{xyy}/(u_0\Delta t^2) = 0$ .

A stability analysis is performed for first-order upwinding and the second-order scheme on unstructured and two-dimensional Cartesian grids. The first-order upwind scheme is most restrictive on unstructured grids when  $\theta = \pi/6$  which requires that  $0 \leq C_0 \leq \sqrt{3}/2 \approx 0.87$ . In comparison, the constraint is stricter on Cartesian grids, and the most restrictive Courant number occurs when  $\theta = \pi/4$ , which requires that  $0 \leq C_0 \leq 1/\sqrt{2} \approx 0.71$ . The second-order scheme is stable on unstructured grids with  $\psi \geq 1.5$  and  $0 \leq C_0 \leq 1/\sqrt{6} \approx 0.82$  for all  $\theta$ . In comparison, on Cartesian grids the second-order scheme has stricter conditions for stability with  $\psi \geq 2$  and  $0 \leq C_0 \leq 1/\sqrt{2} \approx 0.71$  for all  $\theta$ .

The accuracy analysis shows that first-order upwinding is first-order accurate in time and space while the second-order scheme is second-order accurate in time and

space. Although the truncation errors of the modified equation are formally first-order for the second-order scheme, the truncation errors are small and the method is effectively second-order accurate in time and space as shown by the accuracy analysis.

# Chapter 5

## Numerical diffusion in San Francisco Bay

### 5.1 Introduction

In this chapter, we introduce a domain-averaged formulation to estimate numerical diffusion coefficients under general flow and triangulation conditions, which provides an estimate for numerical diffusion without the need for analytical methods like the Hirt (Hirt 1968) analysis in Chapter 4. The ability of the domain-averaged formulation to infer diffusion coefficients are verified with idealized simulations. This formulation is particularly suited to compare the performance of high- and low- order scalar advection schemes for applications in complex geometries, and is applied to San Francisco Bay to assess the impact of tidal dispersion and different time scales on the numerical diffusion.

#### 5.1.1 Inferring the diffusion coefficient for general discretizations

The diffusion coefficients derived in Chapter 4 made numerous assumptions about the flow and the triangulation. Under more general flow and triangulation conditions, it is not possible to derive a general form of the diffusion coefficient. In addition,

higher-order advection schemes make the task of analytically deriving the form of the numerical diffusion coefficient extremely difficult if not impossible. Therefore, in this chapter we propose a method to estimate the numerical diffusion without the need for analytical methods like the Hirt (Hirt 1968) analysis in Chapter 4.

Our method of estimating the numerical diffusion coefficient is based on the work of Burchard and Rennau (2007) (hereafter BR07), who developed a method to compute the numerically-induced mixing of a passive tracer at time level  $n$ ,  $s^n$ , with

$$D_{\text{num}}(s^n)^2 = \frac{A[(s^n)^2] - [A(s^n)]^2}{\Delta t}, \quad (5.1)$$

where  $A(s^n) = s^n - \Delta t \text{Adv}^d(s^n)$ , and  $\text{Adv}^d$  is the discrete advection operator. Expression (5.1) is derived from Eq. (18) in BR07, which can be written more generally in its three-dimensional form as

$$\frac{(s^{n+1})^2 - A[(s^n)^2]}{\Delta t} = -2k_{\text{num}} \nabla^d s^n \cdot \nabla^d s^n, \quad (5.2)$$

where  $\nabla^d$  is the discrete gradient operator and  $k_{\text{num}}$  is the effective isotropic numerical diffusion coefficient. BR07 show that, for the FTBS discretization given in Eq. (4.2), the squared-gradient operator at a given cell  $i$  is  $\nabla^d s_i^n \cdot \nabla^d s_i^n = (s_i^n - s_{i-1}^n)^2 / \Delta x^2$  and  $k_{\text{num}} = k_{\text{num},1d}$  given in Eq. (4.4). For more general advection schemes in higher dimensions, we assume that the modified PDE of the advection equation incurs isotropic diffusion of the form

$$k_{\text{num}} \nabla^d \cdot \nabla^d s. \quad (5.3)$$

Errors in computing an effective isotropic numerical diffusion coefficient will arise primarily from the assumption of isotropy. In reality, the numerical diffusion is anisotropic as shown in Eqs. (4.46) and (4.74). Therefore, we emphasize that  $k_{\text{num}}$  is an approximate measure of the numerical diffusion. It is representative of the actual numerical diffusion in idealized test cases using uniform equilateral triangles only when the flow is at an angle of  $\pi/6$  relative to the grid.

Eq. (5.2) can be rearranged to give

$$\frac{(s^{n+1})^2 - (s^n)^2}{\Delta t} + \text{Adv}^d((s^n)^2) = -2k_{\text{num}} \nabla^d s^n \cdot \nabla^d s^n, \quad (5.4)$$

which is a discrete approximation to the continuous tracer variance equation

$$\frac{\partial s^2}{\partial t} + \mathbf{u} \cdot \nabla(s^2) = 0. \quad (5.5)$$

As pointed out by BR07, transport of the tracer variance in its continuous sense is conservative, while discrete transport, in general, is not. Discrete conservation of tracer variance can be ensured with second-order moments (SOM) methods (Prather 1986), although in general SOM methods do not ensure monotonicity. Monotonicity-preservation occurs at the expense of a non-conservative error in the conservation of tracer variance Eq. (5.4). The right-hand side of Eq. (5.4) represents the leading error that results from the numerically-diffusive (or anti-diffusive) nature of the advection scheme.

As outlined in BR07, it is possible to compute the local numerical mixing. This then allows computation of local numerical diffusion coefficients by combining Eqs. (5.1) and (5.2) to yield

$$k_{\text{num,local}} = \frac{D_{\text{num}}(s^n)^2}{2\nabla^d s^n \cdot \nabla^d s^n}. \quad (5.6)$$

This allows us to compute  $k_{\text{num,local}}$  at each grid cell with  $\nabla^d s^n \cdot \nabla^d s^n = [(\partial s / \partial x)^2 + (\partial s / \partial y)^2]$ . Rather than analyze the local properties of the numerical diffusion coefficient, we assume a constant numerical diffusion coefficient and define the global numerical diffusion coefficient via a domain integration of Eq. (5.4) to yield

$$k_{\text{num}} = \frac{\sum [(s^n)^2 - (s^{n+1})^2] \Delta V}{2\Delta t \sum \nabla^d s^n \cdot \nabla^d s^n \Delta V}, \quad (5.7)$$

where  $\sum$  implies summation over the entire domain which consists of control volumes of size  $\Delta V$ , and we assume that the discrete advection operator is locally conservative so that its domain-integration vanishes upon assuming that the tracer concentration on the boundaries is zero. This form of computing a global measure of the numerical

diffusion is more straightforward than domain-averaging Eq. (5.6) because it eliminates the need to compute  $A[(s^n)^2]$ .

We can assess the accuracy of Eq. (5.7) in computing the domain-averaged numerical diffusion coefficient by computing advection of a passive tracer under the influence of a fixed physical diffusion coefficient,  $k_{\text{phys}}$ . If we assume that the presence of physical diffusion leads to reduction of tracer variance in Eq. (5.4) approximately of the form  $-2k_{\text{phys}}\nabla^d s^n \cdot \nabla^d s^n$ , then Eq. (5.7) would give a net diffusion coefficient of

$$k_{\text{net}} = k_{\text{num}} + k_{\text{phys}} = \frac{\sum [(s^n)^2 - (s^{n+1})^2] \Delta V}{2\Delta t \sum \nabla^d s^n \cdot \nabla^d s^n \Delta V}. \quad (5.8)$$

Evaluation of the right-hand side of Eq. (5.8) will then give the net sum of the domain-integrated numerical and physical diffusion. Therefore, if the physical diffusion is large, then  $k_{\text{net}}$  should approximate the physical diffusion.

## 5.2 Numerical simulations

### 5.2.1 Idealized simulations

We initialize a rectangular domain of length  $L = 100$  km and width  $W = 100$  km with a Gaussian passive tracer field of the form

$$s(x, y, t = 0) = \exp \left[ -\frac{(x - x_0)^2}{2R^2} - \frac{(y - y_0)^2}{2R^2} \right], \quad (5.9)$$

where  $x_0 = 20$  km,  $y_0 = 20$  km, and  $R = 5$  km. The passive tracer is advected in the absence of physical diffusion on grids (A)  $\Delta l = 2000$  m, (B)  $\Delta l = 1000$  m, and (C)  $\Delta l = 500$  m using first-order upwind and the same TVD scheme that is used for salinity simulations in Chapter 2. The tracer field is advected in a steady velocity field with a magnitude of  $u_0 = 1$  m s<sup>-1</sup> and a Courant number  $C = 0.1$ , so that the time step size is given by  $\Delta t = C\Delta l/u_0$ , and the tracer field is advected for a total time of 50,000 s.

We compute  $k_{\text{net}}$  using the domain-averaged formulation in Eq. (5.7). Since grid

(C) should have the lowest numerical diffusion, we use this grid to compute two more cases with increasing amounts of physical diffusion to test the ability of the domain-averaged formulation to infer this physical diffusion, namely runs (D)  $k_{\text{phys}} = 50 \text{ m}^2 \text{ s}^{-1}$  and (E)  $k_{\text{phys}} = 200 \text{ m}^2 \text{ s}^{-1}$ . These results are summarized in Table 5.1.

Fig. 5.1 depicts the result of advecting the initial tracer field with different amounts of physical diffusion (runs C - E). In the absence of physical diffusion, the numerical diffusion coefficients for first-order upwind and second-order schemes are derived in Chapter 4. For the case that  $\theta = 0$ , numerical diffusion exists only in the streamwise direction, while the lateral and cross-diffusion terms are zero. Even though physical diffusion acts equally in all directions, the net diffusion is anisotropic because numerical diffusion is in the streamwise direction. As expected, first-order upwinding leads to higher diffusion and stronger spreading in the streamwise direction compared to the TVD scheme. Time series of  $k_{\text{net}}$  for cases C-E are depicted in Fig. 5.2. For all cases  $k_{\text{net}}$  is large upon initiation because the tracer field experiences dominant numerical diffusion at the start. After a few time steps, the smoothing of fronts lead to a decrease in the amount of numerical diffusion the tracer field experiences, and  $k_{\text{net}}$  decays until it reaches a quasi steady-state.

Upon reaching quasi-equilibrium,  $k_{\text{net}}$  is used to assess the numerical diffusion (Table 5.1). These results show that the numerical diffusion for the TVD scheme is consistently lower than that for first-order upwinding. Similar amounts of numerical diffusion are predicted for runs C - E, indicating  $k_{\text{net}}$  accurately infers the added physical diffusion. The numerical diffusion coefficient scales with grid spacing for the high- and low- order schemes, i.e, for first-order upwinding  $k_{\text{num}}/u_0\Delta l \sim 0.13$  and for the TVD scheme  $k_{\text{num}}/u_0\Delta l \sim 0.01$ . The coefficient of proportionality is one order of magnitude smaller for the TVD scheme compared to first-order upwinding, which is consistent with results in Chapter 4. The analytical numerical diffusion coefficients when  $\theta = 0$  for  $k_{xx}/u_0\Delta l$  using first-order upwind and the second-order scheme with  $\psi = 1.5$  are respectively 0.2 and 0.025.  $k_{\text{num}}/u_0\Delta l$  assumes isotropy which results in underprediction of the numerical diffusion coefficients. In reality numerical diffusion is anisotropic for the case that  $\theta = 0$ , and numerical diffusion exists only in the streamwise direction.

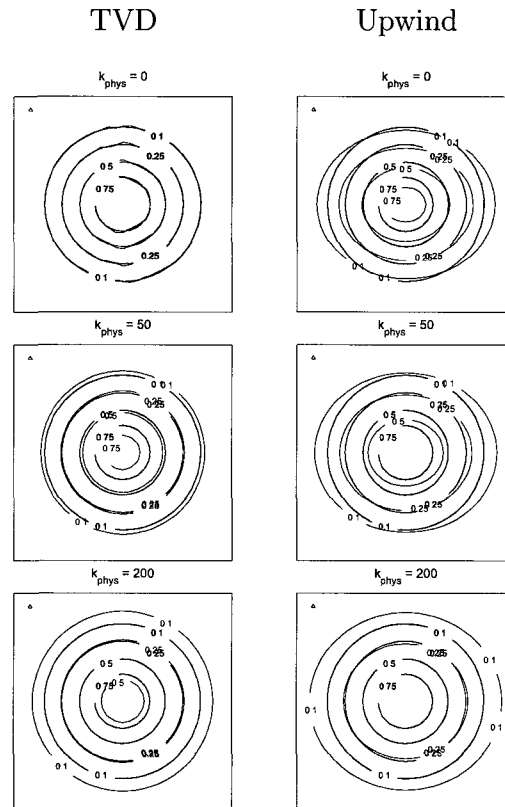


Figure 5.1: Result of advecting a Gaussian passive tracer after 50,000 s with the TVD scheme (left column) and first-order upwind (right column). The three rows represent results with  $k_{\text{phys}} = 0 \text{ m}^2 \text{ s}^{-1}$  (run C),  $k_{\text{phys}} = 50 \text{ m}^2 \text{ s}^{-1}$  (run D) and  $k_{\text{phys}} = 200 \text{ m}^2 \text{ s}^{-1}$  (run E). The grid cell size is represented by a small triangle on the top left hand corner of the plot. Legend: Numerical solution (black), Exact solution (red).



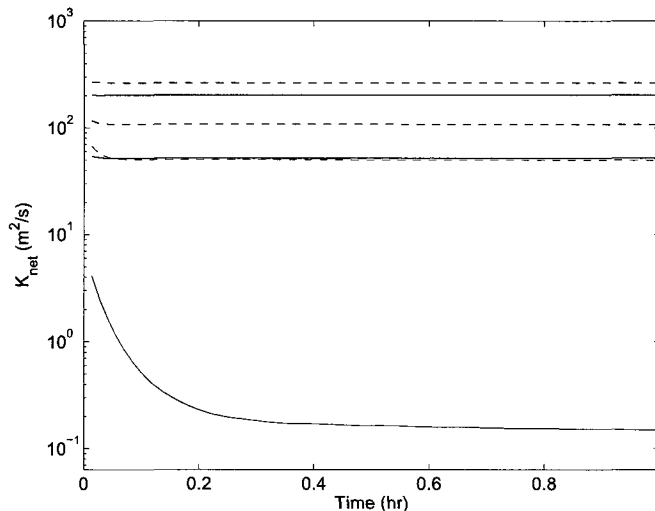


Figure 5.2: Comparison of  $k_{\text{net}}$  with different amounts of physical diffusion. Legend: first-order upwind (---), TVD (—),  $k_{\text{phys}} = 0 \text{ m}^2 \text{ s}^{-1}$  (black),  $k_{\text{phys}} = 50 \text{ m}^2 \text{ s}^{-1}$  (red),  $k_{\text{phys}} = 200 \text{ m}^2 \text{ s}^{-1}$  (blue).

Fig. 5.3 shows the sensitivity of  $k_{\text{net}}$  and  $k_{\text{xx}}$  to grid resolution. For first-order upwinding, numerical diffusion grows to first-order in the grid spacing, and both  $k_{\text{net}}$  and  $k_{\text{xx}}$  converges with first-order accuracy. Eq. (4.46) shows analytical  $k_{\text{xx}}$  is proportional to  $\Delta l$ . On one-dimensional grids the TVD scheme has numerical diffusion that is second-order accurate. The TVD scheme is nonlinear in the advected quantity, and hence on unstructured grids this method obtains  $k_{\text{net}}$  that grows to 1.5-order in grid spacing. For comparison, the second-order scheme with constant  $\psi$  has  $k_{\text{xx}}$  which converges with first-order accuracy as shown in Eq. (4.74).

Following the method outlined in Burchard and Rennau (2007), we obtain local numerical diffusion coefficients from the same set of numerical simulations, by computing  $k_{\text{num,local}}$  with Eq. (5.6). The statistical properties (mean, max, min, std) of  $k_{\text{num,local}}$  are summarized in Table 5.2 and compared to the domain-averaged formulation.  $k_{\text{num,local}}$  is representative of the independent analysis since the tracer moves from type A to type B cells (following the notation in Chapter 4) as it is advected in the domain, and the numerical diffusion coefficients oscillate widely for the two types of cells. This leads to high standard deviation in the statistical properties for

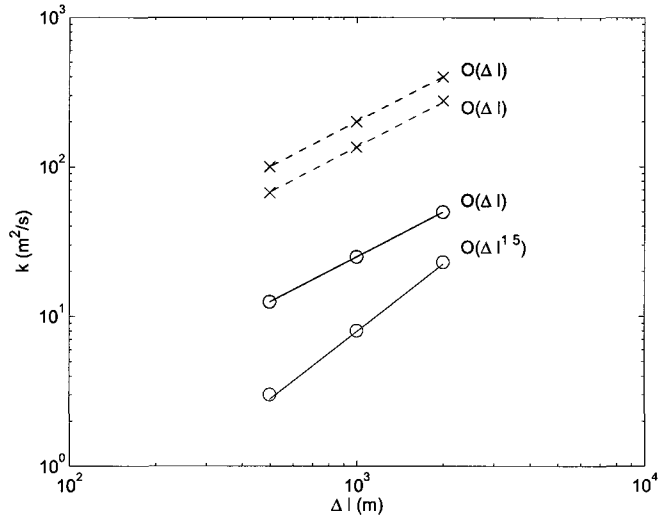


Figure 5.3: Sensitivity of  $k_{\text{net}}$  to grid resolution. Legend:  $k_{\text{net}}$  (black),  $k_{\text{xx}}$  (red), First-order upwind (x,--), Second-order (o,—).

Table 5.1: Channel flow numerical simulations with the addition of physical diffusion.  $k_{\text{xx}}$  derived in Chapter 4 for the case that  $\theta = 0$  is shown for comparison.  $k_{\text{yy}} = k_{\text{xy}} = 0$  when  $\theta = 0$ . Diffusion coefficients are in  $\text{m}^2 \text{s}^{-1}$ .  $k_{\text{num}} = k_{\text{net}} - k_{\text{phys}}$ .

| Case | $\Delta x$ (m) | $k_{\text{phys}}$ | $k_{\text{net}}$ |     | $k_{\text{num}}$ |     | $k_{\text{num}}/u_0\Delta l$ |       | $k_{\text{xx}}/u_0\Delta l$ |              |
|------|----------------|-------------------|------------------|-----|------------------|-----|------------------------------|-------|-----------------------------|--------------|
|      |                |                   | Upwind           | TVD | Upwind           | TVD | Upwind                       | TVD   | Upwind                      | $\psi = 1.5$ |
| A    | 2000           | 0                 | 277              | 20  | 277              | 16  | 0.13                         | 0.010 | 0.2                         | 0.025        |
| B    | 1000           | 0                 | 135              | 8   | 135              | 8   | 0.13                         | 0.008 | 0.2                         | 0.025        |
| C    | 500            | 0                 | 67               | 4   | 67               | 4   | 0.13                         | 0.008 | 0.2                         | 0.025        |
| D    | 500            | 50                | 117              | 54  | 67               | 4   | 0.13                         | 0.008 | -                           | -            |
| E    | 500            | 200               | 267              | 204 | 67               | 4   | 0.13                         | 0.008 | -                           | -            |

Table 5.2: Comparisons of  $k_{\text{net}}$  and  $k_{\text{num,local}}$  from channel flow numerical simulations. Diffusion coefficients are in  $\text{m}^2 \text{s}^{-1}$ .

| Run | $\Delta x$ (m) | Upwind           |                        |      |     | TVD              |                        |      |      |       |     |
|-----|----------------|------------------|------------------------|------|-----|------------------|------------------------|------|------|-------|-----|
|     |                | $k_{\text{net}}$ | $k_{\text{num,local}}$ |      |     | $k_{\text{net}}$ | $k_{\text{num,local}}$ |      |      |       |     |
|     |                |                  | mean                   | max  | min | std              |                        | mean | max  | min   | std |
| A   | 2000           | 277              | 255                    | 4205 | 0   | 363              | 23                     | 47   | 4342 | -4557 | 491 |
| B   | 1000           | 135              | 134                    | 1998 | 0   | 140              | 8                      | 8    | 814  | -794  | 165 |
| C   | 500            | 67               | 67                     | 967  | 0   | 58               | 4                      | 2    | 849  | -988  | 71  |

$k_{\text{num,local}}$ . On the other hand, the combined analysis which employs a recurrence relation to derive one equation takes into account the effects of one type of cell on the other and computes numerical diffusion in an averaged sense along the path the tracer field is advected. This is analogous to the domain-averaged formulation  $k_{\text{net}}$  which provides a better estimate of numerical diffusion than  $k_{\text{num,local}}$  computed at each grid cell.

### 5.2.2 Numerical diffusion in San Francisco Bay

We employ the unstructured-grid SUNTANS model to perform three-dimensional simulations of flow in San Francisco Bay. The setup and implementation of the SUNTANS model applied to San Francisco Bay, and details of the calibration and validation are presented in Chapter 2. To assess the effects of tidal dispersion and time scales on numerical diffusion, we analyze the dynamics of a passive tracer field advected with first-order upwind and the TVD scheme.

The domain is initialized with a passive tracer field at three different locations throughout the Bay, namely (A) Golden Gate, (B) Carquinez Strait, (C) South Bay Shoals (see Fig. 2.1). The passive tracer has radius  $R = 1$  km and is constant over the depth. The tracer field is initialized on 4 February 2005 at the beginning of the flood

tide (recall that the model is calibrated during the period 1 January to 14 February 2005), and the resulting tracer field is analyzed over the subsequent three days.

### 5.3 Tidal dispersion

The flow dynamics at the three sites in San Francisco Bay are characterized by varying degrees of horizontal and vertical tidal dispersion. The tidal flow has a large influence on dispersion at regions with abrupt changes in bathymetry, through mechanisms such as shear dispersion, turbulence, tidal pumping and trapping and Lagrangian motions (Geyer and Signell 1992). Strong tidal currents are generated at the Golden Gate where strong currents lead to tidal pumping that results from a jet-sink asymmetry at the inlet (Stommel and Farmer 1952). This tidal pumping leads to strong tidal dispersion which is enhanced by the formation of transient eddies and flow separation (Signell and Geyer 2007). At Carquinez Strait, the longitudinal density gradient resulting from the salt wedge drives gravitational circulation in which flow is advected landward along the bottom and seaward at the surface, resulting in longitudinal dispersion of the passive tracer released at this location (Hansen and Rattray 1965; Monismith et al. 2002). The baroclinic circulation also induces transverse residual circulation resulting in lateral shear (Smith and Cheng 1987; Nunes and Simpson 1985). At South Bay Shoals where bathymetric variability is weak, tidal dispersion is negligible relative to that at Golden Gate and Carquinez Strait.

Figs. 5.4 - 5.9 show the evolution of the depth-averaged passive tracer field over the first 21 hours at the three sites, and compares the results of the TVD scheme to those with first-order upwinding. We also quantify the relative effects of tidal dispersion on the numerical diffusion in each of the three locations by computing  $k_{\text{net}}$  using Eq. (5.8). The mean  $k_{\text{net}}$  for the three-day period are tabulated in Table 5.3. Time series of  $k_{\text{net}}$  at each location, and comparisons of the TVD scheme to first-order upwinding are shown in Fig. 5.10. Since physical diffusion of the tracer field is ignored in these simulations,  $k_{\text{net}}$  should provide a direct measure of the numerical diffusion for each scheme.

The strong tidal dispersion at Golden Gate (Fig. 5.4) and Carquinez Strait (Fig. 5.6)

lead to substantial stirring of the tracer field that produces marked differences between first-order upwind and the TVD scheme for the first 12 hours. At both locations, the TVD scheme maintains the initial sharp fronts, while first-order upwinding has a tendency to smooth the fronts. However, after roughly 12 hours (Figs. 5.5 and 5.7) the differences between the high- and low- order schemes at both locations are reduced. This is shown by the time series of  $k_{\text{net}}$  in Fig. 5.10. Because the differences between first-order upwind and the TVD scheme are large only initially, the averaged values are roughly equal as shown in Table 5.3.

In the South Bay Shoals (Figs. 5.8 and 5.9), where tidal dispersion is weak, the differences between the high- and low- order schemes remain high throughout the period of simulation. The low velocities in the shoals lead to the tracer field remaining at roughly the initial location. The TVD scheme maintains the sharp fronts of the tracer, while first-order upwinding smooths the fronts by numerical diffusion.  $k_{\text{net}}$  shows a marked difference between the high- and low-order schemes for the period of simulation (Fig. 5.10), and is approximately a factor of three times smaller for the TVD scheme compared to first-order upwinding. As a consequence of the weak tidal dispersion, numerical diffusion is the main contributor to  $k_{\text{net}}$  in the shoals.

These results show that  $k_{\text{net}}$  is lower for the TVD scheme only in regions where tidal dispersion is relatively low. In regions of high tidal dispersion, strong stirring of the tracer field leads to grid-scale variability that produces equivalent  $k_{\text{net}}$  for both first-order upwinding and the TVD scheme after an initial smoothing period.

## 5.4 Diffusion coefficients evaluated over different time scales

We obtain similar  $k_{\text{net}}$  for the passive tracer field at Carquinez Straits with both first-order upwind and the TVD scheme after the initial smoothing period (Fig. 5.6), while a sensitivity analysis of salinity simulations at the location of Benicia in Carquinez Straits demonstrate a reduction in mean and RMS errors when employing the TVD scheme (Fig. 3.1). To investigate if the time scale over which the numerical diffusion is

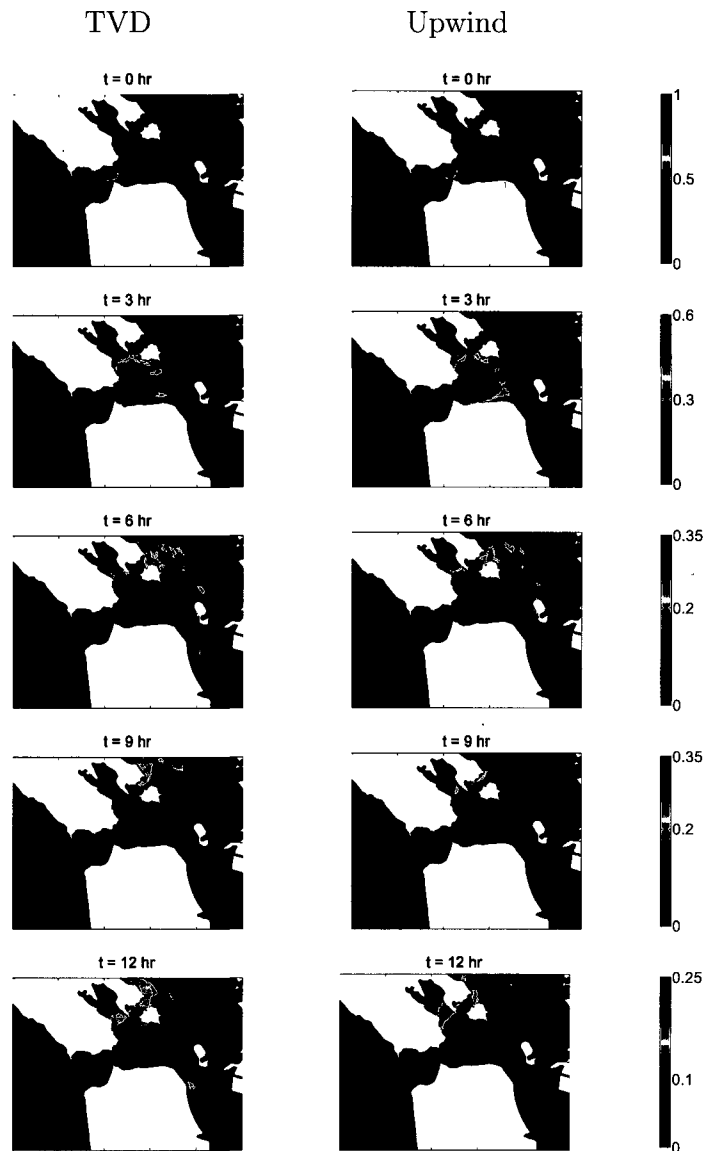


Figure 5.4: Evolution of passive tracer field at Golden Gate from 0 to 12 hour in 3 hour intervals. Left column is the TVD scheme and right column is first-order upwind. Note that the color axes change with time.

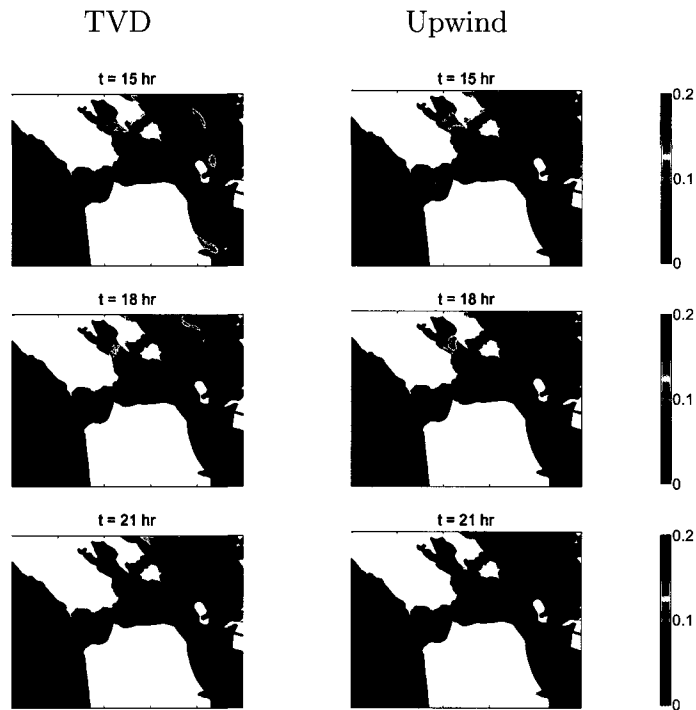


Figure 5.5: Evolution of passive tracer field at Golden Gate from 15 to 21 hour in 3 hour intervals. Left column is the TVD scheme and right column is first-order upwind. Note that the color axes change with time.

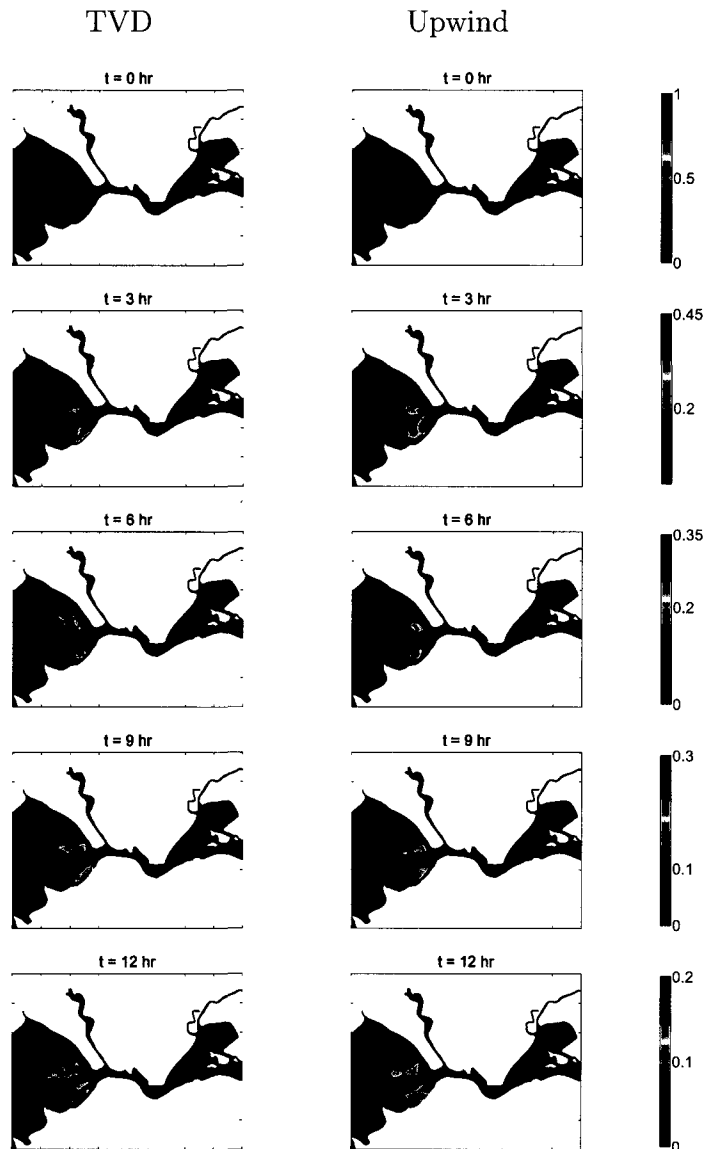


Figure 5.6: Evolution of passive tracer field at Carquinez Strait from 0 to 12 hour in 3 hour intervals. Left column is the TVD scheme, and right column is first-order upwind. Note that the color axes change with time.



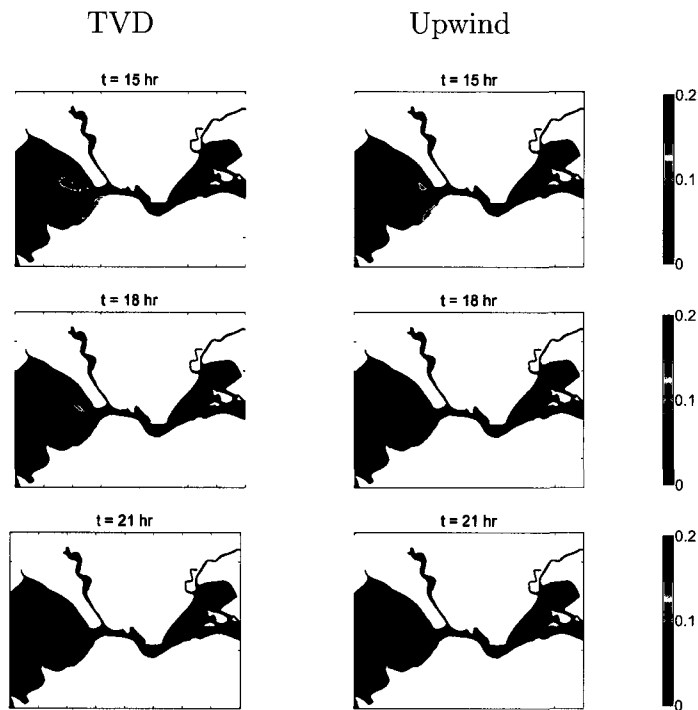


Figure 5.7: Evolution of passive tracer field at Carquinez Strait from 15 to 21 hour in 3 hour intervals. Left column is the TVD scheme, and right column is first-order upwind. Note that the color axes change with time.

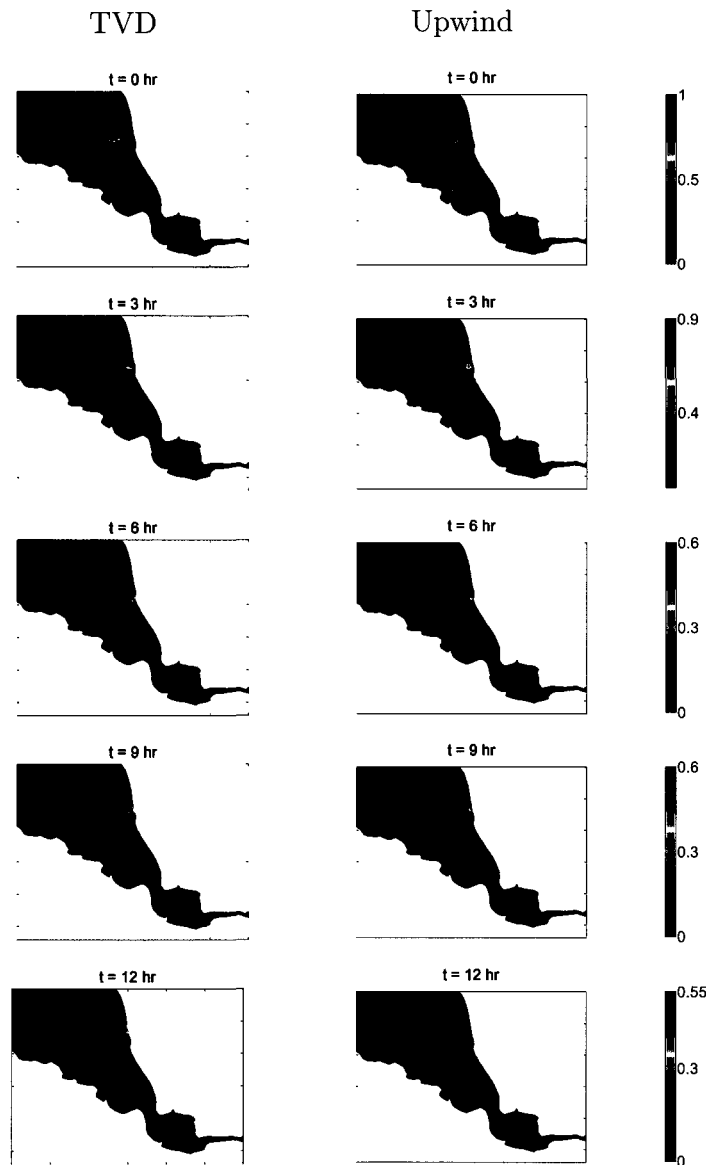


Figure 5.8: Evolution of passive tracer field in South Bay from 0 to 12 hour in 3 hour intervals. Left column is the TVD scheme, and right column is first-order upwind. Note that the color axes change with time.

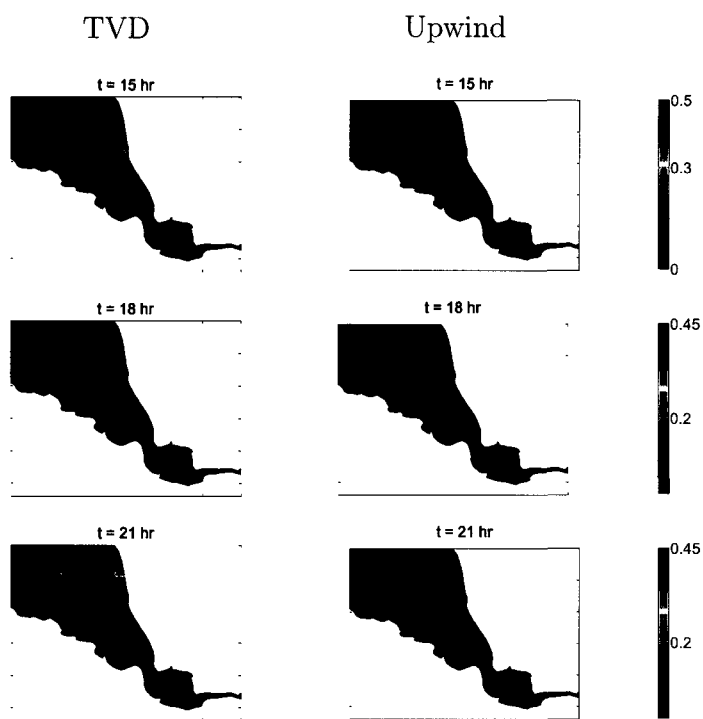


Figure 5.9: Evolution of passive tracer field in South Bay from 15 to 21 hour in 3 hour intervals. Left column is the TVD scheme, and right column is first-order upwind. Note that the color axes change with time.

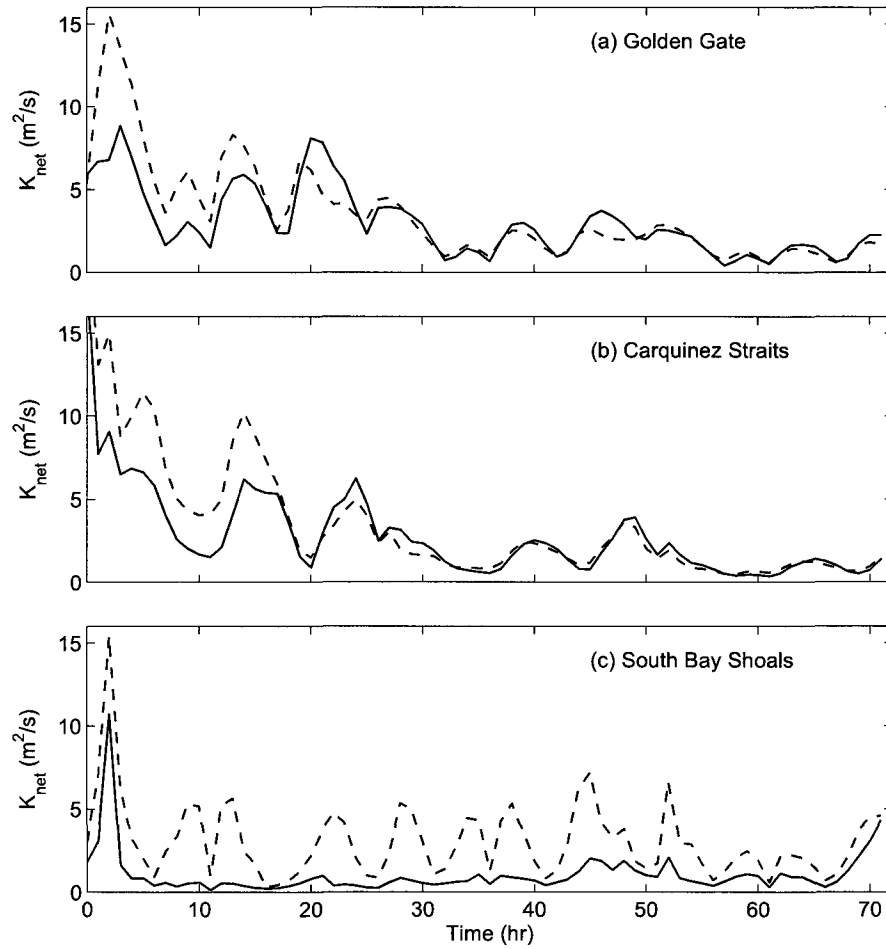


Figure 5.10: Comparison of  $k_{\text{net}}$  for the period of simulation at (a) Golden Gate (b) Carquinez Straits (c) South Bay Shoals. Legend: first-order upwind (---), TVD (—).

computed might contribute to the performance of the advection schemes, we estimate the diffusion coefficient over short time scales and compare these to the long time scales results.

An estimate of the short time scale diffusion is obtained by initializing a passive tracer field with Eq. (5.9) and  $R_0 = 1$  km at the same three locations in the Bay.  $k_{\text{net}}$  is computed using Eq. (5.8) over the first hour, and the tracer field is reinitialized at the end of the first hour. Since the tracer field experiences little tidal dispersion initially, this method of computing  $k_{\text{net}}$  over the first hour provides an estimate of the numerical diffusion with  $k_{\text{net}} = k_{\text{num}}$ .  $k_{\text{net}}$  is smaller over the three-day period compared to values computed for the first hour of simulation, since over long time scales smoothing of fronts leads to a reduction of numerical diffusion, and hence results in smaller  $k_{\text{net}}$ . For the case of scale-dependent dispersion, however, the growth of the size of the tracer causes it to sample a larger range of scales of turbulence, and the dispersion coefficient depends on the size of the tracer to the 4/3-power (Richardson 1926; Batchelor 1969).

As shown in Fig. 5.11, over short time scales the TVD scheme introduces a smaller amount of numerical diffusion compared to first-order upwinding at all three locations.  $k_{\text{net}}$  is computed for short time scale simulations and tabulated in Table 5.3. The values are approximately a factor of two smaller for the TVD scheme compared to first-order upwinding. This indicates that the implementation of a second order accurate, TVD scheme is crucial to accurately simulate the transport of a passive tracer field over short time scales. This effect is important particularly for periodic stratification in which numerical diffusion acts primarily over tidal time scales. For this reason the TVD scheme produces results that are more accurate than first-order upwinding for the salinity results described in Chapter 3.

## 5.5 Summary

A domain-averaged formulation provides an estimate for numerical diffusion without the need for analytical methods like the Hirt analysis in Chapter 4. The ability of the domain-averaged formulation to infer diffusion coefficients is verified with idealized

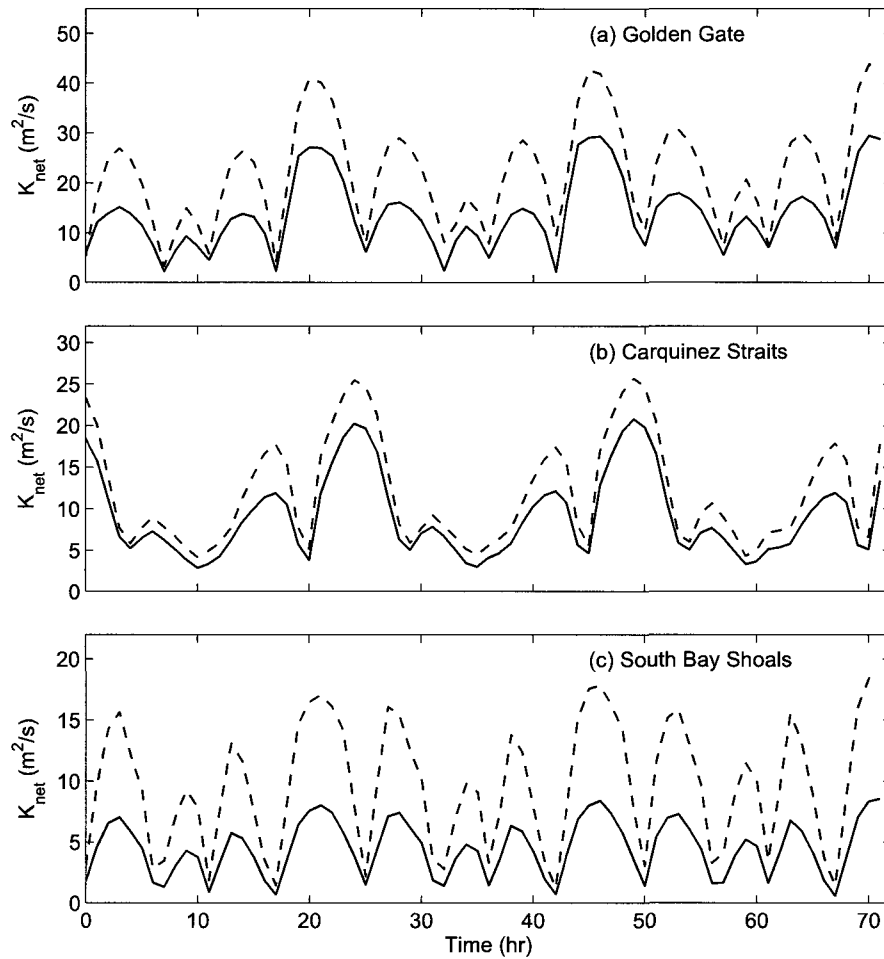


Figure 5.11: Comparison of  $k_{\text{net}}$  with reinitialization at (a) Golden Gate (b) Carquinez Straits (c) South Bay Shoals. Legend: first-order upwind (---), TVD (—).

Table 5.3: Mean  $k_{\text{net}}$  (in  $\text{m}^2 \text{s}^{-1}$ ) in San Francisco Bay for the re-initialized simulations and those run over a three-day period.

| Location         | Re-initialized |      | Three days |     |
|------------------|----------------|------|------------|-----|
|                  | Upwind         | TVD  | Upwind     | TVD |
| Golden Gate      | 22.0           | 13.9 | 3.0        | 3.4 |
| Carquinez Strait | 11.9           | 9.0  | 3.5        | 3.1 |
| South Bay Shoals | 9.7            | 4.5  | 3.0        | 1.0 |

simulations, and this formulation is applied to San Francisco Bay to assess the impacts of tidal dispersion and different time scales on numerical diffusion.

In regions of high tidal dispersion, strong stirring of the tracer field leads to grid-scale variability that produces equivalent  $k_{\text{net}}$  for the first-order upwind and TVD schemes.  $k_{\text{net}}$  is lower for the TVD scheme only in regions where tidal dispersion is relatively low. The importance of time scales on numerical diffusion is investigated by reinitializing the tracer field every hour and computing the diffusion coefficients after one hour of simulation. For short time scales,  $k_{\text{net}}$  is consistently smaller for the TVD scheme compared to first-order upwinding, which verifies results in Chapter 3 that demonstrate the effectiveness of the TVD scheme in producing salinity results that are more accurate than those obtained with first-order upwinding.

# Chapter 6

## Potential climate change impacts on estuarine circulation and salinity intrusion

### 6.1 Introduction

In this chapter, we employ the three-dimensional unstructured-grid SUNTANS model to assess the implications of sea-level rise and hydrologic changes to the estuarine system. An increase in the rate of sea-level rise is one of the primary impacts of global climate change, which combined with changes to the local hydrology due to global warming is expected to modify salinity intrusion and estuarine circulation in North San Francisco Bay.

### 6.2 Numerical Model

We employ the three-dimensional, unstructured-grid SUNTANS model (Fringer et al. 2006) to simulate the flow in San Francisco Bay. The model inputs include high-resolution bathymetry from the NGDC database (Fig. 2.1) and an unstructured grid that enables refinement of the complex coastline (Fig. 2.2). The model is tidally



forced at the open ocean boundary with the 8 major tidal constituents from observed water surface elevations at Point Reyes. Freshwater inflow estimates from the DAYFLOW program (CDWR 1986) are imposed as flow boundary conditions at the Delta boundary. The model is calibrated for the 45-day period 1 January - 15 February 2005, using 32 processors on the Peter A. McCuen Environmental Computing Center at Stanford University, such that the simulations run roughly ten times faster than real time. The spring and neap tidal cycles and the mixed semi-diurnal and diurnal tidal ranges for surface elevations and currents are reproduced by the model. The salinity predictions are in good qualitative agreement with observation in terms of amplitude and phase, and the model is able to capture the periodic stratification of the estuary. Predicted  $X_2$  ranges from 67.3 km to 70.6 km in the calibration period, which compares well with the observed  $X_2$  value on 23 February 2005 of 68.5 km. We use these simulations as the baseline and study the effect of changes in mean sea level and freshwater inflows. Details of the implementation and validation are discussed in Chap. 2.

### 6.3 Climate Change Scenarios

Over the past century, mean sea level at Golden Gate has risen by 0.22 m (Flick 2003) consistent with global average rates (Church et al. 2004). Based on global mean temperatures as projected by the CCSM3 global climate model under the A2 greenhouse gas emissions scenario, 100-year projections of mean sea level at Golden Gate were produced by Cayan et al. (2008) using the method of Rahmstorf (2007). To study the impact of sea-level rise, we initialize the model with different mean sea-level heights based on values derived from the CCSM3-A2 global climate model. Four scenarios are studied, namely: 0.00 m (year 2000), 0.46 m (year 2050), 1.00 m (year 2081) and 1.39 m (year 2099). The tides are then forced relative to the different mean sea-level heights, and we assume that the tidal constituents remain constant with sea-level rise (Cayan et al. 2008; Knowles 2010).

Climate change impacts on hydrology are difficult to assess due to uncertainties in the projections of temperature and precipitation (Dettinger 2005; Maurer and

Duffy 2005). However, it is likely that rising global temperatures will impact the Sacramento-San Joaquin watershed by reducing the snowpack, which would produce higher winter but reduced spring-summer flows (Miller et al. 2003; Dettinger et al. 2004; Knowles and Cayan 2002; Knowles and Cayan 2004). Rather than impose predicted inflows, we impose constant-in-time average seasonal inflows from the estimates of Knowles and Cayan (2004), namely: low inflow of  $300 \text{ m}^3\text{s}^{-1}$  based on average summer conditions, a baseline average inflow of  $800 \text{ m}^3\text{s}^{-1}$ , and a high inflow of  $2000 \text{ m}^3\text{s}^{-1}$  based on average winter conditions.

Sea-level rise leads to an increase in the tidal prism of the Delta and flooding of Delta islands. The difficulties in modeling the inundation of low-lying Delta regions are circumvented by using a model with a false delta approximation (Figure 2.2). The “false delta” consists of two rectangles sized to obtain the correct tidal behavior of the Delta as seen by the eastern boundary of the SUNTANS domain, while eliminating the need to resolve the highly complex channels and tributaries that make up the Delta. Making the assumption of “hard shorelines”, i.e. levees/dikes are built to ensure the shoreline perimeter does not increase with rising sea levels, and eliminating the vulnerability of levee failures, the potential threat of shoreline retreat that could lead to an increase in the tidal prism of the Bay is not considered in our scenarios.

In summary, we perform a total of twelve simulations consisting of four different sea-level rise scenarios and three different freshwater inflow scenarios. All simulations are initialized with the same salinity field which is obtained from United States Geological Survey (USGS) synoptic observations collected on 11 Jan 2005. This data consist of vertical profiles of salinity at 1 m vertical resolution at 39 sampling locations along the longitudinal axis of San Francisco Bay. Interpolation to the three-dimensional grid points is performed under the assumption of no lateral variability. The ocean salinity is assumed to be fixed at 33.5 psu for all scenarios. The modeled salinity field is nearly tidally-periodic after 15 days of spin-up time, and results are analyzed for the remaining 30 days.

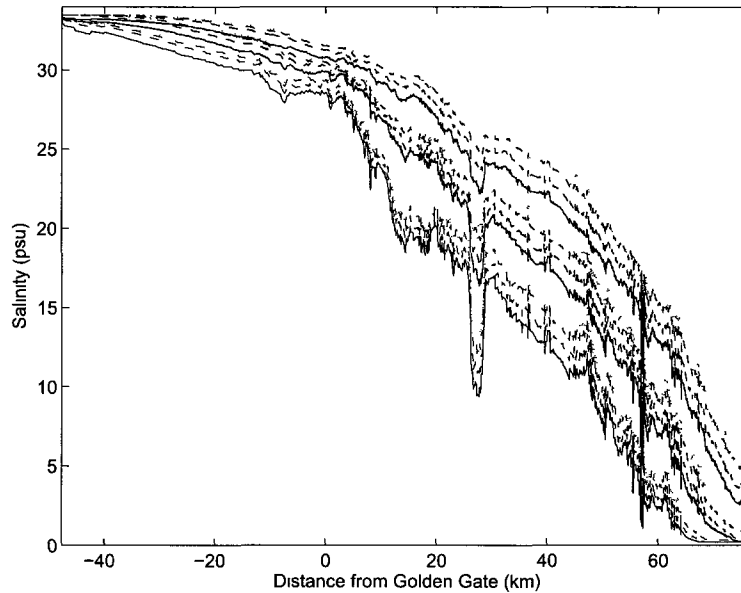


Figure 6.1: Tidal and depth-averaged salinities from the Golden Gate along the longitudinal axis in North San Francisco Bay. Distances into the Bay are positive and those towards the ocean are negative. Legend: Freshwater inflows  $2000 \text{ m}^3\text{s}^{-1}$  (black),  $800 \text{ m}^3\text{s}^{-1}$  (red),  $300 \text{ m}^3\text{s}^{-1}$  (blue), and sea-level rise 0 m (—) 0.46 m (— —), 1.00 m (— ·) and 1.39 m (· · ·).

## 6.4 Salinity intrusion and estuarine circulation

The climate change scenario simulations described in Section 6.3 are performed to investigate their influence on salinity intrusion and changes to the estuarine circulation in North San Francisco Bay. Fig. 6.1 shows depth-averaged salinity fields that are averaged over simulation day 32 along a longitudinal transect extending from the Pacific Ocean and through North San Francisco Bay to the eastern boundary of the domain (see Fig. 2.1). The results show that sea-level rise leads to higher salinities due to greater intrusion of salinity further upstream into North Bay, while increased inflows freshen the Bay and push the salinity field downstream.

The interplay between rising sea levels and variable freshwater inflows is further illustrated with vertical profiles of tidally-averaged salinity along a transect in Carquinez Strait (black line in Fig. 2.1) for the different scenarios. The changes

in estuarine circulation depicted in Fig. 6.2 are investigated qualitatively from the cross-sectionally and tidally averaged salt transport equation (Fischer et al. 1979):

$$A \frac{\partial s}{\partial t} + \frac{\partial}{\partial x}(Qs) = \frac{\partial}{\partial x} \left[ K A \frac{\partial s}{\partial x} \right], \quad (6.1)$$

where  $A$  is the cross-sectional area,  $s$  is the salinity,  $Q$  is the river flow,  $K$  is the longitudinal dispersion coefficient, and  $x$  is measured upstream from the mouth of the estuary.

By assuming a balance between the longitudinal pressure gradient arising from the longitudinal salinity gradient and turbulent shear stresses arising primarily from bottom-generated turbulence, Hansen and Rattray (1965) demonstrate that the magnitude of the baroclinically-induced gravitational circulation is proportional to the longitudinal salinity gradient. A velocity scale for the exchange flow is represented with

$$U_{GC} \sim \frac{\beta g \frac{\partial s}{\partial x} H^3}{\nu_t}, \quad (6.2)$$

where  $\beta$  is the coefficient of salt expansion,  $H$  is the water depth, and  $\nu_t$  is the vertical eddy diffusivity. At steady state, the salt balance in Eq. (6.1) is given by

$$-\frac{Q}{A}s = K_x \frac{\partial s}{\partial x}. \quad (6.3)$$

The longitudinal dispersion coefficient  $K$  is obtained from the balance between the horizontal advection of the salinity gradient and vertical diffusion of the vertically varying salinity perturbation, and is given by

$$K \sim \frac{(\beta g)^2 \left(\frac{\partial s}{\partial x}\right)^2 H^8}{\nu_t^3}. \quad (6.4)$$

Increased inflows cause the compression of isohalines, which is observed in Fig. 6.2. From the steady state salt balance, higher inflows result in a stronger horizontal salinity gradient. The velocity scale in Eq. (6.2) is proportional to the longitudinal salinity gradient, indicating a higher horizontal salinity gradient results in stronger gravitational circulation. From Eq. (6.4), an increased horizontal salinity gradient

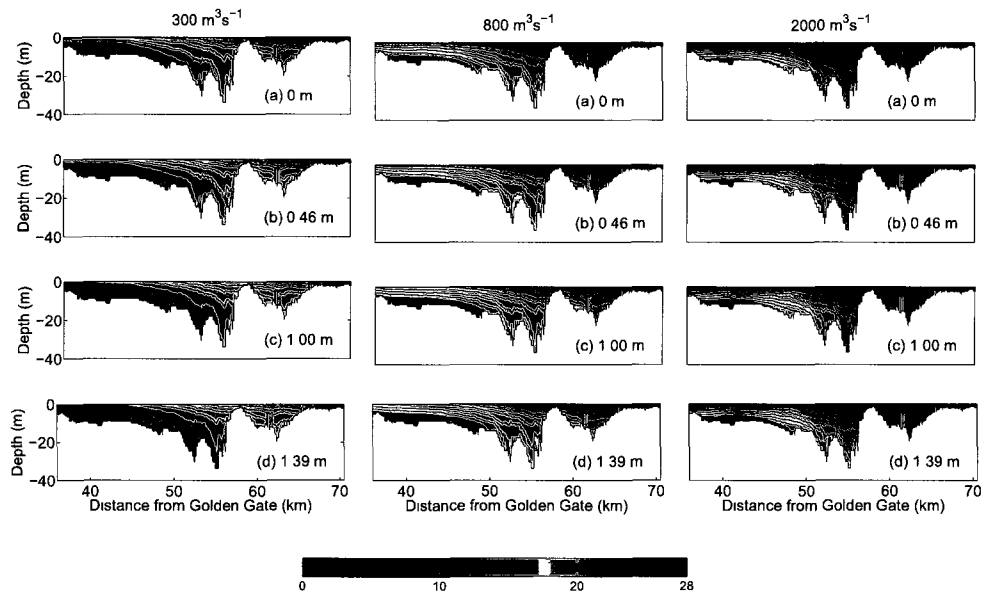


Figure 6.2: Vertical profiles of tidally-averaged salinity along a transect in Carquinez Strait (black line in Fig. 2.1) for  $2000 \text{ m}^3\text{s}^{-1}$ ,  $800 \text{ m}^3\text{s}^{-1}$  and  $300 \text{ m}^3\text{s}^{-1}$  freshwater inflows, and (a) 0 m (b) 0.46 m (c) 1.00 m (d) 1.39 m sea-level rise.

corresponds to higher longitudinal dispersion.

Rising sea levels result in a stronger baroclinic pressure gradient which is proportional to the water depth. The longitudinal pressure gradient arises from the longitudinal salinity gradient, indicating an increase in the strength of the gravitational circulation (Eq. 6.2) and a larger longitudinal dispersion coefficient (Eq. 6.4). Sea-level rise reduces the impact of bottom-generated turbulence, which leads to less vertical mixing, both of which results in stronger gravitational circulation (Eq. 6.2) and larger longitudinal dispersion (Eq. 6.4).

## 6.5 Quantifying salinity intrusion due to sea-level rise

An indicator for effective management of estuarine biological resources as well as to set standards for managing freshwater inflows in San Francisco Bay is proposed by the Environmental Protection Agency (EPA) (Schubel 1993; Kimmerer and Schubel 1994). The isohaline position  $X_2$ , which is defined as the distance (in km) from the Golden Gate Bridge measured along the longitudinal axis to the location where the bottom salinity is 2 psu, is selected for this purpose.  $X_2$  is correlated with a number of variables, including inflows, estuarine habitats and abundance of organisms. In the present analysis we employ  $X_2$  as a measure of salinity intrusion into the Bay.

A method of estimating  $X_2$  from salinity observation data is outlined in Jassby et al. (1995). Predictions of  $X_2$  can be computed from a time-series regression relationship (Jassby et al. 1995) or obtained from salinity predictions using hydrodynamic modeling (MacWilliams et al. 2005). The ability of regression relationships to predict  $X_2$  is limited for high and low flow conditions, while hydrodynamic models obtain  $X_2$  which match observed  $X_2$  over a range of inflows (MacWilliams et al. 2005). The ability of numerical models to accurately compute  $X_2$  under current conditions suggest that it is appropriate to use hydrodynamic models to predict  $X_2$  for the climate change scenario simulations. Salinity predictions obtained along the thalweg in North San Francisco Bay are averaged over day 32, and  $X_2$  is computed by interpolation to

find the location along this transect at which bottom salinity is equal to 2 psu.

The salinity intrusion length scale can be derived from classical estuarine theory under the assumption of constant vertical mixing coefficients (Hansen and Rattray 1965). The expression for the longitudinal dispersion coefficient  $K$  given in Eq. (6.4) is substituted into the steady state salt balance (Eq. 6.3) to obtain

$$-\frac{Q}{A}s = K \frac{\partial s}{\partial x} = \frac{(\beta g)^2 H^8}{\nu_t^3} \left( \frac{\partial s}{\partial x} \right)^3. \quad (6.5)$$

Rearranging Eq. (6.5), the salinity intrusion length scale becomes

$$X_2 \sim \frac{(W\alpha)^{1/3}(\beta g s)^{2/3} H^3}{Q^{1/3} \nu_t}, \quad (6.6)$$

where  $W$  is the width of the estuary, and  $\alpha = 5.4 \times 10^{-5}$  is the constant of proportionality. From the scaling in Eq. (6.6),  $X_2$  is shown to be proportional to  $Q$  to the  $-1/3$  power. Increased inflows result in a stronger horizontal salinity gradient, as seen from the steady state salt balance in Eq. (6.3). The balance between the divergence of the shear stress and the baroclinic pressure gradient arising from the longitudinal salinity gradient leads to a velocity scale for the exchange flow given in Eq. (6.2) from which stronger gravitational circulation is obtained with higher horizontal salinity gradient. The increase in the strength of the gravitational circulation acts to create higher vertical stratification, leading to the nonlinear feedback between vertical mixing and stratification, hence resulting in decreased sensitivity of  $X_2$  to variability of inflows. Interestingly, field experiments by Monismith et al. (2002) in San Francisco Bay found a similar weak dependence on inflows, such that  $X_2$  is proportional to  $Q$  to the  $-1/7$  power. Sea-level rise decreases the impact of bottom-generated turbulence, which leads to less vertical mixing. The scaling relationship in Eq. (6.6) demonstrate an increase in  $X_2$  when the vertical eddy diffusivity decreases.

The dependence of  $X_2$  on  $Q$  for different sea-level rise scenarios is shown in Fig. 6.3. Applying regression analysis to the data, the coefficients for the least-squares fit of the form  $X_2 = bQ^n$  are tabulated in Table 6.1. Rising sea levels lead to greater dependence of  $X_2$  on  $Q$  since the exponent  $n$  in  $Q^n$  increases in absolute value. An

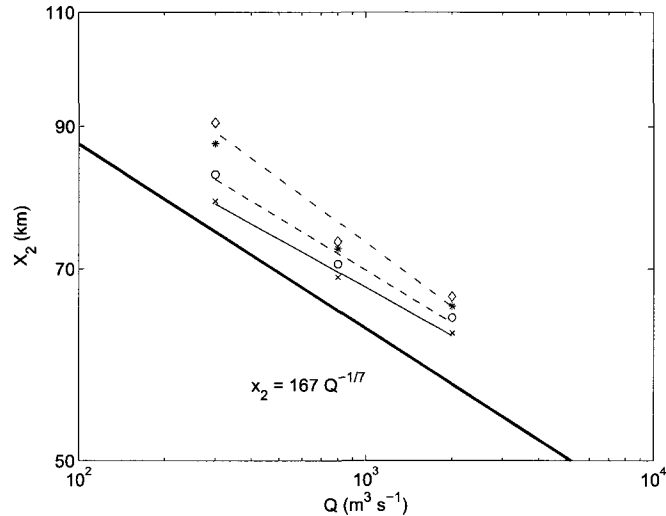


Figure 6.3: Dependence of salinity intrusion length scale  $X_2$  on inflows. Legend: Sea-level rise scenarios 0.00 m (—, ×), 0.46 m (—, ○), 1.00 m (⋯, \*), 1.39 m (· - ·, ◇).

increase in the water depth leads to a weaker dependence on  $\partial S/\partial x$  because in the limit of deep water  $\partial S/\partial x = 0$ . This is consistent with the results of Bowen (2002), who found  $X_2$  has a  $Q^{-1}$  dependence and is independent of  $\partial S/\partial x$ , in the limit of gravitational circulation having no effect on salt transport. Also, overlaid on Fig. 6.3 is the result  $X_2 = 167Q^{-1/7}$  obtained from field experiments in San Francisco Bay by Monismith et al. (2002). Even though our exponent values are consistently higher, they are within the range of scatter of the data used by Monismith et al. (2002). Our results show for the scenario with no sea-level rise,  $X_2 \sim Q^{-1/8}$ , with a 95.7% confidence level.

The change in  $X_2$  with sea-level rise for different inflow scenarios is shown in Fig. 6.4. A regression analysis is performed of the form  $X_2 = c(H_0 + \Delta H)^m$ , where  $H_0 = 12.4$  m is the average depth over the transect and  $\Delta H$  is the sea-level rise. The coefficients for the least-squares fit are tabulated in Table 6.2. Following the salinity intrusion length scaling in Eq. (6.6),  $X_2$  is proportional to  $H$  to the third-power. However, since  $\nu_i \sim H$ , the dependence of  $X_2$  on  $H$  is reduced to  $X_2 \sim H^2$ . Our scenario simulations indicate that  $m$  is within the range 0.5 and 1.3, with a 99.9%



Table 6.1: Least-squares fit of the form  $X_2 = bQ^n$  for sea-level rise scenarios in Fig. 6.3.

| Sea-level rise<br>(m) | b<br>( $\times 10^5$ ) | n      | Confidence level<br>(%) |
|-----------------------|------------------------|--------|-------------------------|
| 0.00                  | 1.57                   | -0.122 | 95.7                    |
| 0.46                  | 1.74                   | -0.133 | 92.3                    |
| 1.00                  | 2.04                   | -0.151 | 90.8                    |
| 1.39                  | 2.24                   | -0.162 | 88.4                    |

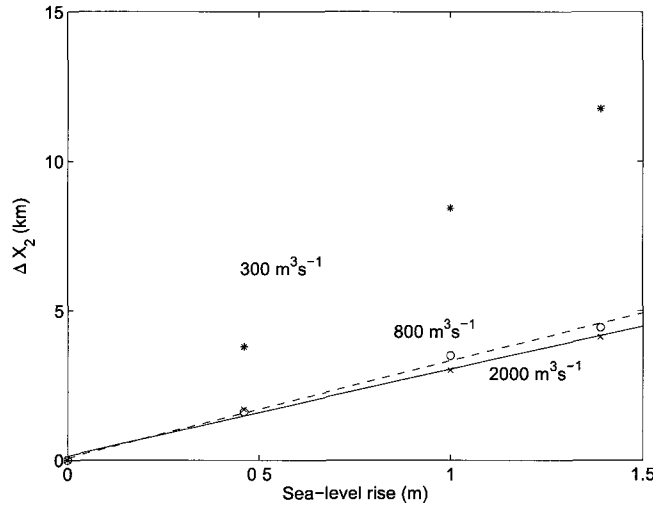


Figure 6.4: Dependence of salinity intrusion length scale  $X_2$  on sea-level rise. Legend: Freshwater inflows  $2000 \text{ m}^3\text{s}^{-1}$  (—, ×),  $800 \text{ m}^3\text{s}^{-1}$  (---, o), and  $300 \text{ m}^3\text{s}^{-1}$  (⋯, \*).

confidence level.

Under low-flow conditions, the exponent  $m$  is the largest, since sea-level rise has a greater effect on salinity intrusion due to weaker vertical stratification in the presence of low inflows. For baseline and high inflows, the exponent  $m$  is reduced approximately by a factor of 2, with the smallest  $m$  obtained for high-flow conditions. For high-flow conditions, the exponent is the smallest. Stronger inflows increase the strength of gravitational circulation, which acts to create higher vertical stratification leading to the nonlinear feedback between vertical mixing and stratification. The effect of sea-level rise on vertical stratification and consequently salinity intrusion is reduced, owing to the suppression of mixing by stratification.

Table 6.2: Least-squares fit of the form  $X_2 = c(H_0 + \Delta H)^m$  for the inflow scenarios in Fig. 6.4.

| Inflows<br>( $\text{m}^3\text{s}^{-1}$ ) | c<br>( $\times 10^4$ ) | m     | Confidence level<br>(%) |
|--|------------------------|-------|-------------------------|
| 300                                      | 0.290                  | 1.31  | 99.9                    |
| 800                                      | 1.54                   | 0.595 | 99.7                    |
| 2000                                     | 1.42                   | 0.588 | 99.6                    |

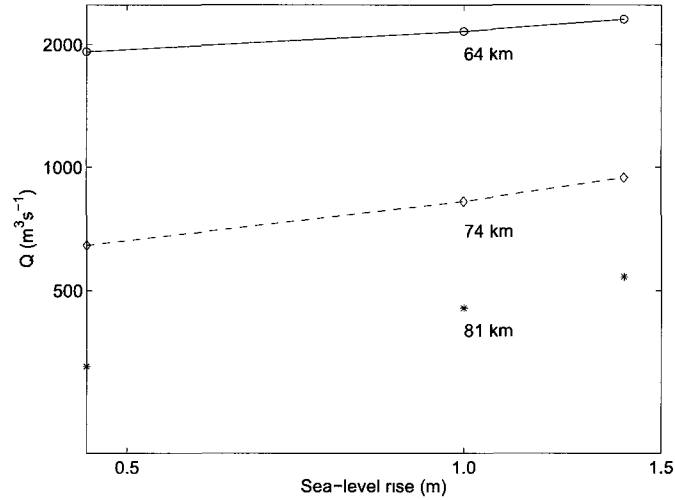


Figure 6.5: Inflows required to maintain  $X_2$  standards for the sea-level rise scenarios. Legend: Port Chicago  $X_2 = 64$  km ( $\text{—}$ ,  $\circ$ ), Chipps Island  $X_2 = 74$  km ( $\text{-- --}$ ,  $\diamond$ ), and Collinsville  $X_2 = 81$  km ( $\cdots$ ,  $*$ ).

## 6.6 Estimating the effect of sea-level rise on $X_2$

Direct measurements of inflows in San Francisco Bay cannot be made because of the complex geometry of the channels, which results in a high degree of uncertainty particularly at low flows. Therefore,  $X_2$  is used as a substitute for regulating inflows to ensure that sufficient fresh water is available to flush the Bay. A set of standards for  $X_2$  was proposed in the 1994 Bay-Delta Accord, which explicitly states  $X_2$  maintained at Port Chicago, Chipps Island and Collinsville are respectively 64, 74 and 81 km. The steady-state inflows required to maintain  $X_2$  at 64, 74 and 81 km are respectively  $826 \text{ m}^3\text{s}^{-1}$ ,  $352 \text{ m}^3\text{s}^{-1}$  and  $194 \text{ m}^3\text{s}^{-1}$  (Sullivan and Richard 1994).

Fig. 6.5 shows the amount of freshwater inflows required to maintain  $X_2$  at the three locations for the different sea-level rise scenarios. This was determined from Fig. 6.3 where for each sea-level rise scenario the amount of inflows required to maintain  $X_2$  at 64, 74 and 81 km are interpolated from the plot. Note that Fig. 6.5 is a log-log plot and spacing between small values are amplified. All three locations show with sea-level rise increased inflows is required to maintain  $X_2$  at its current location. Sea-level rise decreases bottom-generated turbulence, which leads to less vertical mixing and results in stronger gravitational circulation. This causes higher vertical stratification and greater salinity intrusion, hence requiring greater inflows to maintain  $X_2$  at its current location. The largest increase in inflows from current conditions is required to maintain  $X_2$  at the downstream location at Port Chicago, since this is the closest location amongst the three to the Pacific Ocean and most affected by sea-level rise. The increase in inflows required to maintain  $X_2$  at its current location due to a 1.39 m sea-level rise at Port Chicago, Chipps Island and Collinsville are respectively  $711 \text{ m}^3 \text{ s}^{-1}$ ,  $456 \text{ m}^3 \text{ s}^{-1}$  and  $308 \text{ m}^3 \text{ s}^{-1}$ .

## 6.7 Summary

The three-dimensional unstructured-grid SUNTANS model is employed to assess the implications of sea-level rise and hydrologic changes on salinity intrusion and estuarine circulation in North San Francisco Bay. Climate change scenario simulations with sea-level rise projections derived from the CCSM3-A2 global climate model are performed under hydrologic conditions of low, baseline and high freshwater inflows, and their effects on the salinity intrusion length are quantified. Rising sea levels reduce the impact of bottom-generated turbulence causing less vertical mixing. This creates stronger gravitational circulation and higher vertical stratification, resulting in enhanced salinity intrusion. Under low-flow conditions, salinity intrusion is the largest, since sea-level rise has a greater impact due to weaker vertical stratification. Strong flows increase the strength of the gravitational circulation, resulting in higher vertical stratification, which leads to the nonlinear feedback between vertical mixing and stratification. The effect of sea-level rise on vertical stratification and consequently

salinity intrusion is reduced owing to the suppression of mixing by stratification. With sea-level rise increased inflows are required to maintain current  $X_2$  standards. The least increase in inflows is required to maintain  $X_2$  at the downstream location at Port Chicago.

# Chapter 7

## Conclusion

### 7.1 San Francisco Bay numerical model

Three-dimensional simulations of San Francisco Bay are performed with the unstructured-grid SUNTANS model. A TVD scalar transport scheme is included in the model and modified to work for flows with extensive wetting and drying. The model inputs include high resolution bathymetry from the NGDC database and an unstructured grid that enables refinement of the complex coastline. The model is tidally forced with water surface elevations at the open ocean boundary. Freshwater inflow estimates from the DAYFLOW program are imposed as flow boundary conditions at the Delta boundary. A 45-day three-dimensional simulation runs roughly ten times faster than real time. The bottom roughness is adjusted to reproduce the observed sea-surface heights and currents with the model. With no further tuning, the model is validated with salinity observations in North San Francisco Bay.

The model-predicted surface elevations and depth-averaged currents compare well with observations at most locations in the Bay. The spring and neap tidal cycles, and the mixed semi-diurnal and diurnal tidal ranges for surface elevations and depth-averaged currents are reproduced by the model. However, predicted surface elevations show errors at upstream locations at Mare Island and Port Chicago, which arise largely due to the false delta approximation. As the focus of our work is on salinity simulations at Benicia and Point San Pablo, these errors upstream have little effect.

The depth-averaged currents demonstrate small errors in amplitudes and phases at the Richmond and Oakland ADPs. Comparisons of predicted velocity profiles with observations also show the presence of errors at these locations. These errors are likely a result of performing advection of momentum using ELM with a low-order scheme that has linear interpolation. The model realistically predicts the tidal time scale variability in salinity. The salinity predictions also capture the periodic stratification of the estuary by obtaining with a high degree of accuracy the surface and bottom salinity at Point San Pablo (PSP) and Benicia (BEN). This indicates the MY2.5 turbulence closure scheme represents the effects of stratification on turbulence reasonably well for North San Francisco Bay.

## 7.2 Sensitivity analysis of salinity simulations

A sensitivity study is performed to determine the effects of grid resolution, the turbulence model, and the scalar transport scheme on salinity simulations in North San Francisco Bay. Comparisons of salinity predictions with observations are made with three levels of grid refinement, and simulations are performed on each mesh with four different scenarios to evaluate the relative effects of the scalar transport scheme and the turbulence model.

The grid resolution study indicates that model convergence is highly sensitive to the choice of the advection scheme and the turbulence model. The best convergence rate in space is achieved when the TVD scheme is employed for salt transport and the turbulence model is employed. This accuracy degrades without the turbulence model due to the lack of feedback between vertical mixing and stratification. The result is an increase in error by one order of magnitude and a smaller convergence rate. Use of first-order upwinding further increases the errors roughly by a factor of two. Despite an expected first-order rate of convergence, these errors do not decrease when the mesh is refined. The impact of the turbulence model on the errors is also negligible when first-order upwinding is used.

Lack of convergence and large errors when first-order upwinding is used result from horizontal numerical diffusion that leads to a diffuse salt wedge and decreased

baroclinic circulation. The errors are much more sensitive to mesh refinement and the turbulence model when the TVD scheme is used because of the increased horizontal salinity gradient. This ensures that nonlinear feedback between vertical mixing and stratification can take place when the turbulence model is employed. A diffuse salt wedge prevents the formation of sufficient vertical stratification that would damp the vertical mixing and lead to further salinity intrusion.

A salt-flux analysis shows that, when first-order upwinding is used, the salt flux does not change when the grid is refined or when the turbulence model is employed. Horizontal salinity gradients are so weak that the tidal flux of salt is larger than the steady exchange flux. This is in contrast to the results of using the TVD scheme, which shows that the salt fluxes are smaller on the coarse grid than on the fine grid. Use of the TVD scheme produces a compressed salinity front that resolves more of the baroclinic circulation. This has the effect of producing a larger tidal flux to balance the river flux without the turbulence model. On the coarse grid, lack of the turbulence model does not change the tidal flux, but instead the reduction of the river flux is balanced by an equal reduction in the exchange flux.

### 7.3 Numerical scalar diffusion on unstructured grids

The quantification of numerical diffusion from scalar transport is employed to assess the performance of first-order upwind and second-order scalar advection schemes on unstructured grids. The quantification of numerical diffusion resulting from scalar transport on unstructured grids is obtained using an analytical approach by extending the Hirt analysis (Hirt 1968) on Cartesian grids to unstructured grids. We assume uniform flow on a grid composed of equilateral triangles in the derivation of analytical numerical diffusion coefficients.

We introduce two methods, termed the independent analysis and the combined analysis to compute the modified form of the advection equation. The independent analysis separately derives the modified equations for the two types of cells, and this method leads to an overprediction of numerical diffusion coefficients. The combined analysis employs a recurrence relation to derive the equation for one cell, which is

substituted into the Taylor-series expansion of the other type of cell. Holleman et al. (2011) shows that the combined analysis obtains the correct numerical diffusion coefficients for first-order upwinding, and we extend this method to derive diffusion coefficients for the second-order scheme. The second-order scheme is based on the Lax-Wendroff scheme on Cartesian grids which stabilizes central differencing but introduces dispersion.

The numerical diffusion coefficients are verified with idealized simulations using the method of spatial moments analysis, and the coefficients are found to be one order of magnitude smaller for first-order upwinding than the second-order scheme. As the method of spatial moments analysis cannot be employed to compute numerical dispersion coefficients from idealized simulations, the dispersion coefficients are verified with a pseudospectral method. The diffusion and dispersion coefficients are found to be comparable on unstructured grids and two-dimensional Cartesian grids, and the coefficients are identical when one of the edges is aligned with the flow. As Cartesian grids require a larger  $\psi$  for stability, setting the minimum  $\psi$  leads to larger diffusion coefficients on Cartesian grids compared to unstructured grids.

A stability analysis is performed for first-order upwind and the second-order scheme on unstructured grids, and conditions for stability are compared to those on two-dimensional Cartesian grids. For first-order upwinding, the most restrictive Courant number on unstructured grids occurs when  $\theta = \pi/6$  which requires that  $0 \leq C_0 \leq \sqrt{3}/2 \approx 0.87$ . In comparison, the stability condition is stricter on Cartesian grids, and the most restrictive Courant number occurs when  $\theta = \pi/4$ , which requires that  $0 \leq C_0 \leq 1/\sqrt{2} \approx 0.71$ . The second-order scheme is stable on unstructured grids with  $\psi \geq 1.5$  and  $0 \leq C_0 \leq 2/\sqrt{6} \approx 0.82$  for all  $\theta$ . In comparison, on Cartesian grids the second-order scheme has stricter conditions for stability with  $\psi \geq 2$  and  $0 \leq C_0 \leq 1/\sqrt{2} \approx 0.71$  for all  $\theta$ .

An accuracy analysis shows that first-order upwinding is first-order accurate in time and space while the second-order scheme is second-order accurate in time and space. Although the truncation errors of the modified equation are formally first-order for the second-order scheme, the truncation errors are small and the method is effectively second-order accurate in time and space as shown by the accuracy analysis.



## 7.4 Numerical diffusion in San Francisco Bay

A domain-averaged formulation based on the work of Burchard and Rennau (2007) provides an estimate for numerical diffusion without the need to analytically derive it, allowing for a computationally efficient method to compute diffusion coefficients under general flow and triangulation conditions. The net sum of the domain-integrated numerical and physical diffusion is referred to as  $k_{\text{net}}$ .  $k_{\text{net}}$  for three cases with increasing amounts of physical diffusion are computed using first-order upwinding and the TVD scheme, and the ability of the domain-averaged formulation to infer this physical diffusion is demonstrated. A grid resolution study of numerical diffusion shows that a higher convergence rate in space is achieved with the TVD scheme compared to first-order upwinding.

The performance of first-order upwind and the TVD scheme are assessed to determine the effects of tidal dispersion and time scales on numerical diffusion in San Francisco Bay. The three-dimensional, unstructured grid SUNTANS model applied to San Francisco Bay is employed to simulate flow in the Bay, and a passive tracer field is introduced at different locations in the Bay.  $k_{\text{net}}$  is computed to quantify numerical diffusion resulting from scalar transport on unstructured grids.

In regions with strong tidal dispersion,  $k_{\text{net}}$  values are similar for the high- and low-order schemes after an initial smoothing period, due to strong stirring of the tracer field which leads to grid-scale variability.  $k_{\text{net}}$  is lower for the TVD scheme only in regions where tidal dispersion is relatively low. The importance of time scales on numerical diffusion is investigated by reinitializing the tracer field every hour and computing the diffusion coefficient after one hour of simulation. For short time scales,  $k_{\text{net}}$  is consistently smaller for the TVD scheme compared to first-order upwinding.

## 7.5 Potential climate change impacts on estuarine circulation and salinity intrusion

The three-dimensional unstructured-grid SUNTANS model is employed to assess the implications of sea-level rise and hydrologic changes on salinity intrusion and estuarine

circulation in North San Francisco Bay. Climate change scenario simulations with sea-level rise projections derived from the CCSM3-A2 global climate model are performed under hydrologic conditions of low, baseline and high freshwater inflows, and their effects on salinity intrusion and salt flux are quantified.

Sea-level rise reduces the impact of bottom-generated turbulence causing less vertical mixing, which increases the strength of the gravitational circulation. This leads to higher vertical stratification and enhanced salinity intrusion. Under low-flow conditions, salinity intrusion is the largest, since sea-level rise has a greater impact due to weaker vertical stratification. Strong flows result in stronger gravitational circulation that creates higher vertical stratification leading to the nonlinear feedback between vertical mixing and stratification. The effect of sea-level rise on vertical stratification and consequently salinity intrusion is reduced owing to the suppression of mixing by stratification.

Policy decisions are guided by the location of  $X_2$  in San Francisco Bay. As sea-level rises and with climate-induced alterations to inflows into the Bay, the location of  $X_2$  is likely to shift, indicating changes to estuarine conditions and resources.  $X_2$  is used as a substitute for regulating inflows to ensure that sufficient freshwater is available to flush the Bay, and a set of standards was proposed to maintain  $X_2$  at Port Chicago, Chipps Islands and Collinsville. At all three locations increased inflows are required to maintain  $X_2$  at its current location with sea-level rise. The largest increase in inflows is required to maintain  $X_2$  at the downstream location at Port Chicago, since this is the closest location amongst the three to the Pacific Ocean.

## 7.6 Recommendations

Even though our calibration and validation runs show predicted sea-surface heights, currents and salinity match well with observations, improvements to the three-dimensional SUNTANS model of San Francisco Bay can be made by using a better false delta and including the effects of wind and all freshwater sources, i.e., small rivers and creeks in the southern end of South Bay. The sensitivity analysis in Chapter 3 demonstrates the importance of horizontal grid resolution in salinity simulations, with the mean

and RMS errors decreasing with near second-order accuracy as the grid is refined. Hence our model could be improved by providing greater horizontal grid resolution. Employing higher resolution bathymetric sources and more accurate specification of  $z_0$  is also likely to result in better simulation results.

Our calibration and validation results can also be improved by using a high-order scheme with quadratic interpolation, which will reduce numerical diffusion when employing ELM for advection of momentum (Wang et al. 2011b). Our current runs are performed with a low-order scheme with linear interpolation resulting in first-order accuracy for the advection of momentum. Including the influence of the coastal Pacific Ocean might also improve our simulation results, however this is a smaller effect as our calibration and validation runs are performed in the winter season with high freshwater inflows and minimal upwelling. The potential effects of the coastal ocean are small particularly in our simulations which are focused on North San Francisco Bay.

The sensitivity analysis determines the effects of horizontal grid resolution, the turbulence model and the scalar transport scheme on salinity simulations. An investigation into the effect of vertical grid resolution would be valuable to assess the impact of varying the stretching ratio of the vertical grid on salinity simulations. Our simulations employ z-levels which are stretched in the vertical to provide extra resolution at the upper layers in order to resolve the flow in shallow regions of the Bay and in the vicinity of the salt wedge at Carquinez Strait, at the expense of under-resolving the bottom boundary layer.

The climate change scenario simulations assess the implications of sea-level rise and hydrologic changes on salinity intrusion and estuarine circulation by making the assumption of “hard shorelines”. The sea-level rise simulations will be more realistic if we employ “soft shorelines” in our model, which can be used to determine the impact of building dams and levees under various simulation scenarios. The development of such models will be extremely valuable for management decisions in planning for climate change.

# Appendix A

This appendix defines position vectors in the analysis. Defining the position vector pointing from centroid of cell  $B_i$  to the centroid of cell  $A_3$  (see Fig. 4.4) as  $\delta_i^{BA} = \delta_i^{BA} \mathbf{e}_x + \delta_i^{BA} \mathbf{e}_y$ , and  $r$  is the distance between Voronoi points of adjacent cells, we have

$$\begin{aligned}\delta_{1x}^{BA} &= -r \cos\left(\frac{\pi}{6} - \theta\right), \\ \delta_{1y}^{BA} &= r \sin\left(\frac{\pi}{6} - \theta\right), \\ \delta_{2x}^{BA} &= r \cos\left(\frac{\pi}{6} + \theta\right), \\ \delta_{2y}^{BA} &= r \sin\left(\frac{\pi}{6} + \theta\right), \\ \delta_{3x}^{BA} &= r \cos\left(\frac{\pi}{2} - \theta\right), \\ \delta_{3y}^{BA} &= -r \sin\left(\frac{\pi}{2} - \theta\right).\end{aligned}\tag{1}$$

Likewise, the components of the position vector showing the relationships between the A and B cells, pointing from the centroid of cell  $A_i$  ( $i = 1, 2, 3$ ) to that of cell  $B_1$

are defined as

$$\begin{aligned}
\delta_{1x}^{AB} &= r \cos\left(\frac{\pi}{2} + \theta\right), \\
\delta_{1y}^{AB} &= r \sin\left(\frac{\pi}{2} + \theta\right), \\
\delta_{2x}^{AB} &= -r \cos\left(\frac{\pi}{6} + \theta\right), \\
\delta_{2y}^{AB} &= -r \sin\left(\frac{\pi}{6} + \theta\right), \\
\delta_{3x}^{AB} &= r \cos\left(\frac{\pi}{6} - \theta\right), \\
\delta_{3y}^{AB} &= -r \sin\left(\frac{\pi}{6} - \theta\right).
\end{aligned} \tag{2}$$

The position vectors pointing from the centroid of cell  $A_i$  ( $i = 1, 2, 3, 4, 5, 6, 7$ ) to that of cell  $A_3$  are defined as

$$\begin{aligned}
\delta_{1x}^{AA} &= -\Delta l \cos\left(\frac{\pi}{3} - \theta\right), \\
\delta_{1y}^{AA} &= \Delta l \sin\left(\frac{\pi}{3} - \theta\right), \\
\delta_{2x}^{AA} &= -\Delta l \cos \theta, \\
\delta_{2y}^{AA} &= -\Delta l \sin \theta, \\
\delta_{3x}^{AA} &= 0, \\
\delta_{3y}^{AA} &= 0, \\
\delta_{4x}^{AA} &= \Delta l \cos\left(\frac{\pi}{3} + \theta\right), \\
\delta_{4y}^{AA} &= \Delta l \sin\left(\frac{\pi}{3} + \theta\right), \\
\delta_{5x}^{AA} &= \Delta l \cos \theta, \\
\delta_{5y}^{AA} &= \Delta l \sin \theta, \\
\delta_{6x}^{AA} &= \Delta l \cos\left(\frac{\pi}{3} - \theta\right), \\
\delta_{6y}^{AA} &= -\Delta l \sin\left(\frac{\pi}{3} - \theta\right), \\
\delta_{7x}^{AA} &= -\Delta l \cos\left(\frac{\pi}{3} + \theta\right), \\
\delta_{7y}^{AA} &= -\Delta l \sin\left(\frac{\pi}{3} + \theta\right).
\end{aligned} \tag{3}$$

# Bibliography

- Anderson, J. and M. Mierzwa (2002). DSM2 tutorial, An introduction to the Delta Simulation Model 2. Technical report, California Dept. Water Res. Tech. report.
- Bakun, A. (1973). Coastal upwelling indices, west coast of North America. Tech. rep. nmfs ssrf-671, 103 pp., Natl. Oceanic. Atmos. Admin., Seattle, Wash.
- Barth, T. J. (1993). Recent development in high order k-exact reconstruction on unstructured meshes. Technical report, AIAA paper 93-0668.
- Batchelor, G. K. (1969). Computation of the energy spectrum in homogeneous two-dimensional turbulence. *Phys. Fluids Supp.* 11, 233–239.
- Blumberg, A. F. and G. L. Mellor (1987). A description of a three-dimensional coastal ocean circulation model. In N. S. Heaps (Ed.), *Three dimensional coastal ocean models*, Washington, D.C. AGU.
- Bobba, A. G. (2002). Numerical modeling of salt-water intrusion due to human activities and sea-level change in the Godavari Delta, India. *Hydrol. Sci.* 47, S67–S80.
- Bouche, F. P. D. and J. M. Ghidaglia (2005). Error estimate and the geometric corrector for the upwind finite volume method applied to the linear advection equation. *SIAM J. Numer. Analys.* 43, 578–603.
- Bowen, M. M. (2002). *Mechanisms and variability of salt transport in partially stratified estuaries*. PhD thesis, Woods Hole/ MIT Joint Program in Phys. Oceano. 171 pp.
- Burchard, H. and H. Rennau (2007). Comparative quantification of physically and

- numerically induced mixing in ocean models. *Ocean Modell.* 20, 293–311.
- Casulli, V. (1990). Semi-implicit finite difference methods for the two-dimensional shallow water equations. *J. Comput. Phys.* 86, 56–74.
- Casulli, V. and E. Cattani (1994). Stability, accuracy and efficiency of a semi-implicit method for three-dimensional shallow water flow. *Comput. Math. Appl.* 27, 99–112.
- Casulli, V. and R. T. Cheng (1992). Semi-implicit finite difference methods for three-dimensional shallow water flow. *Int. J. Numer. Meth. Fluids* 15, 629–648.
- Casulli, V. and R. A. Walters (2000). An unstructured grid, three-dimensional model based on the shallow water equations. *Int. J. Numer. Meth. Fluids* 32, 331–348.
- Casulli, V. and P. Zanolli (2005). High resolution methods for multidimensional advection-diffusion problems in free-surface hydrodynamics. *Ocean Modell.* 10, 137–151.
- Cayan, D. R., P. D. Bromirski, K. Hayhoe, M. Tyree, M. D. Dettinger, and R. E. Flick (2008). Climate change projections of sea level extremes along the California coast. *Clim. Change* 87, S57–S73.
- CDWR (1986). DAYFLOW program documentation and data summary user's guide. Technical report, CA Dept. Water Resour., Sacramento, CA.
- Cheng, R. T., V. Casulli, and J. W. Gartner (1993). Tidal, residual, intertidal mudflat (TRIM) model and its applications to San Francisco Bay, California. *Estuar., Coast. Shelf Sci.* 36, 235–280.
- Cheng, R. T., C. H. Ling, J. W. Gartner, and P. F. Wang (1999). Estimates of bottom roughness length and bottom shear stress in South San Francisco Bay, California. *J. Geophys. Res.* 104, 7715–7728.
- Cheng, R. T. and R. E. Smith (1998, Nov). A nowcast model for tides and tidal currents in San Francisco Bay, California. In *Proc., Ocean Comm. Conf.*, Baltimore, MD, pp. 537–543. Marine Technology Science.

- Chua, V. P. and O. B. Fringer (2011). Sensitivity analysis of three-dimensional salinity simulations in North San Francisco Bay using the unstructured-grid SUNTANS model. *Ocean Modell.* doi:10.1016/j.ocemod.2011.05.007.
- Church, J. A. and N. J. White (2006). A 20th century acceleration in global sea level rise. *Geophys. Res. Lett.* 33, L01602, doi:10.1029/2005GLO24826.
- Church, J. A., N. J. White, R. Coleman, K. Lambeck, and J. X. Mitrovica (2004). Estimates of the regional distribution of sea level rise over the 1950-2000 period. *J. Climate* 17, 2609–2625.
- Cloern, J. E. and F. H. Nichols (1985). Time scales and mechanisms of estuarine variability, a synthesis from studies of San Francisco Bay. *Hydrobiol.* 129, 229–237.
- Cohen, A. (2000). An introduction to the San Francisco Estuary. Technical report, San Francisco Estuary Institute. Save the Bay, San Francisco Estuary Project.
- Conomos, T. J. (1979a). Properties and circulation of San Francisco Bay waters. In T. J. Conomos (Ed.), *San Francisco Bay: The Urbanized Estuary*, San Francisco, CA, pp. 47–84. AAAS, Pacific Division.
- Conomos, T. J. (1979b). *San Francisco Bay: The Urbanized Estuary. Investigation into the natural history of San Francisco Bay and Delta with reference to the influence of man.* San Francisco, CA: AAAS, Pacific Division. 493 pp.
- Conomos, T. J., R. E. Smith, and J. W. Gartner (1985). Environmental setting of San Francisco Bay. *Hydrobiol.* 129, 1–12.
- Conomos, T. J., R. E. Smith, D. H. Peterson, S. W. Hager, and L. E. Schemel (1979). Processes affecting seasonal distributions of water properties in the San Francisco Bay estuarine system. In T. J. Conomos (Ed.), *San Francisco Bay: The Urbanized Estuary*, San Francisco, CA, pp. 115–142. AAAS, Pacific Division.
- Cooper, M. J. P., M. D. Beevers, and M. Oppenheimer (2008). The potential impacts of sea level rise on the coastal region of New Jersey, USA. *Clim. Change* 90, 475–492.



- Darwish, M. S. and F. Moukalled (2003). TVD schemes for unstructured grids. *Int. J. Heat Mass Trans.* 46(4), 599–611.
- Dettinger, M. D. (2005). From climate change spaghetti to climate change distributions for 21st century. *San Francisco Estuary and Watershed Science* 3.
- Dettinger, M. D., D. R. Cayan, M. Meyer, and A. E. Jeton (2004). Simulated hydrologic responses to climate variations and change in the Merced, Carson and American river basins, Sierra Nevada, California, 1900-2099. *Clim. Change* 62, 283–317.
- Dever, E. P. and S. J. Lentz (1994). Heat and salt balances over the northern California shelf in winter and spring. *J. Geophys. Res.* 99, 16001–16017.
- Fischer, H. B., E. J. List, R. C. Y. Koh, J. Imberger, and N. H. Brooks (1979). *Mixing in Inland and Coastal Waters*. San Diego, CA: Academic Press.
- Fletcher, C. A. J. (1997). *Computational Techniques for Fluid Dynamics, Volume I*. Springer-Verlag.
- Flick (2003). Trends in United States tidal datum statistics and tide range. *J. Waterway, Port, Coast. and Ocean Engr.* 129, 155–164.
- Freyberg, D. L. (1986). A natural gradient experiment on solute transport in a sand aquifer: 2. Spatial moments and the advection and dispersion of nonreactive tracers. *Water Resour. Res.* 22, 2031–2046.
- Fringer, O. B., M. Gerritsen, and R. L. Street (2006). An unstructured-grid, finite-volume, nonhydrostatic, parallel coastal ocean simulator. *Ocean Modell.* 14, 139–173.
- Fringer, O. B. and R. L. Street (2005). Reducing numerical diffusion in interfacial gravity wave simulations. *Int. J. Numer. Meth. Fluids* 49(3), 301–329.
- Galperin, B., L. H. Kantha, S. Hassid, and A. Rosati (1988). A quasi-equilibrium turbulent energy model for geophysical flows. *J. Atmos. Sci.* 45, 55–62.
- Gerdes, R., K. C., and J. Willebrand (1991). The influence of numerical advection schemes on the results of ocean general circulation models. *Clim. Dyn.* 5, 211–226.

- Geyer, W. R. (2010). Estuarine salinity structure and circulation. In A. Valle-Levinson (Ed.), *Cont. Issues in Est. Phys.*, pp. 12–26. Cambridge Univ. Press.
- Geyer, W. R. and R. Chant (2006). The physical oceanography processes in the Hudson River estuary. In J. S. Levinton and J. R. Waldman (Eds.), *The Hudson River Estuary*. Cambridge Univ. Press.
- Geyer, W. R. and R. P. Signell (1992). A reassessment of the role of tidal dispersion in estuaries and bays. *Estuaries* 15, 97–108.
- Geyer, W. R., J. H. Trowbridge, and M. M. Bowen (2000). The dynamics of a partially mixed estuary. *J. Phys. Oceanogr.* 30, 2035–2048.
- Gornitz, V., S. Couch, and E. K. Hartig (2001). Impacts of sea level rise in the New York City metropolitan area. *Global Planet Change* 32, 61–88.
- Gross, E. S., J. R. Koseff, and S. G. Monismith (1999a). Evaluation of advective schemes for estuarine salinity simulations. *J. Hydraul. Eng.* 125, 32–46.
- Gross, E. S., J. R. Koseff, and S. G. Monismith (1999b). Three-dimensional salinity simulations of South San Francisco Bay. *J. Hydraul. Eng.* 125(11), 1199–1209.
- Gross, E. S., B. L., and R. G. (2002). Consistency with continuity in conservative advection schemes for free-surface models. *Int. J. Numer. Meth. Fluids* 38(4), 307–327.
- Gross, E. S., M. L. MacWilliams, and W. Kimmerer (2005). Simulating periodic stratification in the San Francisco estuary. *Proc. 9th Int. Conf. Est. Coast. Model.*, 155–175.
- Gross, E. S., M. L. MacWilliams, and W. J. Kimmerer (2009). Three-dimensional modeling of tidal hydrodynamics in the San Francisco estuary. *San Francisco Estuary and Watershed Science* 7(2). 37 pp.
- Hallberg, R. W. (1997). Stable split time stepping schemes for large scale ocean modeling. *J. Comp. Phys.* 135, 54–65.
- Haney, R. L. (1991). On the pressure gradient force over steep topography in sigma coordinate ocean models. *J. Phys. Oceanogr.* 21, 610–619.

- Hansen, D. V. and M. Rattray (1965). Gravitational circulation in straits and estuaries. *J. Mar. Res.* 23, 104–122.
- Harten, A. (1983). High resolution schemes for hyperbolic conservation laws. *J. Comput. Phys.* 49, 357–393.
- Heberger, M., H. Cooley, P. Herrera, P. H. Gleick, and E. Moore (2009). The impacts of sea-level rise on the California coast. Technical report, California Climate Change Center.
- Hennecke, W. G. (2004). GIS-based coastal behavior modeling and simulation of potential land and property loss: Implications of sea-level rise at Collaroy/Narrabeen beach, Sydney (Australia). *Coastal Management* 32, 449–470.
- Higdon, R. L. and A. F. Bennett (1996). Stability analysis of operator splitting for large-scale ocean modeling. *J. Comp. Phys.* 123, 311–329.
- Hirt, C. W. (1968). Heuristic stability theory for finite-difference equations. *J. Comp. Phys.* 2, 339–355.
- Holleman, R., M. T. Stacey, and O. B. Fringer (2011). Numerical diffusion for flow-aligned unstructured grids with application to estuarine modeling. In prep.
- Hollibaugh, J. T. (1996). *San Francisco Bay: The Ecosystem. Further investigation into the natural history of San Francisco Bay and Delta with reference to the influence of man.* San Francisco, CA: AAAS, Pacific Division. 542 pp.
- Hull, C. H. J. and J. G. Titus (1986). Greenhouse effect, sea-level rise, and salinity in the Delaware estuary. Technical report, U.S. Environmental Protection Agency and the Delaware River Basin Commission, Washington, D. C. EPA 230-05-86-010.
- Ip, J. T. C., D. R. Lynch, and C. T. Friedrichs (1998). Simulations of estuarine flooding and dewatering with application to Great Bay, New Hampshire. *Estuar. Coast. Shelf Sci.* 47, 119–141.
- IPCC (2001). Climate change 2001: the scientific basis. Technical report, IPCC Third Asses. Rep., Cambridge, UK.

- IPCC (2007). Climate change 2007: the physical basis, summary for policy makers. Technical report, Contrib. Work. Group I Fourth Assess. Rep. Intergov. Panel Climate Change, Cambridge, UK.
- Jassby, A. D., W. J. Kimmerer, S. G. Monismith, C. Armor, J. E. Cloern, T. M. Powell, J. R. Schubel, and T. J. Vendlinski (1995). Isohaline position as a habitat indicator for estuarine populations. *Eco. Appl.* 5, 272–289.
- Kimmerer, W. J. (2002, December). Physical, biological and management responses to variable freshwater flow into the San Francisco estuary. *Estuaries* 25, 1275–1290.
- Kimmerer, W. J. (2004). Open water processes of the San Francisco Estuary: From physical forcing to biological responses. *San Francisco Estuary and Watershed Science* 2. Article 1.
- Kimmerer, W. J. and M. L. Nobriga (2008). Investigating particle transport and fate in the Sacramento-San Joaquin Delta using a particle tracking model. *San Francisco Estuary and Watershed Science* 6. 26 pp.
- Kimmerer, W. J. and J. R. Schubel (1994). Managing freshwater flows into San Francisco Bay using a salinity standard: results of a workshop. In K. R. Dyer and R. J. Orth (Eds.), *Changes in Fluxes in Estuaries: Implications from Science to Management*, pp. 411–416. Fredensborg, Denmark: Olsen and Olsen.
- King, I. P. and W. R. Norton (1978). Recent application of RMA's finite element models for two dimensional hydrodynamics and water quality. In *Finite Elements in Water Resources*, London. Pentech Press.
- King, I. P. and R. Rachiele (1990). Multi-dimensional modeling of hydrodynamics and salinity in San Francisco Bay. In *Estuarine and Coastal Modeling, Proc. 1st International Conference*, New York, pp. 511–518.
- King, L. P. (1993). A finite element model for three-dimensional density stratified flow. Technical report, Aus. Water Coastal Studies Interim Report.
- Knowles, N. (2010). Potential inundation due to rising sea levels in the San Francisco Bay region. *San Francisco Estuary and Watershed Science* 8. Article 1.

- Knowles, N. and D. R. Cayan (2002). Potential effects of global warming on the Sacramento/San Joaquin watershed and the San Francisco estuary. *Geophys. Res. Letters* 29, 1891–1895.
- Knowles, N. and D. R. Cayan (2004). Elevational dependence of projected hydrologic changes in the San Francisco estuary and watershed. *Clim. Change* 62, 319–336.
- Kosloff, D., M. Reshef, and D. Loewenthal (1984). Elastic wave calculations by the Fourier method. *Bull. Seism. Soc. Am.* 74, 875–891.
- Kutta, W. (1901). Beitrag zur naherungsweise Integration totaler Differentialgleichungen. *Zeitschr. fur Math. u. Phys.* 46, 435–453.
- Largier, J. L. (1996). Hydrodynamic exchange between San Francisco Bay and the ocean: The role of ocean circulation and stratification. In J. T. Hollibaugh (Ed.), *San Francisco Bay: The Ecosystem*, San Francisco, CA, pp. 69–104. AAAS.
- Lax, P. and B. Wendroff (1960). Systems of conservation laws. *Commun. Pure Appl Math.* 13, 217–237.
- Lax, P. D. and B. Wendroff (1964). Difference schemes for hyperbolic equations with high order of accuracy. *Comm. Pure Appl. Math.* 17, 381–398.
- LeBlanc, D. R., S. P. Garabedian, K. M. Hess, L. W. Gelhar, R. D. Quadri, K. G. Stollenwerk, and W. W. Wood (1991). Large-scale natural gradient tracer test in sand and gravel. *Water Resour. Res.* 27, 895–910.
- Leendertse, J. L. (1967). Aspects of a computational model for long-period water-wave propagation. Memorandum rm-5294, The RAND Corporation.
- Leveque, R. J. (2011). *Finite Difference Methods for Ordinary and Partial Differential Equations*. Philadelphia, PA: SIAM.
- Li, X., R. J. Rowley, J. C. Kostelnick, D. Braaten, J. Meisel, and K. Hulbutta (2009). GIS analysis of global impacts from sea level rise. *Photogram. Engr. Remote Sensing* 75, 807–818.

- MacWilliams, M. L. and R. T. Cheng (2006, September). Three-dimensional hydrodynamic modeling of San Pablo Bay on an unstructured grid. In *7th Int. Conf. Hydrosoci. Eng.*, Philadelphia, USA.
- MacWilliams, M. L., E. S. Gross, J. F. DeGeorge, and R. R. Rachiele (2007). Three-dimensional hydrodynamic modeling of the San Francisco estuary on an unstructured grid. In *Proc. Int. Assoc. Hydraul. Eng. Res.*, Venice Italy.
- MacWilliams, M. L., E. S. Gross, and W. Kimmerer (2005). Simulating salt intrusion into Suisun Bay and the Western Delta. *State of the Estuary*.
- Maurer, E. P. and P. B. Duffy (2005). Uncertainty in projections of streamflow changes due to climate change in California. *Geophys. Res. Lett.* *32*. L03704.
- Meisler, H., P. P. Leahy, and L. L. Knobel (1984). Effect of eustatic sea-level changes on saltwater-freshwater in the Northern Atlantic Coastal Plain. Technical report, USGS, Reston, Virginia. USGS Water Supply Paper 2255.
- Mellor, G. L. (1996). *User's guide for a three-dimensional, primitive equation, numerical ocean model*. Princeton, NJ: Program in Atmospheric and Oceanic Sciences, Princeton University. 40 pp.
- Mellor, G. L. and T. Yamada (1982). Development of a turbulence closure model for geophysical fluid problem. *Rev. Geophys. Space Phys.* *20*(4), 851–875.
- Miller, N. L., K. E. Bashford, and E. Strem (2003). Potential impacts of climate change on California hydrology. *J. Am. Water Resour. Assoc.* *39*, 771–784.
- Monismith, S. G., J. R. Burau, and M. T. Stacey (1996). Stratification dynamics and gravitational circulation in northern San Francisco Bay. In J. T. Hollibaugh (Ed.), *San Francisco Bay: The Ecosystem*. Am. Assoc. Adv. Sci.
- Monismith, S. G., W. Kimmerer, J. R. Burau, and M. T. Stacey (2002). Structure and flow-induced variability of the subtidal salinity field in northern San Francisco Bay. *J. Phys. Oceanogr.* *32*, 3003–3019.
- Nelson, A. W. and R. J. Lerseth (1972). A study of dispersion capability of San Francisco Bay-Delta waters. Technical report, California Dept. Water Res., Sacramento, California. 89 pp.

- Nepf, H. M. (1999). Drag, turbulence, and diffusion in flow through emergent vegetation. *Water Resour. Res.* 35, 479–489.
- Nichols, F. H., J. E. Cloern, S. N. Luoma, and D. H. Peterson (1986). The modification of an estuary. *Science* 231, 567–573.
- Nunes, R. A., G. W. Lennon, and D. G. Bowers (1990). Physical behaviour of a large, negative or inverse estuary. *Cont. Shelf Res.* 10, 277–304.
- Nunes, R. A. and J. H. Simpson (1985). Axial convergence in a well-mixed estuary. *Est. Coast. Shelf Sci.* 20, 637–649.
- Okubo, A. (1973). Effect of shoreline irregularities on streamwise dispersion in estuaries and other embayments. *Nether. J. Sea Res.* 6, 213–224.
- Oltmann, R. N. (1998). Indirect measurement of delta outflow using ultrasonic velocity meters and comparison to mass-balance calculated outflow. *IEP Newsletter* 11, 5–8.
- Oude Essink, G. H. P. (1999). Impact of sea level rise in the Netherlands. In J. Bear, A.-D. Cheng, S. Sorek, D. Ouazar, and I. Herrera (Eds.), *Seawater Intrusion in Coastal Aquifers - Concepts, Methods and Practices*, pp. 507–530. Dordrecht, The Netherlands: Kluwer Academic Publishers.
- Park, K. and A. Y. Kuo (1996). Effect of variation in vertical mixing on residual circulation in narrow, weakly nonlinear estuaries. In D. G. Aubrey and C. T. Friedrichs (Eds.), *Buoyancy Effects on Coastal and Estuarine Dynamics*, pp. 301–317. Amer. Geophys. Union.
- Prather, M. J. (1986). Numerical advection by conservation of second-order moments. *J. Geophys. Res.-Atmos.* 91(D6), 6671–6681.
- Pritchard, D. W. (1994). What is an estuary? Physical viewpoint. In G. H. Lauff (Ed.), *Estuaries* (83 ed.), pp. 3–5. AAAS.
- Rahmstorf, S. (2007). A semi-empirical approach to projecting future sea level rise. *Science* 315, 368–370.
- Reed, D. J. (1990). The impact of sea-level rise on coastal salt marshes. *Progress in Phys. Geo.* 14, 24–40.

- Reed, D. J. (1995). The response of coastal marshes to sea-level rise: survival or submergence. *Earth Surface Processes Landforms* 20, 39–48.
- Rennau, H. and H. Burchard (2009). Quantitative analysis of numerically induced mixing in a coastal model application. *Ocean Dyn.*, 671–687.
- Reshef, M., D. Kosloff, M. Edwards, and C. Hsiung (1988). Three-dimensional elastic modeling by the Fourier method. *Geophys.* 53, 1184–1193.
- Richardson, L. F. (1926). Atmospheric diffusion shown on a distance-neighbour graph. *Proc. R. Soc. Lond A.* 110, 709–737.
- Roberts, P. V., M. N. Goltz, and D. M. Mackay (1986). A natural gradient experiment on solute transport in a sand aquifer: 3. Retardation estimates and mass balances for organic solutes. *Water Resour. Res.* 22, 2047–2058.
- Roe, P. L. (1984). Generalized formulation of TVD Lax-Wendroff schemes. NASA Langley Research Center Technical Report, ICASE Report 84-53. NASA CR-172478.
- Runge, C. (1895). Über die numerische Auflösung von Differentialgleichungen. *Math. Ann.* 46, 167–178.
- Sankaranarayanan, S. and D. F. McCay (2003). Application of a two-dimensional depth-averaged hydrodynamic tidal model. *Ocean Eng.* 30, 1807–1832.
- Schallenberg, M., C. J. Hall, and C. W. Burns (2003). Consequences of climate-induced increases on zooplankton abundance and diversity in coastal lakes. *Marine Eco. Prog. Series* 251, 181–189.
- Schijf, J. B. and J. C. Schonfeld (1953). Theoretical considerations on the motion of salt and fresh water. In *Proc., Minnesota Int. Hydraul. Conf.*, Minneapolis, Minnesota, pp. 321–333. IAHR.
- Schubel, J. R. (1993). Managing freshwater discharge to the San Francisco Bay-Delta Estuary: The scientific basis for an estuarine standard. Technical report, San Francisco Estuary Project, U.S. Environmental Protection Agency, San Francisco, California.



- Scwing, F. B., M. O'Farrell, J. Steger, and K. Baltz (1996). Coastal upwelling indices, west coast of North America 1946-1995. Tech. rep. noaa-tm-nmfs-swfsc-231, 207 pp., Natl. Oceanic. Atmos. Admin., Silver Spring, MD.
- Shchepetkin, A. and J. C. McWilliams (2005). The regional oceanic modeling system (ROMS): A split-explicit, free-surface, topography-following-coordinate oceanic model. *Ocean Modell.* 9, 347–404.
- Sherif, M. M. and V. P. Singh (1999). Effect of climate change on sea water intrusion in coastal aquifers. *Hydrol. Process.* 13, 1277–1287.
- Short, F. T. and H. A. Neckles (1999). The effects of global climate change on seagrasses. *Aqua. Botany* 63, 169–196.
- Signell, R. P. and B. Butman (1992). Modeling tidal exchange and dispersion in Boston Harbor. *J. Geophys. Res.* 97, 15591–15606.
- Signell, R. P. and W. R. Geyer (2007). Numerical simulation of tidal dispersion around a coastal headland. In R. T. Cheng (Ed.), *Residual Currents and Long-Term Transport in Estuaries and Bays. Lecture Notes on Coastal and Estuarine Studies*, New York. Springer-Verlag.
- Simpson, J. H., J. Brown, J. Matthews, and G. Allen (1990). Tidal straining, density currents, and stirring in the control of estuarine stratification. *Estuaries* 13, 125–132.
- Smaoui, H. and B. Radi (2002). Comparative study of different advective schemes: Application to the MECCA model. *Env. Fluid Mech.* 1, 361–381.
- Smith, L. H. and R. T. Cheng (1987). Tidal and tidally averaged circulation characteristics of Suisun Bay, California. *Water Resour. Res.* 23(1), 145–155.
- Smith, P. E. (2006). A semi-implicit, three-dimensional model for estuarine circulation. Technical report, USGS Open-File Report 2006-1004. 176 pp.
- Smith, P. E., J. M. Donovan, and H. F. N. Wong (2005). Applications of 3D hydrodynamic and particle tracking models in the San Francisco Bay-Delta Estuary. In *Proc. World Water and Environmental Resources Congress*, Anchorage, AK. American Society of Civil Engineers. 8 pp.

- Sommer, T., B. Suits, M. Mierzwa, and J. Wilde (1993). Evaluation of residence time and entrainment using a particle tracking model for the Sacramento-San Joaquin Delta. Technical report, California Dept. Water Res., Sacramento, California. Draft paper.
- Stacey, M. T., J. P. Fram, and F. K. Chow (2008). The role of tidally periodic density stratification in the creation of estuarine subtidal circulation. *J. Geophys. Res.* *113*. C08016, doi:10.1029/2007JC004581.
- Stommel, H. and H. G. Farmer (1952). On the nature of estuarine circulation. Tech. Rep. 52-88, Woods Hole Oceano. Inst.
- Sudicky, E. A. (1986). A natural gradient experiment on solute transport in a sand aquifer: Spatial variability of hydraulic conductivity and its role in the dispersion process. *Water Resour. Res.* *22*, 2069–2082.
- Sullivan, G. D. and A. D. Richard (1994). Report on clean water act  $X_2$  water quality standards. Technical report, Contra Costa Water District, Concord, CA. Tech. report.
- Sverdrup, H. U., M. W. Johnson, and R. H. Flemming (1942). *The oceans - their physics, chemistry and general biology*. Englewood Cliffs, N. J.
- Sweby, P. K. (1984). High resolution schemes using flux limiters for hyperbolic conservation laws. *SIAM J. Numer. Analysis* *25*(5), 995–1011.
- Titus, J. G. (1988). Greenhouse effect, sea level rise, and coastal wetlands. Technical report, U.S. Environmental Protection Agency, Washington, D.C. EPA 230-05-86-013.
- Titus, J. G. and C. Richman (2001). Maps of lands vulnerable to sea level rise: Modeled elevation along the US Atlantic and Gulf coasts. *Climate Research* *18*, 205–228.
- Turkel, E. (1986). Accuracy of scheme with nonuniform meshes for compressible fluid flows. *Appl. Numer. Math.* *2*, 529–550.
- VonNeumann, J. and R. D. Richtmyer (1950). A method for the numerical calculation of hydrodynamic shocks. *J. Appl. Phys.* *21*. doi:10.1063/1.1699639.

- Walters, R. A., R. T. Cheng, and T. J. Conomos (1985). Time scales of circulation and mixing processes of San Francisco Bay waters. *Hydrobiol.* 129, 13–36.
- Wang, B., O. B. Fringer, S. N. Gridding, and D. A. Fong (2008). High-resolution simulations of a macrotidal estuary using SUNTANS. *Ocean Modell.* 28, 167–192.
- Wang, B., S. N. Giddings, O. B. Fringer, E. S. Gross, D. A. Fong, and S. G. Monismith (2011a). Modeling and understanding turbulent mixing in a macrotidal salt wedge estuary. *J. Geophys. Res.* 116. C02036,doi:10.1029/2010JC006135.
- Wang, B., G. Zhao, and O. B. Fringer (2011b). Reconstruction of vector fields for semi-lagrangian advection on unstructured staggered grids. *Ocean Modelling*. doi:10.1016/j.ocemod.2011.06.003.
- Warming, R. F. and B. J. Hyett (1974). The modified equation approach to the stability and accuracy analysis of finite-difference methods. *J. Comp. Phys.* 14, 159–179.
- Warner, J. C., W. R. Geyer, and J. A. Lerczak (2005). Numerical modeling of an estuary: A comprehensive skill assessment. *J. Geophys. Res.* 110. C05001, doi:10.1029/2004JC002691.
- Werner, A. D. and C. T. Simmons (2009). Impact of sea-level rise on sea water intrusion in coastal aquifers. *Ground Water* 47, 197–204.
- Williams, P. B. (1987). The impacts of climate change on the salinity of San Francisco Bay. Technical report, U.S. Environmental Protection Agency, Philip Williams and Associates, San Francisco, California. EPA 230-05-89-051.
- Zheng, L. C. and C. H. Liu (2003). A modeling study of the Satilla River estuary, Georgia I: Flooding-drying process and water exchange over the salt marsh-estuary-shelf complex. *Estuaries* 26, 651–669.
- Zimmerman, J. T. F. (1976). Mixing and flushing of tidal embayments in the western Dutch Wadden Sea part 1: Distribution of salinity and calculation of mixing time scales. *Neth. J. Sea Res.* 10, 149–191.

- Zimmerman, J. T. F. (1986). The tidal whirlpool: A review of horizontal dispersion by tidal and residual currents. *Neth. J. Sea Res.* 20, 133–154.